

2
2002

LIBRARY
Michigan State
University

This is to certify that the

dissertation entitled

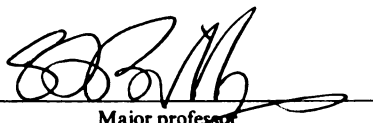
Local Strain in $\text{ZnSe}(1-x)\text{Te}(x)$ Alloys

presented by

PETER F. PETERSON

has been accepted towards fulfillment
of the requirements for

Ph.D degree in Physics


Major professor
S. Billinge

Date 10/22/01

PLACE IN RETURN BOX to remove this checkout from your record.
TO AVOID FINES return on or before date due.
MAY BE RECALLED with earlier due date if requested.

| DATE DUE | DATE DUE | DATE DUE |
|----------|----------|----------|
| | | |
| | | |
| | | |
| | | |
| | | |
| | | |
| | | |
| | | |
| | | |
| | | |

LOCAL STRAIN IN $\text{ZnSe}_{1-x}\text{Te}_x$ ALLOYS

By

PETER F. PETERSON

A DISSERTATION

Submitted to
Michigan State University
in partial fulfillment of the requirements
for the degree of

DOCTOR OF PHILOSOPHY

Physics

2001

ABSTRACT
LOCAL STRAIN IN $\text{ZnSe}_{1-x}\text{Te}_x$ ALLOYS

By
PETER F. PETERSON

Pseudobinary semiconductor alloys are of great interest because the lattice parameter and energy band gap can be varied by changing the composition. The atomic structure of $\text{ZnSe}_{1-x}\text{Te}_x$ is studied using the pair distribution function (PDF) measured with the General Materials Diffractometer (GEM) at ISIS. While the zincblende average atomic structure interpolates linearly between the end-member (ZnSe and ZnTe) values, the local structure stays closer to the end-member structure. Understanding the interplay between these length scales is the focus of this work.

The local structure is found to have two distinct nearest neighbor (nn) bond lengths in the alloys. No strain effects are seen in the nn PDF peak widths using temperature dependent data. In contrast, the far neighbor (fn) bonds show strain in their PDF peak widths. The fn peak widths have two components to them, one from strain and one from thermal motion. The nn and fn PDF peak widths as a function of temperature are adequately described by the Debye and Einstein models respectively.

Quantitative analysis is done using the Kirkwood potential model. Model PDFs are calculated without adjustable parameters using bond bending and stretching force constants from the literature. Agreement with the measured PDFs is quite good showing how well the Kirkwood model describes the structure. The Kirkwood model predicts the structure of other semiconductor alloys, here the structure $\text{In}_x\text{Ga}_{1-x}\text{As}$ is compared to that of $\text{ZnSe}_{1-x}\text{Te}_x$. Qualitatively all of the results of $\text{ZnSe}_{1-x}\text{Te}_x$ and $\text{In}_x\text{Ga}_{1-x}\text{As}$ are the same, therefore the difference in chemical composition appears to have little bearing on the atomic structure of the material.

Copyright by
PETER F. PETERSON
2001

For Sharon and Alex

Acknowledgements

None of this research would have happened without my adviser, Simon Billinge. I greatly appreciate his willingness to let me participate in such a wide variety of projects throughout my time at MSU. I also need to thank my guidance committee members, Phillip Duxbury, Edwin Loh, Scott Pratt, and Stuart Tessmer, for their time and effort.

The entire Billinge group was very helpful, but I would like to make special mention of a few of them. Thomas Proffen for collaborating on the majority of the software projects, Valeri Petkov for teaching me so much about x-ray measurements, Jeroen Thompson for making me responsible for all of the equipment the group owns, and Emil Bozin for joining me on the snipe hunt we call PDF quality. Collaborators outside of the group that have been of special help are Mike Thorpe for his discussions of the Kirkwood model, and Kyoung-Shin Choi for sample fabrication and teaching me how to wield a propane torch.

I also must thank the group of students that helped me stay (moderately) sane throughout the last couple of years in *the basement*. And finally, my family, who have been curious, confused, and supportive throughout my time at MSU.

Table of Contents

| | |
|---|-----------|
| LIST OF TABLES | ix |
| LIST OF FIGURES | x |
| 1 Introduction | 1 |
| 1.1 Introduction | 1 |
| 1.2 Properties of Semiconductors | 3 |
| 1.2.1 Electronic Structure | 4 |
| 1.2.2 Atomic Structure | 5 |
| 1.3 Pair Distribution Function | 7 |
| 1.4 Layout of Dissertation | 8 |
| 2 The Pair Distribution Function Technique | 9 |
| 2.1 Introduction | 9 |
| 2.2 The Pair Distribution Function | 10 |
| 2.3 Data Collection | 14 |
| 2.3.1 Neutrons | 15 |
| 2.3.2 X-rays | 16 |
| 2.4 Data Reduction | 18 |
| 2.5 Peak Position and Width | 18 |
| 2.6 Structural Modelling | 21 |

| | | |
|----------|--|-----------|
| 2.7 | Summary | 21 |
| 3 | Measures of Pair Distribution Function Quality | 22 |
| 3.1 | Introduction | 22 |
| 3.2 | Finite Measurement Range | 25 |
| 3.3 | Quality Measure | 29 |
| 3.3.1 | Definition of Quality Measures | 29 |
| 3.3.2 | Testing the Quality Measures | 36 |
| 3.4 | Data Analysis Protocols | 46 |
| 3.4.1 | Methods of Optimizing PDFs | 49 |
| 3.5 | Summary | 52 |
| 4 | Local Bond Length Mismatch in $\text{ZnSe}_{1-x}\text{Te}_x$ | 53 |
| 4.1 | Introduction | 53 |
| 4.2 | Experimental | 55 |
| 4.2.1 | Synthesis and Characterization | 55 |
| 4.2.2 | Neutron Measurements and Data Processing | 57 |
| 4.2.3 | Method of Modeling | 58 |
| 4.3 | Results and Discussion | 61 |
| 4.3.1 | Model Independent Results | 61 |
| 4.3.2 | Kirkwood Model | 64 |
| 4.3.3 | Comparison with $\text{In}_x\text{Ga}_{1-x}\text{As}$ | 65 |

| | | |
|----------|--|-----------|
| 4.4 | Conclusion | 68 |
| 5 | Temperature Dependence of $\text{ZnSe}_{1-x}\text{Te}_x$ | 69 |
| 5.1 | Introduction | 69 |
| 5.2 | Experimental | 71 |
| 5.2.1 | Data Reduction | 71 |
| 5.2.2 | Method of Extracting Peak Widths | 72 |
| 5.3 | Nearest Neighbor Information | 73 |
| 5.4 | Far Neighbor Information | 76 |
| 5.5 | Conclusions | 79 |
| 6 | Summary and Discussion | 81 |
| 6.1 | Summary | 81 |
| 6.2 | Future Work | 83 |
| | APPENDIX | 85 |
| | LIST OF REFERENCES | 87 |

List of Tables

| | | |
|-----|---|----|
| 3.1 | Values of quality criteria unspoiled data with Q_{max} of 100\AA^{-1} and 40\AA^{-1} . | 40 |
| 3.2 | Values of quality criteria for different amounts of random noise. R_{wp} is calculated between the test data and the ideal PDF. | 40 |
| 3.3 | Values of quality criteria for various scaling. | 41 |
| 3.4 | Values of quality criteria for various systematic errors. R_{wp} is calculated between the test data and the appropriately scaled ideal PDF. The three columns are shown in Figures 3.7 and 3.8 as (a), (b), and (c) respectively. | 42 |
| 3.5 | Results of varying different parameters. The traditional method columns, in order, are done by using physical parameters, varying ρ_{eff} to minimize G_{low} , and reducing σ_{eff} then varying ρ_{eff} to minimize G_{low} . The second half of the table is done by varying α , ρ_{eff} , and σ_{eff} with β to obtain $N_m = 1$ and minimize G_{low} | 51 |
| 4.1 | α and β reported for $\text{ZnSe}_{1-x}\text{Te}_x$ and $\text{In}_x\text{Ga}_{1-x}\text{As}$. [1] | 61 |
| 4.2 | Ionic radii from literature when atoms are in tetrahedral covalent bonds. [2] | 67 |
| 5.1 | Debye temperature found from the nn peak widths with $\sigma_{eff}^2=0.0\text{\AA}^2$. | 74 |
| 5.2 | Parameters for Einstein model fit to the fn peak widths. | 77 |

List of Figures

| | | |
|-----|---|----|
| 1.1 | Abbreviated periodic table of elements with atomic numbers. | 3 |
| 1.2 | Cartoon of a reduced zone energy diagram showing the allowed states for a one dimensional crystal. The bands are shown to the left of the diagram. | 4 |
| 1.3 | The zinc-blende structure shown with conventional unit cell. | 6 |
| 1.4 | Comparison of the Pauling and Vegard limits for a pseudobinary alloy. | 7 |
| 2.1 | General physical setup of for a PDF measurement. The incident radiation scatters off of a powder sample held at the center of the diffractometer. Scattered radiation is detected by either an array of detectors or by a single detector that is rotated through an angle. | 14 |
| 2.2 | 10K Garnet data measured at the General Materials Diffractometer (GEM) at ISIS. From top to bottom the raw data, the fully corrected total scattering structure function, and the resulting PDF. | 19 |
| 3.1 | The termination function along with its components (inset) for $Q_{min}=0.9\text{\AA}^{-1}$ and $Q_{max}=40\text{\AA}^{-1}$ | 26 |
| 3.2 | The error function (dark line), sine and cosine components (grey lines), and the components (inset) for $Q_{min}=0.9\text{\AA}^{-1}$ and $Q_{max}=40\text{\AA}^{-1}$. The amplitude of the oscillations at $r=0.9\text{\AA}$ is 3\AA^{-2} | 27 |
| 3.3 | Synthetic 10K Germanium PDF (a) as calculated by PDFFIT and resulting $S(Q)$ (b) calculated by Fourier transform. The synthetic data was calculated using parameters to mimic a GLAD measurement. | 37 |
| 3.4 | Value of S_{int} and G_{int} as a function of Q_{max} and R_{max} respectively. The dotted lines are the theoretical values. | 38 |
| 3.5 | Reduced total scattering structure function (left), form of noise dS added to $S(Q)$ (inset), and associated PDFs (right). From top to bottom the synthetic data are pure, constant noise added, Q -dependent noise added. | 39 |

| | | |
|------|---|----|
| 3.6 | $S(Q)$ (left), and associated PDFs (right). From top to bottom the scale, α , is 0.5, 1.0 and 2.0. Both $S(Q)$ and $G(r)$ are offset for clarity. | 42 |
| 3.7 | $Q[S(Q) - 1]$ for three types of errors, (a) long wavelength sine oscillation, (b) step function, and (c) sine oscillation with Q -dependent random noise. Below each structure function is the difference between the data with and without errors. The insets are the same data plotted from 0\AA^{-1} to 100\AA^{-1} . | 43 |
| 3.8 | $G(r)$ for three types of errors, (a) long wavelength sine oscillation, (b) step function, and (c) sine oscillation with Q -dependent random noise. Below each PDF is the difference between the data with and without errors. | 44 |
| 3.9 | Representative reduced total scattering structure factor for Germanium at 10K measured using GLAD at IPNS. | 47 |
| 3.10 | Representative PDF (circles), PDFFIT model (line) and difference curve with 2σ error bars as dotted lines (below) for Germanium at 10K measured using GLAD at IPNS. The sine systematic error with Q -dependent noise test data with Q_{max} of 25\AA^{-1} (inset) is also shown for comparison. | 48 |
| 4.1 | The zinc-blende structure shown with conventional unit cell. | 54 |
| 4.2 | $\langle 331 \rangle$ and weak $\langle 420 \rangle$ peaks of $\text{ZnSe}_{1-x}\text{Te}_x$ measured at 300K using Cu rotating anode. | 56 |
| 4.3 | $Q[S(Q) - 1]$ for $\text{ZnSe}_{1-x}\text{Te}_x$ measured at 10K. | 58 |
| 4.4 | $G(r) = 4\pi r(\rho(r) - \rho_0)$ for $\text{ZnSe}_{1-x}\text{Te}_x$ measured at 10K. | 59 |
| 4.5 | nn positions from the PDF (\bullet), EXAFS data [3] (\circ), and Kirkwood model z -plot (solid line) [1] as a function of composition, x , for $\text{ZnSe}_{1-x}\text{Te}_x$. The angled dashed line is the average nn distance. The horizontal dashed lines are at the end-member distances for comparison. Note that not all EXAFS points had reported error bars so they were all set to the same value. | 62 |

| | | |
|-----|--|----|
| 4.6 | Square of the PDF peak widths for near (\circ) and far (\bullet) neighbors as a function of composition, x . The extracted values are plotted with parabolas (lines) to guide the eye. The upper dotted line is at 0.0056\AA^2 and the lower is at 0.0024\AA^2 | 63 |
| 4.7 | Comparison of the Kirkwood model (lines) and data (\circ) PDFs for (from top to bottom) ZnTe, $\text{ZnSe}_{3/6}\text{Te}_{3/6}$, $\text{ZnSe}_{4/6}\text{Te}_{2/6}$, and ZnSe. | 65 |
| 4.8 | Comparison of the Kirkwood model (lines) and data (points) nn distances for $\text{ZnSe}_{1-x}\text{Te}_x$ where x is 0 (\times), $\frac{1}{6}$ (\circ), $\frac{2}{6}$ (\diamond), $\frac{3}{6}$ (\oplus), $\frac{4}{6}$ (\star), $\frac{5}{6}$ (Δ), and 1 (+). | 66 |
| 4.9 | Comparison of the theoretically calculated $\text{ZnSe}_{1-x}\text{Te}_x$ (solid line) and $\text{In}_x\text{Ga}_{1-x}\text{As}$ (dashed line) z-plots. | 67 |
| 5.1 | Cartoon of motion in solids. Rigid body motion (a), correlated atomic motion (b), and uncorrelated atomic motion (c) are shown. | 70 |
| 5.2 | Data measured as a function of temperature and composition. The data was measured for 60 minutes (\bigcirc), 45 minutes (\square), and 30 minutes (Δ). | 72 |
| 5.3 | nn peak widths for Zn-Se (a) and Zn-Te (b). The widths are extracted from ZnSe (\square), $\text{ZnSe}_{0.5}\text{Te}_{0.5}$ (\bigcirc), and ZnTe (Δ). The solid lines are the Debye model fit to the data. | 74 |
| 5.4 | fn peak widths for Zn-Zn (a), Zn-Alloy (b), and Alloy-Alloy (c) plotted with fits of the Einstein model. The widths are extracted from ZnSe (\square), $\text{ZnSe}_{0.5}\text{Te}_{0.5}$ (\bigcirc), and ZnTe (Δ). | 77 |

Chapter 1: Introduction

1.1 Introduction

Semiconductors are very useful and are seen throughout modern society in a large variety of devices. The vast majority of semiconductor devices are integrated circuits built using Silicon as a base. The best example of this is computers. Earliest computers used amplifier tubes to make the logical circuit, occupied large rooms, and only served to replace trajectory tables used for firing artillery. In contrast, modern computers contain millions of transistors with feature sizes as small as $0.13\mu m$. As technology continues to shrink features to produce smaller, faster, devices there is a growing need for understanding the underlying physics of semiconductors.

In the semiconductor industry the majority of devices are made using doped thin films of Silicon, Germanium, or Gallium-Arsenide. Because of its widespread use, Silicon is the cheapest material to manufacture devices with and has the largest variety of techniques surrounding its fabrication and processing. The search for new devices has led to other semiconductor materials finding greater use in industry because of their particular electronic or structural properties. Pseudobinary semiconductor alloys, especially, are finding greater use because of their ability to select the lattice parameter, a , and the energy band gap, E_g . [4, 5, 6, 7]

Similar semiconductors, for example ZnSe and ZnTe, can be alloyed together to produce pseudobinary alloys. By alloying semiconductors, the structure of the two end-member systems, ZnSe and ZnTe, are merged to form a new material, $ZnSe_{1-x}Te_x$. ZnSe and ZnTe, both have zinc-blende structure (space-group symmetry $F\bar{4}3m$), [8] the alloy is also zinc-blende and has a well defined lattice parameter that interpolates linearly between the end member values consistent with

Vegard's law. [9] Vegard's law states that alloying materials' macroscopic parameters, such as the lattice parameter, vary linearly between the end-member values. Because the inter-atomic potential of ZnSe and ZnTe have different optimal nearest neighbor (nn) distance, strain is introduced by alloying.

The study of alloys is complicated by the fact that considerable local atomic strains are present due to the ordering effect of alloying. This means that local bond-lengths can differ from those inferred from the average (crystallographic) structure by as much as 0.1 Å. [10, 11] This clearly has a significant effect on calculations of electronic and transport properties. [5] To fully characterize the structure of these alloys it is necessary to augment crystallography with local structural measurements.

The traditional method of structure determination, Rietveld analysis of Bragg peaks from powder diffraction, cannot resolve the local structure. [12] Rietveld refinements are a probe of global structure and will fail to see the strain which appears in the diffuse scattering produced by the local structure varying from the crystalline behavior. In the past the extended x-ray absorption fine structure (XAFS) technique has been extensively used. [3, 10, 13] XAFS uses the absorption edge of an atomic species to find chemical specific local information of a powder. XAFS lead to the result that pseudobinary alloys have two distinct bond lengths, but it is unable to reproduce the crystallographic structure. A limitation of the XAFS method for studying the local structure of alloys is that it only gives information about the first and second neighbor bond-lengths. Also, the measurement is atomic species specific and information about bond-length distributions is less accurate than bond-length determination. More recently the atomic pair distribution function (PDF) analysis of powder diffraction data has also been applied to get additional local structural information from $\text{In}_x\text{Ga}_{1-x}\text{As}$ alloys along with the average structure. [11, 14, 15]

| | | | | | | |
|------------------|------------------|------------------|------------------|------------------|------------------|------------------|
| II | III | IV | V | VI | VII | ² He |
| | ⁵ B | ⁶ C | ⁷ N | ⁸ O | ⁹ F | ¹⁰ Ne |
| | ¹³ Al | ¹⁴ Si | ¹⁵ P | ¹⁶ S | ¹⁷ Cl | ¹⁸ Ar |
| ³⁰ Zn | ³¹ Ga | ³² Ge | ³³ As | ³⁴ Se | ³⁵ Br | ³⁶ Kr |
| ⁴⁸ Cd | ⁴⁹ In | ⁵⁰ Sn | ⁵¹ Sb | ⁵² Te | ⁵³ I | ⁵⁴ Xe |
| ⁸⁰ Hg | ⁸¹ Tl | ⁸² Pb | ⁸³ Bi | ⁸⁵ Po | ⁸⁶ At | ⁸⁷ Rn |

Figure 1.1: Abbreviated periodic table of elements with atomic numbers.

This dissertation will discuss the atomic structure of pseudobinary semiconductor alloys, using the example of $\text{ZnSe}_{1-x}\text{Te}_x$ at 10K, with the PDF technique. $\text{ZnSe}_{1-x}\text{Te}_x$ is further explored by looking at the temperature dependence of the structure.

1.2 Properties of Semiconductors

Silicon, Germanium, and Gallium-Arsenide are the most thoroughly understood semiconductors due to their widespread use. Everything from the mobility as a function of temperature to the energy diagrams are in introductory texts on the subject. [16, 17, 18, 19, 20] All semiconductors can be placed into one of three general groups: elemental semiconductors, compounds, and alloys. Silicon and Germanium fit into the elemental group while InAs, GaAs, ZnSe, and ZnTe are all semiconductor compounds. Looking at the abbreviated periodic table in Figure 1.1 one immediately sees that compounds are composed of elements in columns equally spaced from the IV column. Semiconductor alloys are obtained by combining semiconductors from the other two groups. Examples of alloys are $\text{Si}_x\text{Ge}_{1-x}$,

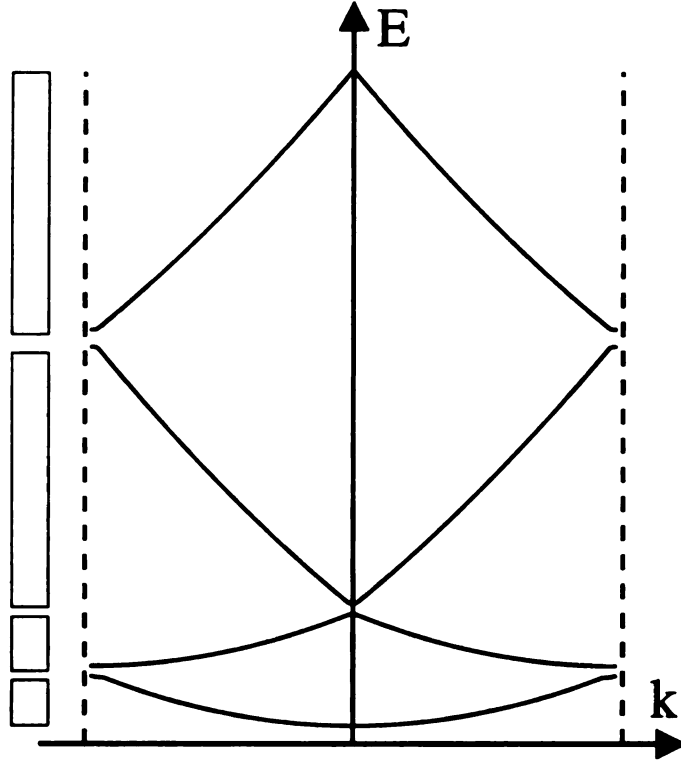


Figure 1.2: Cartoon of a reduced zone energy diagram showing the allowed states for a one dimensional crystal. The bands are shown to the left of the diagram.

$\text{In}_x\text{Ga}_{1-x}\text{As}$, and $\text{ZnSe}_{1-x}\text{Te}_x$ which are IV-IV, III-V, II-VI semiconductor alloys respectively. The x subscript in the alloy formulas denote the percentage of each end-member material, for example, $x = 1$ in $\text{ZnSe}_{1-x}\text{Te}_x$ is ZnTe . However, not all elements or compounds can be alloyed together over the entire range of composition or at all. [21]

1.2.1 Electronic Structure

Features of the electronic structure, while not explored in this dissertation, are presented here for motivational purposes. Charge carriers in a solid material are described by their momentum and energy. For semiconductors, the electron or hole is travelling through a periodic potential determined by the atomic structure of the semiconductor. Globally, semiconductors are periodic in their structure therefore

the potential is periodic and, in turn, the particle's wavefunction must also be periodic. This observation is succinctly stated by the Bloch theorem, [22]

$$\psi(\vec{r} + \vec{R}) = e^{i\vec{k} \cdot \vec{R}} \psi(\vec{r}), \quad (1.1)$$

where $\psi(\vec{r})$ is the wavefunction, \vec{r} is the position of the particle, \vec{R} is a direct lattice vector, and \vec{k} is a reciprocal lattice vector. The result of the Bloch theorem is that the particle must lie within particular energy bands. A qualitative picture of the energy bands and how they arise, for a one-dimensional system, is seen in Figure 1.2. [16, 22] The general features of the energy diagram in Figure 1.2 are also present in the diagrams of real three-dimensional solids. One should notice that there are bands of allowed energies separated by gaps. The size of these gaps dictates many of the electronic properties of a given semiconductor. At room temperature the energy gap between valance and conduction bands is 1.12eV for Silicon, 0.66eV for Germanium, and 1.42eV for Gallium-Arsenide. [17] The size of the band gap is of similar to visible light (0.28eV for red to 0.49eV for violet). As seen in the Bloch theorem a very important parameter is the crystal structure of the material which appears as \vec{R} in Equation 1.1.

1.2.2 Atomic Structure

This dissertation concentrates on the structure of semiconductor alloys, however, much is already known about the structure of bulk semiconductors. Most semiconductors crystalize in diamond, zinc-blende or wurtzite structures. The zinc-blende structure is shown in Figure 1.3 which can be viewed as two interpenetrating face centered cubic (fcc) sub-lattices offset by $a \times (\frac{1}{4}, \frac{1}{4}, \frac{1}{4})$, where a is the lattice parameter and $(\frac{1}{4}, \frac{1}{4}, \frac{1}{4})$ is the in the direction of the body diagonal. The diamond structure is a special case of zinc-blende where both sub-lattices are

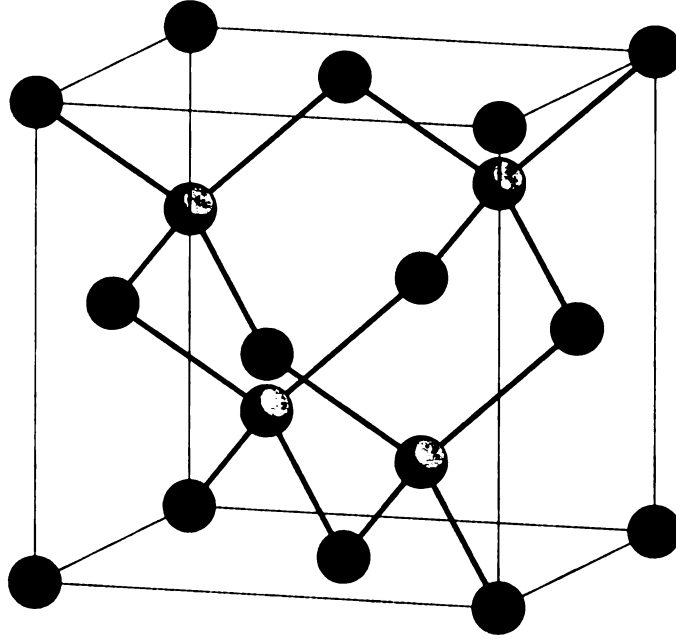


Figure 1.3: The zinc-blende structure shown with conventional unit cell.

occupied by the same atomic species. The zinc-blende and diamond structures have four nn and the conventional unit cell contains eight atoms.

For semiconductor alloys, as suggested above, the local structure differs from that of a simple crystal. Alloying a material adds strain into the material by changing the nn bond lengths. Figure 1.4 demonstrates the two limits of the nn bond length. It is possible that the nn distance, L , remains at the value dictated by the crystallographic structure. For zinc-blende crystals this is $L = a\sqrt{3}/4$. This is known as the Vegard limit and can be seen as the solid line in the figure. In contrast, the atoms can stay at their end-member values for the entire alloy range, this is known as the Pauling limit and is represented as the dashed lines in the figure.

Somehow the intermediate length-scale structure must link the local order to the global order. The case of the Vegard limit is trivial since the local and average structure are the same. However, the Pauling limit produces a large amount of strain that must be accommodated by the average structure. Strain is seen in the

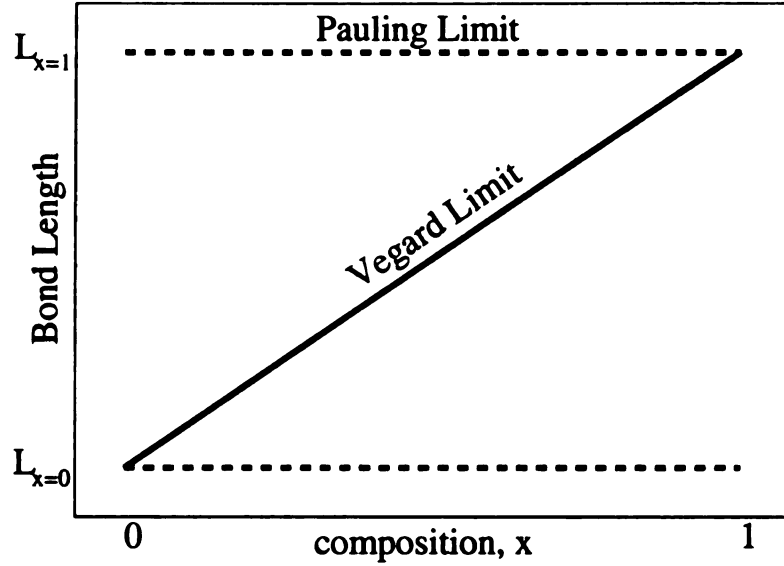


Figure 1.4: Comparison of the Pauling and Vegard limits for a pseudobinary alloy.

average structure as broadening of the bond length distributions. To reduce the amount of broadening due to thermal motion the alloys should be studied at low temperature. This has a disadvantage for understanding the materials as they are normally used at or above room temperature. Therefore, it is also necessary to study the development of the strain in the alloy as a function of temperature.

1.3 Pair Distribution Function

In this study, the PDF analysis of neutron powder diffraction data is used. The PDF is the instantaneous atomic number density-density correlation function which describes the atomic arrangement of the materials. It is the Sine Fourier transform of the experimentally observed total scattering structure function, $S(Q)$, obtained from a powder diffraction experiment. Since the total scattering structure function includes both the Bragg and diffuse scattering, the PDF contains both *local* and *average* atomic structure yielding accurate information on short and intermediate length-scales. Previous high resolution PDF studies on $\text{In}_x\text{Ga}_{1-x}\text{As}$ were carried out

using high energy x-ray diffraction. [11, 15, 23] This yielded data over a wide Q -range (Q is the magnitude of the scattering vector) which resulted in the very high real-space resolution required to separate the nearest neighbor peaks from In-As and Ga-As. The high Q -range coverage and Q -space resolution of the General Materials (GEM) Diffractometer at the ISIS neutron source allowed similarly high real space resolution PDFs of $\text{ZnSe}_{1-x}\text{Te}_x$ using neutrons and to resolve the Zn-Se and Zn-Te bonds that differ in length by only 0.14 Å. Furthermore, the data collection time was an hour or less compared to the twelve hours for the x-ray data with similar quality.

1.4 Layout of Dissertation

In Chapter 2 we discuss the basics of the PDF technique. The reader will be introduced to the PDF formalism, terms related to the PDF and general methods for extracting structural information from the PDF. Chapter 3 further explores the PDF technique by determining the quality of the PDF using different criteria. The criteria introduced are used in later chapters to automate portions of data reduction process. The structure of $\text{ZnSe}_{1-x}\text{Te}_x$ at 10K is presented in Chapter 4 and compared to predictions of the Kirkwood model. Similarities between $\text{ZnSe}_{1-x}\text{Te}_x$ and $\text{In}_x\text{Ga}_{1-x}\text{As}$ are also discussed. Chapter 5 discusses how the low-temperature structure of $\text{ZnSe}_{1-x}\text{Te}_x$ relates to the room temperature structure using the Einstein and Debye models. Finally, summary and discussion are in Chapter 6.

Chapter 2: The Pair Distribution Function Technique

2.1 Introduction

Diffraction has long been used to study the microscopic structure of materials. [24, 25, 26] Initially, crystalline materials were studied using low intensity x-ray sources, looking at the position and relative intensity of the Bragg diffraction the symmetry and lattice vectors can be determined. However, this left the majority of interesting materials unavailable since they are not crystalline in nature. All deviations from the average structure appear in diffuse scattering which, in general, is of low intensity and time-consuming to measure. With powder diffraction all angular information is removed from the scattered intensity but the problem of low intensity is greatly reduced. The development of Extended X-ray Absorption Fine Structure (EXAFS) allows for the measure of the nearest neighbor (nn) and, with less accuracy, next nearest neighbor (nnn) distribution. [3] EXAFS uses x-rays tuned to an energy for a particular chemical species. This opened up the study of glasses, liquids and other amorphous materials, but limits measurements to short range order and to materials with accessible energies. The Pair Distribution Function (PDF) technique is another method developed to study amorphous materials, glasses, and liquids. [27] Like EXAFS, PDF has the disadvantage of averaging over angles, however, PDF not only measures the short range order but also the intermediate range and, potentially, long range order. Due to the greater amount of information in the PDF measurement, a structural model can be built which, in order to agree with data, must correctly reconstruct the angular information as well as distances. The PDF technique is now used to study, in addition to amorphous

materials, the local deviations in the structure of crystalline materials where the inconsistency with traditional Bragg structure refinements was not fully explained. In this chapter we will present the formalism of the PDF technique, methods of data acquisition, and two methods of structure determination.

2.2 The Pair Distribution Function

The PDF technique relies on the scattering of either neutrons or x-rays from a powder sample. Incident radiation of a known state are scattered off an unknown potential then the final state is measured. Information about the scattering potential is gained since the both the initial and final states of the scattered radiation are, within experimental uncertainty, known. In general, the final state of radiation will have a different wave vector, \vec{k}' , and energy.

The formalism of the PDF will begin with the elastic scattering amplitude, $f_{\vec{k}}(\theta, \phi)$, where \vec{k} denotes the incident radiation wave vector. The scattering amplitude is

$$f_{\vec{k}}(\theta, \phi) = \int e^{-i\vec{k}\cdot\vec{x}} U(\vec{x}) e^{i\vec{k}'\cdot\vec{x}} d^3x, \quad (2.1)$$

where $U(\vec{x})$ is the scattering potential and \vec{k}' is wave vector of the scattered radiation. When there is more than one atom acting as a scattering center then interference occurs between radiation scattered from different points. In the limit of an infinite periodic array of atoms we achieve the Laue condition where a Bragg peak appears whenever the change in wave vector, $\vec{Q} = \vec{k}' - \vec{k}$, is equal to a reciprocal lattice vector. Recall that, for elastic scattering, Q is the familiar

$$Q = |\vec{Q}| = \frac{4\pi}{\lambda} \sin \theta, \quad (2.2)$$

where 2θ is the diffraction angle. When the atoms are not perfectly periodic then

diffuse scattering appears in the diffraction pattern which cannot be seen using analysis of the Bragg diffraction. The scattering potential can be written as a sum of potentials from the different atoms

$$U(\vec{x}) = \sum_p U_p(\vec{R}_p) \quad (2.3)$$

where $\vec{R}_p = \vec{x} - \vec{x}_p$ and \vec{x}_p is the position of an atom. Then the scattering amplitude can be written as

$$\begin{aligned} f_{\vec{k}}(\theta, \phi) &= \int \sum_p e^{i(\vec{k}' - \vec{k}) \cdot (\vec{x}_p + \vec{R}_p)} U(\vec{R}_p) d^3 R_p \\ &= \sum_p e^{i\vec{Q} \cdot \vec{x}_p} \int e^{i\vec{Q} \cdot \vec{R}_p} U(\vec{R}_p) d^3 R_p. \end{aligned} \quad (2.4)$$

The integral portion of this equation is the Fourier transform of the atomic potential, therefore

$$f_{\vec{k}}(\theta, \phi) = \sum_p e^{i\vec{Q} \cdot \vec{x}_p} U_p(\vec{Q}). \quad (2.5)$$

For neutron scattering, the atomic potential is essentially a delta function, independent of direction, so $U_p(\vec{Q}) = b_p$ where b_p is called the scattering length since the scattering cross section is $\sigma_p = 4\pi b_p^2$. The square of the scattering amplitude is the measured scattering intensity,

$$\begin{aligned} I(\vec{Q}) &= f_{\vec{k}}^*(\theta, \phi) f_{\vec{k}}(\theta, \phi) \\ &= \sum_p b_p^* e^{-i\vec{Q} \cdot \vec{x}_p} \sum_q b_q e^{i\vec{Q} \cdot \vec{x}_q} \\ &= \sum_{pq} b_p b_q e^{i\vec{Q} \cdot (\vec{x}_q - \vec{x}_p)}. \end{aligned} \quad (2.6)$$

Since the scattering intensity is measured rather than the scattering amplitude, all phase information is lost. Because the sample is isotropic, there is no angular

information in the scattering intensity. It is convenient to introduce $\vec{r}_{pq} = \vec{x}_q - \vec{x}_p$. Because the scattering is isotropic it is only the relative distance between the atoms, $r_{pq} = |\vec{r}_{pq}|$, that matters. In the case when only elastic scattering is considered, Q is dependent only on the directions of the incident and scattered radiation. Averaging the scattering intensity over all angles

$$\begin{aligned} I(Q) &= \sum_{pq} b_p b_q \frac{1}{4\pi} \int_0^{2\pi} \int_0^\pi e^{iQr_{pq} \cos \xi} r_{pq}^2 \sin \xi d\xi d\chi \\ &= \sum_{pq} b_p b_q \frac{\sin(Qr_{pq})}{Qr_{pq}}. \end{aligned} \quad (2.7)$$

This is known as the Debye scattering equation. [28] Here it is useful to introduce the density function, $\rho_p(r_{pq})$, such that the number of atoms in the volume dV_q a distance r_{pq} away from atom p is given by $\rho_p(r_{pq})dV_q$. Then, for a monatomic material

$$I(Q) = \sum_p b^2 + \sum_p b^2 \int \rho_p(r_{pq}) \frac{\sin(Qr_{pq})}{Qr_{pq}} dV_q. \quad (2.8)$$

Letting $r_{pq} = r$ and $\rho(r)$ be the average of $\rho_p(r_{pq})$ over all pairs of atoms

$$I(Q) = \sum_p b^2 + \sum_p b^2 \int_0^\infty 4\pi r^2 \rho(r) \frac{\sin(Qr)}{Qr} dr. \quad (2.9)$$

We then introduce the total number of atoms to be n . Adding and subtracting the average number density, ρ_0 ,

$$I(Q) = nb^2 + nb^2 \int_0^\infty 4\pi r^2 [\rho(r) - \rho_0] \frac{\sin(Qr)}{Qr} dr + nb^2 \int_0^\infty 4\pi r^2 \rho_0 \frac{\sin(Qr)}{Qr} dr. \quad (2.10)$$

The third term is the self scattering term. The self-scattering all occurs in the forward direction and cannot be separated from the unscattered direct beam. It is therefore not measured and cannot be included as an experimental observable. The tails of the self-scattering become visible as "small angle scattering" when the

sample contains microscopic inhomogeneities. In most crystalline and amorphous samples this is not present but, in principle, small angle scattering should be removed from measured data before determining $S(Q)$. In practice, even when it is present it has a negligible effect on the PDF since it is confined to the very low- Q region. On the other hand, studying small angle scattering directly is a very powerful method for studying nanometer to micron scale inhomogeneities in samples. Following Eq. 2.10 we define the total scattering structure function, $S(Q)$ as

$$S(Q) = \frac{I(Q)}{nb^2} - 1 = \int_0^\infty 4\pi r^2 [\rho(r) - \rho_0] \frac{\sin(Qr)}{Qr} dr. \quad (2.11)$$

When more than one atomic species is present $S(Q)$ can be written as

$$S(Q) = \frac{I(Q)}{n\langle b \rangle^2} - \frac{\langle b^2 \rangle - \langle b \rangle^2}{\langle b \rangle^2}. \quad (2.12)$$

Then the scattering equation can be rearranged to resemble a Fourier transform

$$F(Q) = Q[S(Q) - 1] = \int_0^\infty 4\pi r [\rho(r) - \rho_0] \sin(Qr) dr. \quad (2.13)$$

$F(Q)$ is called the reduced total scattering structure function and the kernel of the integral is the pair distribution function, $G(r)$. The inverse Fourier transform of Equation 2.13 is

$$G(r) = 4\pi r [\rho(r) - \rho_0] = \frac{2}{\pi} \int_0^\infty Q[S(Q) - 1] \sin(Qr) dQ, \quad (2.14)$$

which is how the PDF is obtained from scattering data. For x-rays, while the precise derivation is different, Equations 2.12, 2.13, and 2.14 are still valid.

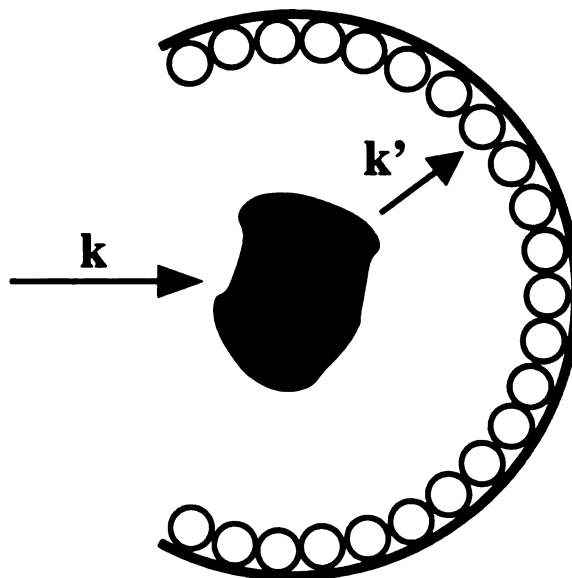


Figure 2.1: General physical setup of for a PDF measurement. The incident radiation scatters off of a powder sample held at the center of the diffractometer. Scattered radiation is detected by either an array of detectors or by a single detector that is rotated through an angle.

2.3 Data Collection

The basics of a PDF can be seen in Figure 2.1. The incident radiation, either neutrons or x-rays, is well characterized and scatters off of the sample in the center of the diffractometer. The scattered radiation is recorded as a function of scattering angle, 2θ , and time (in the case of neutrons) or energy (for synchrotron x-rays). The recorded intensity is used to create the intensity of the single scattered radiation as a function of momentum transfer, Q . The sample environment, background, and incident radiation are also measured to aid in data processing as described in the next section. Below is a description of the differences between neutron and x-ray measurements.

2.3.1 Neutrons

All of the neutron diffraction measurements used for the production of this dissertation were performed at the General Materials Diffractometer (GEM) at ISIS. Pulses of neutrons are produced by accelerating bundles of 800MeV protons at a tantalum target with a current of $20\mu\text{A}$ to produce 2×10^{16} neutrons per second at a frequency of 50Hz. The spallation produces a pulse of neutrons which enter a moderator of liquid methane kept at 100K which produces a spectrum of neutrons with wavelengths from 0.25\AA to 8\AA . The neutrons travel from the moderator down a 17m evacuated flight path before scattering off of the powder sample. The sample is ten to fifteen grams of powder sealed in an extended vanadium container under a Helium environment. The Helium is present to displace any moisture and allow for good thermal contact between the sample and the cold stage. Moisture is a concern because Hydrogen is a strong neutron scatterer and produces a large signal that obscures the measurement. The temperature was controlled using a cryo-furnace that can control the temperature from 8K to 450K to within a few tenths of a degree.

Once scattered by the sample, the neutrons travel to an array of detectors 1m to 2m away. The location of the incoming neutrons as well as the time of arrival are recorded to determine the momentum transfer, Q . The wavelength of the neutron is determined from the total time of flight of the neutron using the deBroglie relation, $\lambda = h/p$; the speed of the neutron is given by $v = L/t$, where L is the flight length and t is the time of flight. The 4140 detectors are time focused to 2θ angles of 17.9° , 63.6° , and 91.4° . Time focusing is a process where detectors at $2\theta + \delta\theta$ are offset by a time to give times to the neutrons as if they were measured at 2θ . The mapping does not significantly reduce the resolution of the measured scattering intensity. Because of the detector locations and the finite diffraction spectrum the Q -range and resolution of each bank is different. The effect of Q resolution is to reduce the

absolute height of the high- r peaks of the PDF.

2.3.2 X-rays

X-ray measurements have no analog of the time of flight technique. Because of this the incident beam has a well known energy by either using a characteristic fixed tube (Cu, Mo, or Ag), rotating anode (Cu), or synchrotron using a monochromator. Since traditional fixed tube and rotating anode sources have a fixed energy (Cu 8.04keV, Mo 17.44keV, and Ag 22.11keV) which have a relatively small maximum Q (Cu 8.15\AA^{-1} , Mo 17.68\AA^{-1} , and Ag 22.41\AA^{-1}) the description here will be limited to synchrotron sources. While the effect of a limited Q_{max} is discussed in the next chapter, it is sufficient to say here that a greater Q_{max} allows for smaller differences in bond lengths to be resolved. While no data presented in this dissertation was measured using x-rays we will discuss the method for the 1-ID hutch at SRI-CAT at the Advanced Photon Source (APS).

X-rays are produced by a electron storage ring 1.1km in diameter. To increase the number of initial photons from the storage ring the protons pass through a undulator insertion device (ID). A undulator has varying magnetic poles that rapidly oscillate the electrons to produces x-rays between 2.5keV and 100keV in energy. By varying the gap between the poles of the undulator the number of photons entering the initial beam optics can be varied. The white beam enters the initial optics, kept in vacuum, by first passing through slits to cut down the physical size of the incident beam and reduce the heat load on the double crystal, fixed exit, Laue type monochromator used to disperse the beam before entering paddle slits that separate the initial optics from the enclosure. Inside the enclosure the monochromatic beam is kept within a Helium filled flight tube to reduce air scattering before it scatters off the sample at the center of a Huber four circle diffractometer. The sample is in flat plate geometry held between two thin

(~ 0.001 inch) pieces of kapton tape inside a displacer that is attached to the ϕ -circle. The displacer is used to control the temperature between 8K and 300K. The thickness of the sample is varied to obtain an absorption, μt , of 0.5 to 1.

The scattered x-rays pass through detector slits and a secondary Helium filled flight path before entering a single energy-dispersive Germanium detector attached to the 2θ -circle. The spectrum measured is sent through two sets of electronics in parallel, a multi-channel analyzer (MCA) and a set of single channel analyzers (SCAs) with different energy windows. The spectrum is sent through the electronics to allow for the reduction of the spectrum to only the unmodified Thompson scattering. This is often referred to by x-ray diffractionists as "elastic scattering" though it contains inelastic scattering from low energy processes such as phonons. In general there is "elastic" scattering, Compton scattering (often called "inelastic"), and x-ray fluorescence from the sample. SCAs are used to specify specific energy window that are recorded during the experiment and are normally set to capture the elastic signal, Compton signal, elastic and Compton signal, and a fluorescence signal. While using SCAs has the advantage of speed and relatively small data files, improperly set energy window can ruin an experiment. A MCA records the entire energy spectrum at each point so the elastic scattering can be extracted during the processing stage. [29]

The geometry used for synchrotron experiments has the ϕ - and 2θ -circles in the scattering plane with the ϕ -circle acting as θ keeping the ratio $2\theta/\phi = 2$. The beam has a small physical size (normally $\sim 2\text{mm} \times \sim 1\text{mm}$) and the sample is fairly thin ($\sim 0.5\text{mm}$ thick) so there is, in general, a problem with having too little sample in the beam for proper powder averaging. To counteract the lack of sample in the beam, the χ -circle is rocked $\pm 2^\circ$ for better powder averaging. The sample is measured several times to improve statistics with concentration on the high- Q region.

2.4 Data Reduction

The intensity listed in Equation 2.12 is the scattering intensity from single scattering events from the sample only. The measured intensity differs from the intensity of Equation 2.12 in that it contains (for example) multiple scattering events, absorption effects, scattering from the sample environment, varying detector efficiencies, and changing amount of incident radiation. The methods for correcting the data for these effects, while incomplete, include characterization measurements of the background and theoretical models for the multiple scattering and absorption and can be seen in Figure 2.2. The reader is referred to the software used to process the data: PDFgetN [30] for neutron data and PDFgetX [31] for both in house and synchrotron x-ray data for more information.

2.5 Peak Position and Width

Simple structural modeling will reveal information from the bond length distribution of a particular bond. The PDF is a correlation function, therefore, a change in bond length distribution can easily be seen as a change in the PDF peak width or height. While peak fitting does not yield information about the overall symmetry of a material it can be used to give information about the material on a particular length scale as a function of a macroscopic parameter such as temperature or magnetic field. To study changes in the PDF peaks, it is necessary to introduce a few new functions which are related to the PDF. First is the radial distribution function (RDF)

$$T(r) = 4\pi r^2 \rho(r) = \sum_{i \leq j} \frac{b_i b_j}{\langle b \rangle^2} \delta(r - r_{ij}). \quad (2.15)$$

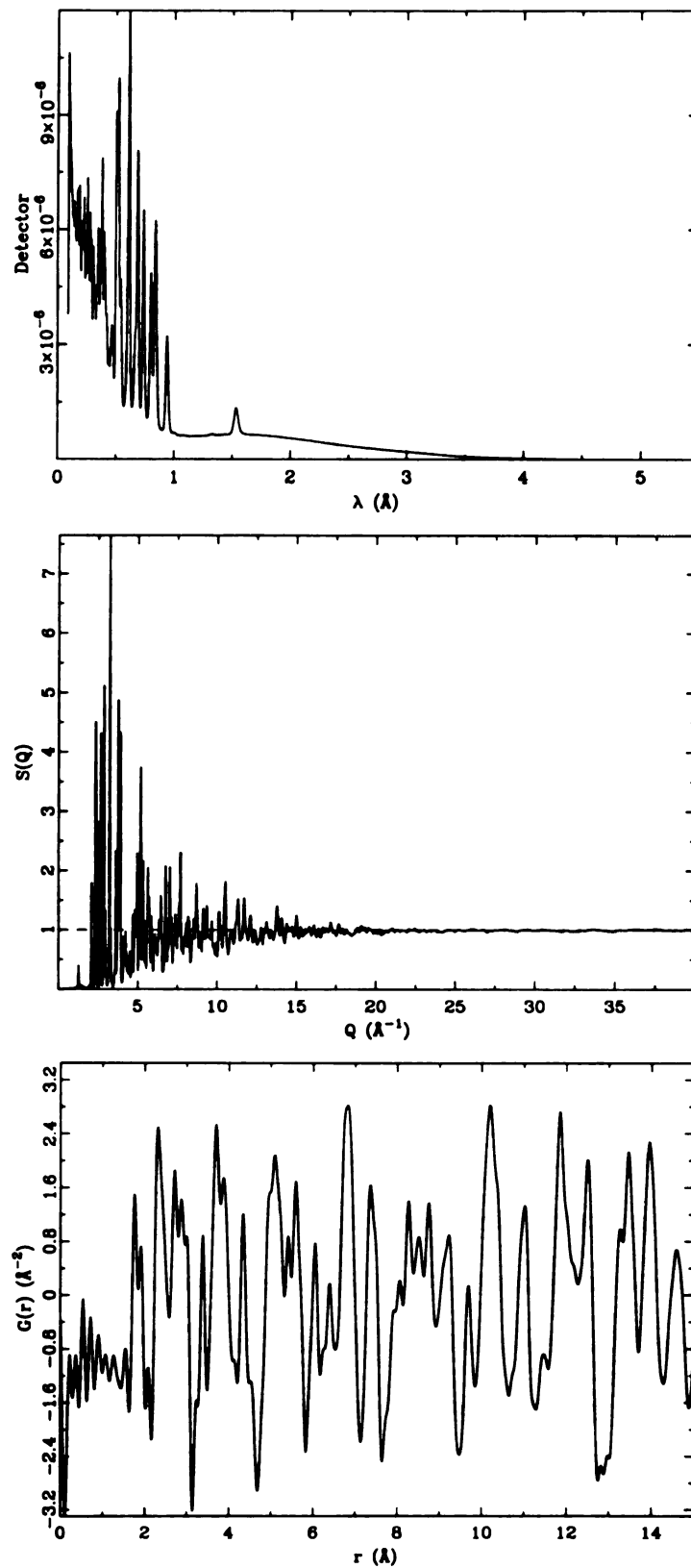


Figure 2.2: 10K Garnet data measured at the General Materials Diffractometer (GEM) at ISIS. From top to bottom the raw data, the fully corrected total scattering structure function, and the resulting PDF.

As above, r_{ij} is the distance between the i th and j th atoms and the RDF, like the PDF, is a correlation function. The main difference between the function is the baseline. Another useful function is the integral of the RDF called the correlation number

$$n(r) = \int_0^r T(x)dx = \int_0^r 4\pi x^2 \rho(x)dx. \quad (2.16)$$

$n(r)$ is the number of neighbors, weighted by the scattering length, within the distance r .

When finding the peak width, or height, one should always find this information from the RDF because it can be fit with a simple Gaussian. The delta functions can be approximated by a Gaussian and the RDF becomes

$$T(r) \propto \sum_{i \leq j} \frac{b_i b_j}{\langle b \rangle^2 \sqrt{2\pi\sigma_{ij}^2}} \exp\left(-\frac{(r - r_{ij})^2}{2\sigma_{ij}^2}\right). \quad (2.17)$$

It is then obvious how peak width and height are related. Since the area under the peak is constant the height is inversely proportional to the width. A simple example of this is that when a sample is heated the atoms move more. In the absence of a phase transition the width of a RDF peak will simply broaden, however, the number of atoms at that distance are fixed, so the height of the peak must reduce in order to keep the integrated number of atoms, $n(r)$, fixed. This can be used to study a particular bond length in a material. While the overall structure of the material is fixed, a particular bond may change in width to accommodate strain introduced by things such as polarons, [32] tilt disorder, [33] or bond-length mismatch. [11] Here we fit the nn peak distribution to determine the position and width of the nn bond. This quantifies the local structure which is compared with the crystal structure as described below.

2.6 Structural Modelling

In contrast to peak fitting, full structural refinements using PDFFIT allow for the study of the crystal structure. [34] PDFFIT allows for constrained fitting of PDF data without use of symmetry parameters that are not explicitly included in the refinement. For materials studied in this dissertation all of the lattice parameters are set to be equal ($a = b = c$), the angle between the lattice vectors are ($\alpha = \beta = \gamma$) 90° , and the atoms are all on the symmetry sites (Zn on $[0,0,0]$ and Se,Te on $[\frac{1}{4}, \frac{1}{4}, \frac{1}{4}]$). In order to learn anything, however, one must refine some parameters.

Normally the known crystal structure is refined by varying atom positions and anisotropic thermal factors. Here we vary the scale factor, N_m , the instrument resolution, σ_Q , the dynamic correlation factor, δ , the lattice parameter, a , and the chemical species specific isotropic thermal factor, U . This is a minimalist approach to structure refinement but the main point of interest here is the effects of strain. While strain does effect the bond lengths, the effect can be eliminated by not including the nn peak in the refinement. By determining the isotropic thermal factors we obtain the far neighbor (fn) peak width, σ_p^2 , which quantify the effect of the local strain on the crystal structure.

2.7 Summary

In this chapter we laid out many of the terms and techniques associated with the PDF. We saw that the PDF allows for determination of the structure on different length scales. This is done by high resolution measurements which are fit using either individual peak fitting or structural refinements.

Chapter 3: Measures of Pair Distribution Function Quality

3.1 Introduction

In this chapter we discuss how to assess and improve the quality of a pair distribution function (PDF) given a structure function, $S(Q)$, that has been obtained from experimental data. As we discussed previously, the PDF has been widely used to study glasses and amorphous materials, [24, 25] but more recently it has been used to study the structure of crystalline materials. [35, 36] An important aspect of every structural technique is to obtain the best results possible from a given measurement. This can be achieved either by improving the measurement method or by processing the data better; we will be discussing the latter.

The most important equations of the PDF are reproduced here for convenience. The PDF, $G(r)$, is obtained from the experimentally determined total scattering structure function, $S(Q)$, by a Sine Fourier transform

$$\begin{aligned} G(r) &= \frac{2}{\pi} \int_0^\infty Q[S(Q) - 1] \sin(Qr) dQ \\ &= 4\pi r(\rho(r) - \rho_0), \end{aligned} \tag{3.1}$$

where

$$\rho(r) = \frac{1}{4\pi r^2} \sum_{ij} \frac{b_i b_j}{\langle b \rangle^2} \delta(r - r_{ij}), \tag{3.2}$$

is the microscopic pair density, and ρ_0 is the average number density of the sample. The sum is taken over all atoms in the sample and $r_{ij} = |\vec{r}_i - \vec{r}_j|$ is the distance separating the i th and j th atoms. It gives the probability of finding two atoms separated by a distance r , weighted by the scattering lengths, and averaged over all

pairs of atoms in the sample.

In a real experiment a number of corrections to the intensity data must be carried out in order to obtain the structure function, $S(Q)$, normalized to the total scattering cross-section of the sample. In principle, the data corrections are well known and well understood [24, 25, 37, 38, 39, 40, 41] and the data analysis can be carried out with no adjustable parameters. In practice, a number of approximations must be made in calculating these corrections and certain parameters are not known with high accuracy. Using these approximations results in a corrected, normalized, $S(Q)$ which contains distortions. The distortions are usually dealt with in somewhat arbitrary ways as described below. Fortunately, the structural information in the PDF is rather robust with respect to these distortions. Inadequacies in the corrections tend to result in very long wavelength distortions to $S(Q)$ giving rise to features in $G(r)$ at nonphysical low values of atomic separation, r . The distortions do not affect the data except insofar as ripples from these features propagate into the high- r region. Frequently an expert eye is needed to minimize distortions to $S(Q)$ so the physics can be studied. Nonetheless, it is clearly of interest to find more quantitative criteria for assessing the quality of a PDF and to minimize these distortions and obtain the most accurate PDFs possible. As instruments such as General Materials Diffractometer (GEM) at ISIS come online increased data acquisition rates necessitate an automated data processing method. A number of indirect methods have been proposed for the Fourier transform such as the case of Reverse Monte Carlo [42] and Bayesian methods [43] and these address this issue. Here we prefer to consider how to obtain the best $S(Q)$ possible for direct Fourier transform.

The most obvious problem to detect is when $S(Q)$ does not asymptote to one as $Q \rightarrow \infty$. In practice, the data are adjusted to obtain the right asymptote. However, it is not *a priori* clear whether the correction should be to add a constant,

multiply by a factor, or apply some other correction. This is because it is often not clear which data correction, or corrections, are primarily to blame for the problem. Some data corrections are additive, such as background, empty can, multiple scattering and incoherent scattering subtractions, and others are multiplicative, such as normalization for flux and number of atoms in the illuminated sample volume and absorption corrections.

A number of different approaches are often taken at this point. The most common is to make the sample density a parameter and vary it until the asymptotic behavior of $S(Q)$ is correct ($S(Q) \rightarrow 1$ as $Q \rightarrow \infty$). This practice is somewhat arbitrary since in many cases this will not be the limiting factor in the accuracy of the corrections as the sample density is easy to determine with reasonable accuracy. It should be noted that varying the sample density applies a predominantly multiplicative correction (it strongly affects the sample-normalization and the absorption correction) to the data with a small additive part (from the multiple scattering correction and an incorrect background subtraction due to the incorrect absorption correction). Another commonly varied parameter is the *effective beam width*. The beam-size is known from the collimation of the instrument, but the beam may not be homogeneous. [38, 39] Therefore, the effective beam width will be different from the physical beam-size due to varying intensity across the beam profile. This beam-size is a predominantly multiplicative correction due to flux normalization, however, it will also have an additive component due to differently evaluated multiple scattering corrections. Less commonly used parameters that can be varied are sample height or effective beam-height.

Since the choice of parameters to vary is mostly arbitrary, it is interesting to see whether taking the completely arbitrary approach of simply multiplying the data by a constant and/or adding a constant results in PDFs of equally good quality. Here we compare a number of different approaches for data normalization.

Since our primary interest is the study of crystalline materials we have chosen to use a neutron data-set from pure Germanium. We systematically apply both a multiplicative and an additive correction to the processed $S(Q)$, obtain the PDF by direct Fourier transform, and analyze the results using a number of PDF quality criteria defined below. The PDF is very sensitive to the asymptotic behavior of $S(Q)$ so we confine our interest to data where $\lim_{Q \rightarrow \infty} \langle S(Q) \rangle = 1.00(2)$. Since Germanium is crystalline with a well defined structure, by modeling we can easily determine when the data are properly normalized. It is then possible to compare different approaches that satisfy these criteria; for example, varying a multiplicative constant, α , and an additive constant, β , varying the sample density ρ_{eff} and β , and so on. The resulting PDFs are then compared using the quality factors. Finally, we suggest a protocol for automatically obtaining the best PDF given an initial experimentally derived $S(Q)$.

3.2 Finite Measurement Range

As discussed above, the corrections to the data are incomplete. This is not only due to the simplifications made to the data corrections but also because characterization runs do not yield the complete picture of the physical set-up. Scattering events when an incident neutron scatters off of the sample, then the sample environment, before entering a detector cannot be fully subtracted using characterization runs where the sample is not present. These inadequacies in the measurement and processing result in a measured total scattering structure function, $S'(Q)$, that varies from the true $S(Q)$. In general, the measured $S'(Q)$ can be written in terms of the true $S(Q)$ as,

$$S'(Q) = \alpha(Q)S(Q) + \beta(Q), \quad (3.3)$$

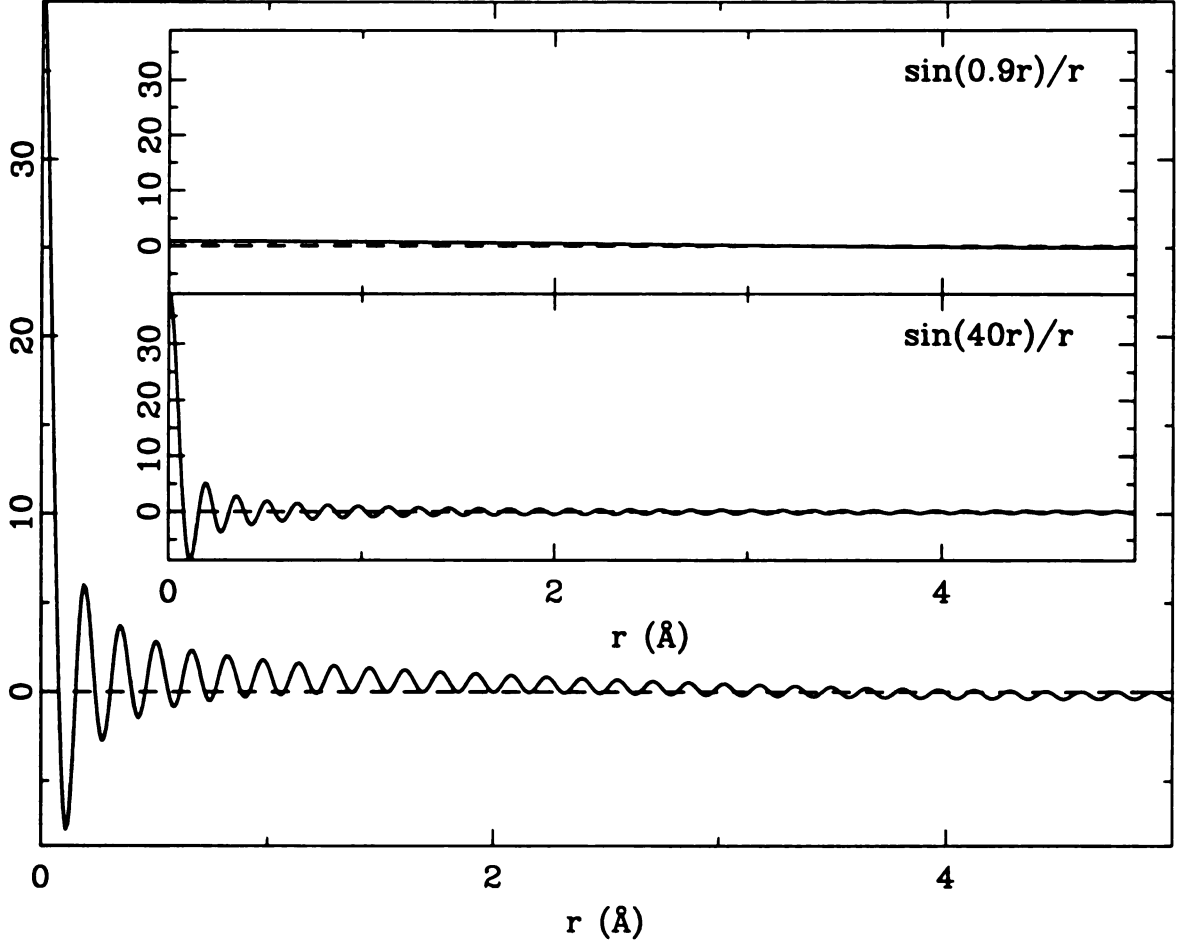


Figure 3.1: The termination function along with its components (inset) for $Q_{min}=0.9\text{\AA}^{-1}$ and $Q_{max}=40\text{\AA}^{-1}$.

where $\alpha(Q)$ and $\beta(Q)$ are dimensionless functions. The simplest approximation is to take $\alpha(Q)$ and $\beta(Q)$ as being independent of momentum transfer, Q , in which case Equation 3.3 becomes,

$$S'(Q) = \alpha S(Q) + \beta. \quad (3.4)$$

The PDF associated with $S'(Q)$ can be written in terms of $S(Q)$ as,

$$\begin{aligned} G'(r) &= \frac{2}{\pi} \int_0^\infty Q[S'(Q) - 1] \sin(Qr) dQ \\ &= \frac{2}{\pi} \int_0^\infty Q[\alpha S(Q) + \beta - 1] \sin(Qr) dQ. \end{aligned} \quad (3.5)$$

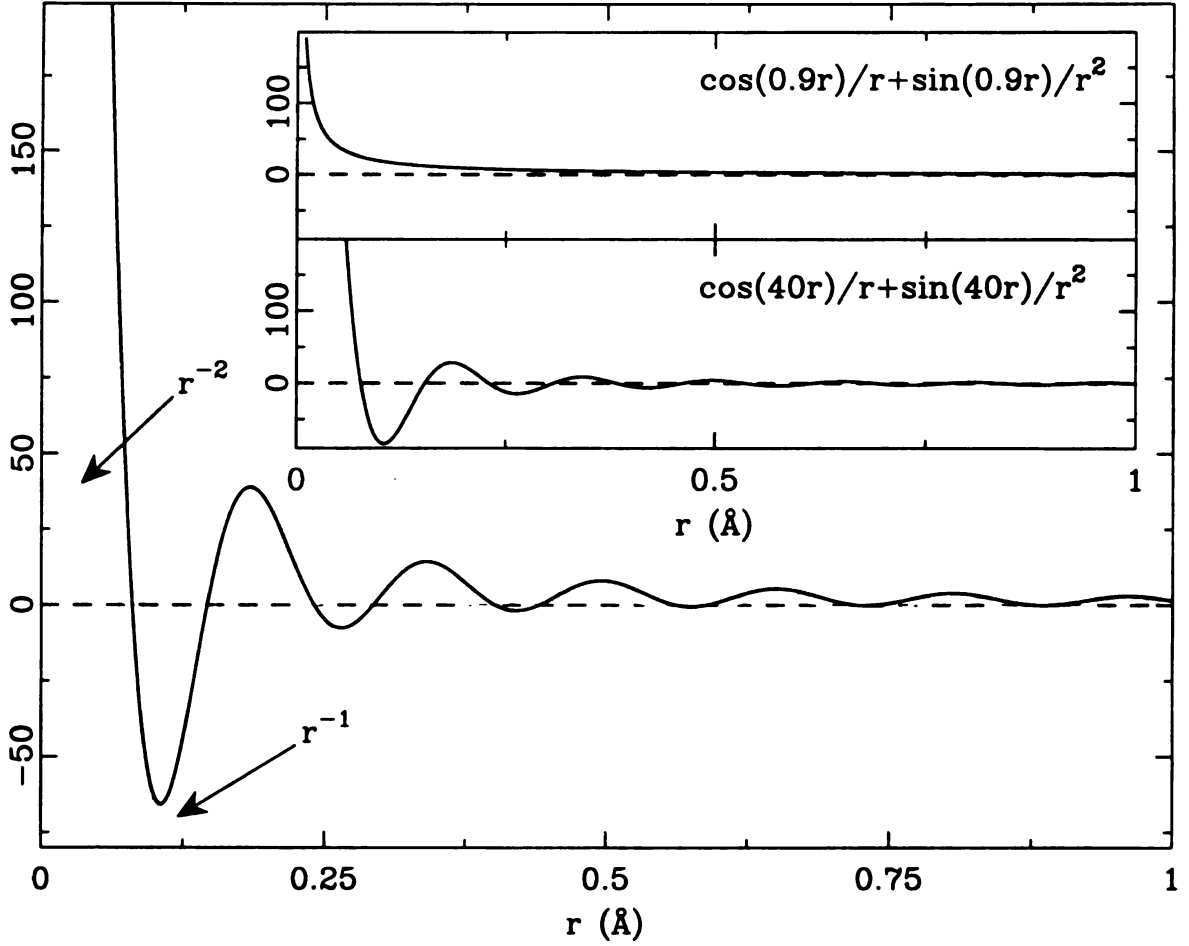


Figure 3.2: The error function (dark line), sine and cosine components (grey lines), and the components (inset) for $Q_{min}=0.9 \text{ Å}^{-1}$ and $Q_{max}=40 \text{ Å}^{-1}$. The amplitude of the oscillations at $r=0.9 \text{ Å}$ is 3 Å^{-2} .

In addition to α and β , the other experimental effect is the finite measurement range. The PDF then becomes,

$$\begin{aligned}
 G'(r) &= \frac{2}{\pi} \int_{Q_{min}}^{Q_{max}} Q[\alpha S(Q) + \beta - 1] \sin(Qr) dQ \\
 &= \frac{2}{\pi} \int_{Q_{min}}^{Q_{max}} Q[\alpha S(Q) - \alpha + \alpha + \beta - 1] \sin(Qr) dQ \\
 &= \alpha \frac{2}{\pi} \int_{Q_{min}}^{Q_{max}} Q[S(Q) - 1] \sin(Qr) dQ \\
 &\quad + (\alpha + \beta - 1) \frac{2}{\pi} \int_{Q_{min}}^{Q_{max}} Q \sin(Qr) dQ
 \end{aligned}$$

$$= \alpha G_c(r) + (\alpha + \beta - 1)\gamma(r), \quad (3.6)$$

where $G_c(r)$ is the real $G(r)$ convoluted with a termination function and $\gamma(r)$ is defined in Equation 3.6. $\gamma(r)$ is the result of an improper high- Q asymptote of the $S(Q)$.

$G_c(r)$, the PDF convoluted with a termination function, can be written as

$$\begin{aligned} G_c(r) &= \frac{2}{\pi} \int_{Q_{\min}}^{Q_{\max}} Q[S(Q) - 1] \sin(Qr) dQ \\ &= F\{Q[S(Q) - 1]\} * F\{\Theta(Q - Q_{\min}) - \Theta(Q - Q_{\max})\}. \end{aligned} \quad (3.7)$$

The step function,

$$\Theta(Q - Q_a) = \begin{cases} 0 & \text{if } |Q| > |Q_a| \\ 1 & \text{if } |Q| \leq |Q_a| \end{cases}, \quad (3.8)$$

has the Fourier transform

$$\begin{aligned} F\{\Theta(Q - Q_a)\} &= \frac{1}{\pi} \int_0^\infty \Theta(Q - Q_a) \cos(Qr) dQ \\ &= \frac{\sin(Q_a r)}{\pi r} = \frac{Q_a}{\pi} j_0(Q_a r), \end{aligned} \quad (3.9)$$

where j_0 denotes the zeroth order spherical Bessel function shown for completeness.

Then the convoluted PDF can be written as

$$\begin{aligned} G_c(r) &= G(r) * \left[\frac{\sin(Q_{\min} r) - \sin(Q_{\max} r)}{\pi r} \right] \\ &= \frac{2}{\pi} G(r) * \left[\frac{Q_{\min}}{\pi} j_0(Q_{\min} r) - \frac{Q_{\max}}{\pi} j_0(Q_{\max} r) \right]. \end{aligned} \quad (3.10)$$

As seen in Figure 3.1, the high frequency oscillation from a finite Q_{\max} is the dominant effect. For this reason the modeling program PDFFIT convolutes with the

high- Q termination function but does not take into account Q_{min} .

The second term in Equation 3.6 vanishes if $\lim_{Q \rightarrow \infty} S'(Q) = 1$, i.e., $\alpha + \beta = 1$.

If $\alpha + \beta \neq 1$ the form of $\gamma(r)$ becomes important:

$$\begin{aligned}
\gamma(r) &= \frac{2}{\pi} \int_{Q_{min}}^{Q_{max}} Q \sin(Qr) dQ \\
&= F\{Q\Theta(Q - Q_{min})\} - F\{Q\Theta(Q - Q_{max})\} \\
&= \frac{2}{\pi} \left[\frac{Q_{min} \cos(Q_{min}r) - Q_{max} \cos(Q_{max}r)}{r} - \frac{\sin(Q_{min}r) - \sin(Q_{max}r)}{r^2} \right] \\
&= \frac{2}{\pi} [Q_{max}^2 j_1(Q_{max}r) - Q_{min}^2 j_1(Q_{min}r)]. \tag{3.11}
\end{aligned}$$

The function $j_1(Qr)$ in the definition of $\gamma(r)$ is the first order spherical Bessel function. The behavior of $\gamma(r)$ can be seen in Figure 3.2. The two terms of $\gamma(r)$ have r^{-1} and r^{-2} dependence. By selecting Q_{min} and Q_{max} carefully, the r^{-1} dependence can be minimized so only the short range r^{-2} dependence remains [44]. This becomes important when $\alpha(Q)$ and $\beta(Q)$ are not constant in Q in which case $\gamma(r)$ cannot be completely eliminated. In fact, we will show that in this case better quality PDFs can sometimes be obtained when when $\lim_{Q \rightarrow Q_{max}} S(Q) = 1$ is *not* satisfied.

The Q -independence of $\alpha(Q)$ and $\beta(Q)$ approximation made earlier can be removed by convoluting $G_c(r)$ and $\gamma(r)$ with $\alpha(Q)$ and $\beta(Q)$ as they appear in Equation 3.7. Then the relationship would be,

$$G'(r) = F\{\alpha(Q)\} * G_c(r) + F\{\alpha(Q) + \beta(Q) - 1\} * \gamma(r). \tag{3.12}$$

3.3 Quality Measure

3.3.1 Definition of Quality Measures

Quantifying the difference between the measured and real PDF is of great

interest when the PDF is unknown. $G(r)$ has certain known properties that can be used to assess its quality. Here we list several criteria used for determining an optimal PDF that is closest to the real structural PDF.

In the case where the crystallographic structure of the sample is being studied there are well established methods of determining the quality of data. Programs such as PDFFIT [34] and GSAS [45, 46] allow a structural model to be refined and then find how well the model and data agree. Usually this is used to determine how correct a model is, however, if the structure is already well known then these programs can be used to test the quality of measured data. In PDFFIT two criteria that tell us about data quality are weighted profile agreement factor, R_{wp} , and the scale factor, N_m . R_{wp} is defined as, [34]

$$R_{wp} = \frac{\sum_i w(r_i) [G_{obs}(r_i) - G_{calc}(r_i)]^2}{\sum_i w(r_i) [G_{obs}(r_i)]^2} \quad (3.13)$$

where $G_{obs}(r)$ and $G_{calc}(r)$ are the measured and model PDFs respectively and $w(r)$ is the weighting factor. N_m is the factor by which the *model* must be multiplied to give good agreement with the data. We therefore define the factor $N_d = N = 1/N_m$ as the factor which the *data* must be multiplied to result in a properly scaled $G(r)$ ($N_m = 1$). These two criteria, and others resulting from such fitting, require significant knowledge of the material *a priori*. In general they will not be used to determine data quality but instead model quality. For this reason they are not discussed further. The remaining criteria presented will require knowledge of the chemical composition and average number density, ρ_0 , only.

Using only information about the general behavior of $S(Q)$ and the PDF there are three criteria that $S(Q)$ should conform to. The first can be found starting with

Equation 3.1

$$\begin{aligned} 4\pi r(\rho(r) - \rho_0) &= \frac{2r}{\pi} \int_0^\infty Q^2[S(Q) - 1] \frac{\sin(Qr)}{Qr} dQ \\ 2\pi^2(\rho(r) - \rho_0) &= \int_0^\infty Q^2[S(Q) - 1] \frac{\sin(Qr)}{Qr} dQ. \end{aligned} \quad (3.14)$$

If we then consider the case when $r \rightarrow 0$, then

$$2\pi^2(\rho(0) - \rho_0) = \int_0^\infty Q^2[S(Q) - 1] dQ. \quad (3.15)$$

In the derivation of this equation the self-scattering is neglected [24] and $\rho(0) = 0$. Again, this is because no atoms can be found separated by distances less than the nn separation. Thus, we find

$$S_{int} = \int_0^\infty Q^2[S(Q) - 1] dQ = -2\pi^2\rho_0. \quad (3.16)$$

This criterion was used to find normalization constants in earlier studies [47, 48, 49, 50]. This integral can be most accurately evaluated if the coherent intensity in $S(Q)$ at Q_{max} is small. Bragg peaks disappear at this point in crystalline materials.

Next we consider that the high- Q portion of $S(Q)$ should approach one. This observation can be seen starting from the definition of $S(Q)$,

$$S(Q) = \frac{I(Q)}{\langle b \rangle^2} - \frac{\langle b^2 \rangle - \langle b \rangle^2}{\langle b \rangle^2} + \eta, \quad (3.17)$$

where η comes from the compressibility of the sample and is effectively negligible. [24] The second term in the sum is called the normalized Laue term, L . In the high- Q limit the scattered intensity, $I(Q)$ is completely incoherent and becomes simply the total scattering cross-section of the sample, $\langle b^2 \rangle$. Equation 3.17

then becomes

$$\lim_{Q \rightarrow \infty} S(Q) = \frac{\langle b^2 \rangle}{\langle b \rangle^2} - \frac{\langle b^2 \rangle - \langle b \rangle^2}{\langle b \rangle^2} = 1. \quad (3.18)$$

From a practical point of view we would like a way to determine the asymptotic behavior of $S(Q)$ numerically in a semiautomated fashion. We do this by finding the mean value of $S(Q)$ once it has achieved its high- Q asymptote. Here we call this parameter S_{avg} . The range of Q over which the average is calculated should extend down from the maximum Q -value that will be Fourier transformed, Q_{max} . Ideally it should extend over a range of data where most of the scattering is incoherent due to Debye-Waller effects. In general there may be some coherent scattering (since in general Q_{max} is chosen where the coherent signal to noise ratio becomes unfavorable); however, $\langle S \rangle$ should still have a value of one if determined over a sufficiently wide range of Q . In this paper the average is taken over $24 \text{ \AA}^{-1} < Q < Q_{max} = 40 \text{ \AA}^{-1}$ for the synthetic data in Section 3.3.2 and $15 \text{ \AA}^{-1} < Q < Q_{max} = 25 \text{ \AA}^{-1}$ for the measured data presented in Section 3.4.1 This represents a range, $0.6 Q_{max} < Q < Q_{max}$, that was determined empirically to be reasonable.

The low- Q asymptotic behavior of $S(Q)$ is also known and can be used To verify the quality of an experimentally determined $S(Q)$ function. In the limit of low- Q one can see that

$$\lim_{Q \rightarrow 0} S(Q) = \frac{0}{\langle b \rangle^2} - L = -L. \quad (3.19)$$

Then the dispersion, S_{disp} , of $S(Q)$ between its low- Q and high- Q asymptotes is

$$\begin{aligned} S_{disp} &= \lim_{Q \rightarrow \infty} S(Q) - \lim_{Q \rightarrow 0} S(Q) \\ &= 1 + \frac{\langle b^2 \rangle - \langle b \rangle^2}{\langle b \rangle^2}. \end{aligned} \quad (3.20)$$

As with the high- Q asymptote, the low- Q asymptote of an experimentally determined $S(Q)$ is found by determining the mean value of $S(Q)$ over a

Predetermined range at low- Q . While the principle behind S_{avg} and S_{disp} are sound, a better method of calculating their values needs to be determined. The method of determining S_{disp} can be improved through the use of Bayesian statistics [51], though this is beyond the scope of the present work.

Certain correctness criteria, independent of structure, also are known for $G(r)$ and can be used to assess quality. The real-space analog of Equation 3.16 can be found in the following way. If we multiply $G(r)$ by r and integrate from 0 to ∞ , and using Equation 3.1, we get

$$\int_0^\infty rG(r)dr = 4\pi \int_0^\infty r^2\rho(r)dr - N, \quad (3.21)$$

where $N = \int_0^\infty 4\pi r^2\rho_0 dr$ is the total number of atoms in the sample. $r^2\rho(r)$ looks like a microscopic density and its integral over all space might also be expected to yield N . However, it is a pair correlation function. The atom of the pair at the origin is not included in the integral (this corresponds to the neglect of the self-scattering in the derivation of the PDF) and $4\pi \int_0^\infty r^2\rho(r)dr$ ingetrates to $N - 1$. This leads to

$$G_{int} = \int_0^\infty rG(r)dr = -1. \quad (3.22)$$

For most crystalline materials, while there is a finite crystal size, the distance for the correlations to approach the average value occur at very high- r ($\gg 100\text{\AA}$).

We know that $G(r)$ should have the proper scale. If the number of nearest neighbors is known in a particular situation, this can be used to determine the proper scale for $G(r)$ using

$$\begin{aligned} \int_{r_a}^{r_b} 4\pi r^2\rho(r)dr &= \sum_{ij} \frac{b_i b_j}{\langle b \rangle^2} \int_{r_a}^{r_b} \delta(r - r_{ij})dr \\ &= \sum_{ij} \frac{b_i b_j}{\langle b \rangle^2} [n(r_b) - n(r_a)]. \end{aligned} \quad (3.23)$$

This is the coordination number, $n(r)$, between r_a and r_b weighted by the scattering lengths of the atoms. For monatomic materials, Equation 3.23 reduces to

$$\int_{r_a}^{r_b} 4\pi r^2 \rho(r) dr = n(r_b) - n(r_a). \quad (3.24)$$

This kind of scaling is often possible in crystals and network Glasses where the nearest-neighbor coordination number is known with confidence from the chemistry. [41] However, for many studies the coordination number is exactly what is being determined.

In the region where r is less than the nearest-neighbor distance, r_{low} , there are no structural correlations and it is readily seen from Equation 3.1 that

$$G(r) = -4\pi r \rho_0. \quad (3.25)$$

If the scale factor, N , is not unity we get $NG(r) = -4N\pi r \rho_0$. As we discussed previously, it is in this very low- r region of $G(r)$ where features appear that can be directly attributed to systematic errors from experimental uncertainties. Thus, measuring the mean-square fluctuations of the measured $G(r)$ from $-4N\pi r \rho_0$ and summing them in this region below the nearest neighbor peak should be a sensitive measure of how well the corrections are working. One problem is that, in general, N is not known precisely *a priori*. However, by fitting a line through the low- r part of the PDF, $-4N\pi r \rho_0$ (and therefore N) can be estimated. In practice, with crystal samples, it is convenient to use the program PDFFIT to do this, in which case R_{wp} is evaluated in the range $0 < r < r_{low}$ where r_{low} is the highest r point included in the sum. Obviously the nn peak has a finite width and the summation should be terminated below the leading edge of this peak. We thus get a new quality criterion

G'_{low} defined as

$$G'_{low} = \frac{\int_0^{r_{low}} [G(r) + 4\pi r \rho_{fit}]^2 dr}{\int_0^{r_{low}} [4\pi r \rho_{fit}]^2 dr}, \quad (3.26)$$

where ρ_{fit} is the best-fit slope of the low- r PDF and ideally yields $N\rho_0$. As we show later, it is preferable to add an r -weighting to the residuals function since noise ripples that propagate further into the PDF are more harmful than larger features close to $r = 0$ that die out quickly. We therefore define a more general criterion,

G^n_{low} ,

$$G^n_{low} = \frac{\int_0^{r_{low}} r^n [G(r) + 4\pi r \rho_{fit}]^2 dr}{\int_0^{r_{low}} [4\pi r \rho_{fit}]^2 dr}. \quad (3.27)$$

The r^n factor in the numerator allows for different possible r -weighting of the difference. Three different weightings were tried to see what produced the smallest ripples in the low- r region. Our tests indicate that r^2 weighting yields the best result. Therefore, for brevity, we define G_{low} to be

$$G_{low} = \frac{\int_0^{r_{low}} r^2 [G(r) + 4\pi \rho_{fit} r]^2 dr}{\int_0^{r_{low}} (4\pi \rho_{fit} r)^2 dr}. \quad (3.28)$$

The r^2 weighting was also necessary to get an accurate estimation of ρ_{fit} and was therefore used all three cases. Since ρ_{fit} should be $N\rho_0$, this can be used to estimate N if the number density of the material is known. For crystalline materials ρ_0 is known in general being the number of atoms in the unit cell divided by the unit cell volume. This method of obtaining N has the advantage that a model for the structure is not required, although it will be a less direct and sensitive measure of N than using a full structural model.

In the next section the criteria (S_{int} , S_{avg} , S_{disp} , G_{int} , and G_{low}) will be further explored using synthetic data.

3.3.2 Testing the Quality Measures

To further understand the quality measures presented in the previous section they will be tested against synthetic PDFs of varying quality. All of the test PDFs were *generated* from the same ideal initial PDF. The initial PDF was created by calculating $G(r)$ from a model of germanium at 10K using PDFFIT. Instrumental parameters in PDFFIT [34] were chosen appropriate for the Glass, Liquid and Amorphous Materials Diffractometer (GLAD) at the Intense Pulsed Neutron Source (IPNS) (specifically, $\sigma_Q = 0.0657$). This PDF was Fourier transformed to produce an ideal $S(Q)$ using,

$$Q[S(Q) - 1] = \int_{0\text{\AA}}^{130\text{\AA}} G(r) \sin(Qr) dr. \quad (3.29)$$

At $r=130\text{\AA}$ the PDF has already reached its asymptotic value of zero as seen in Figure 3.3(a). The $S(Q)$ produced by this method can be Fourier transformed back from 0\AA^{-1} to 100\AA^{-1} to reproduce the initial PDF.

The utility of the quality factors (and the synthetic data) can be seen by looking at the synthetic data for different values of Q_{max} to represent ideal and measured data. The different quality factors calculated for Q_{max} of 100\AA^{-1} and 40\AA^{-1} ($R_{max}=100\text{\AA}$) are shown in Table 3.1. In the table the reader will quickly notice that the quality factors in Equations 3.16 and 3.22 vary significantly from their theoretical values, especially as Q_{max} is reduced to 40\AA^{-1} , even in the current case where there are no distortions to the data. In Figure 3.4 the values of S_{int} and G_{int} are plotted as a function of Q_{max} and r_{max} respectively. Notice that as Q_{max} and r_{max} go to large values S_{int} and G_{int} do not achieve their theoretical values of $-2\pi^2\rho_0$ and -1. At present we do not understand why this is the case as synthetically generated $S(Q)$ and $G(r)$ should behave ideally. The most probable reason is some kind of numerical error due to the discrete nature of the synthetic

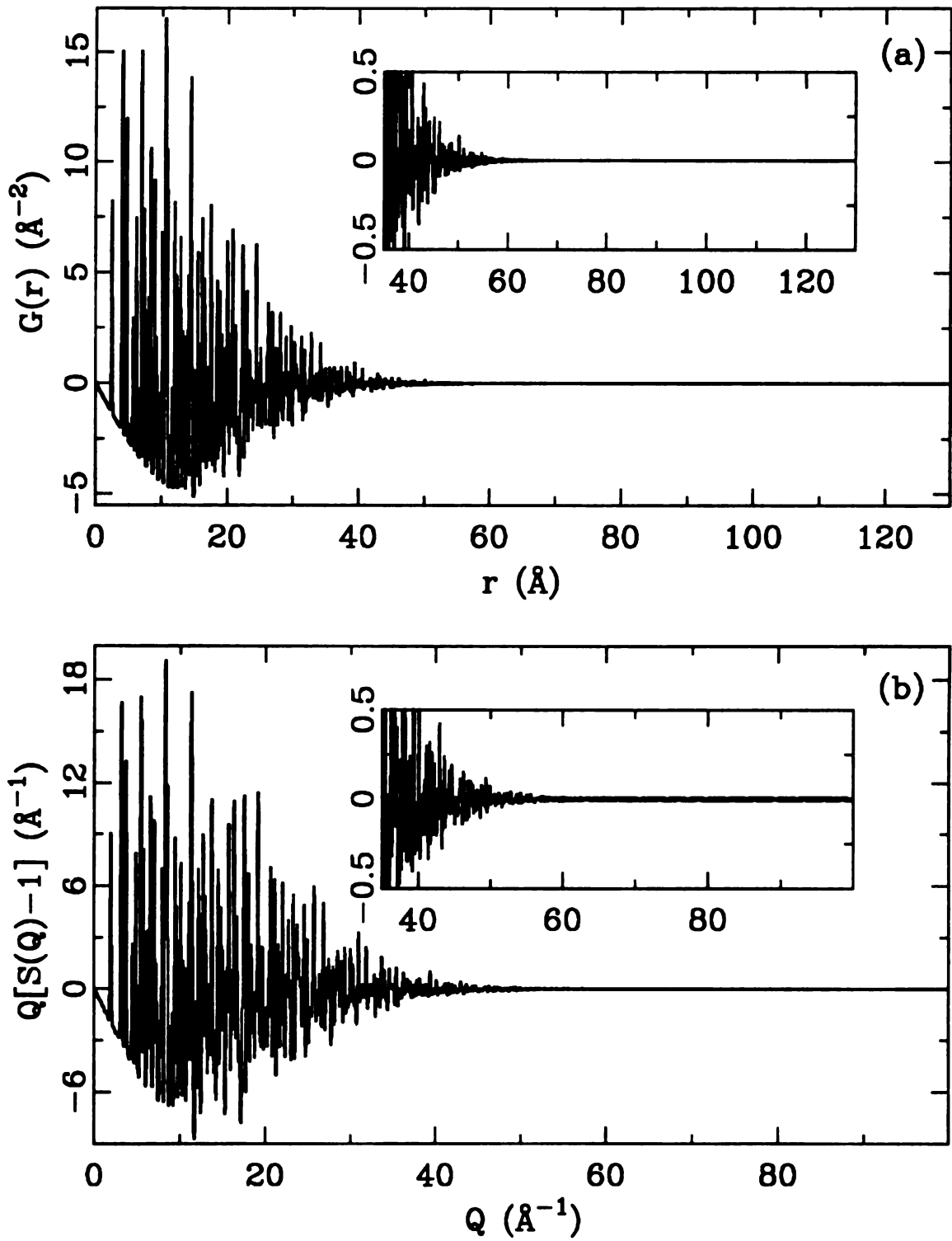


Figure 3.3: Synthetic 10K Germanium PDF (a) as calculated by PDFFIT and resulting $S(Q)$ (b) calculated by Fourier transform. The synthetic data was calculated using parameters to mimic a GLAD measurement.

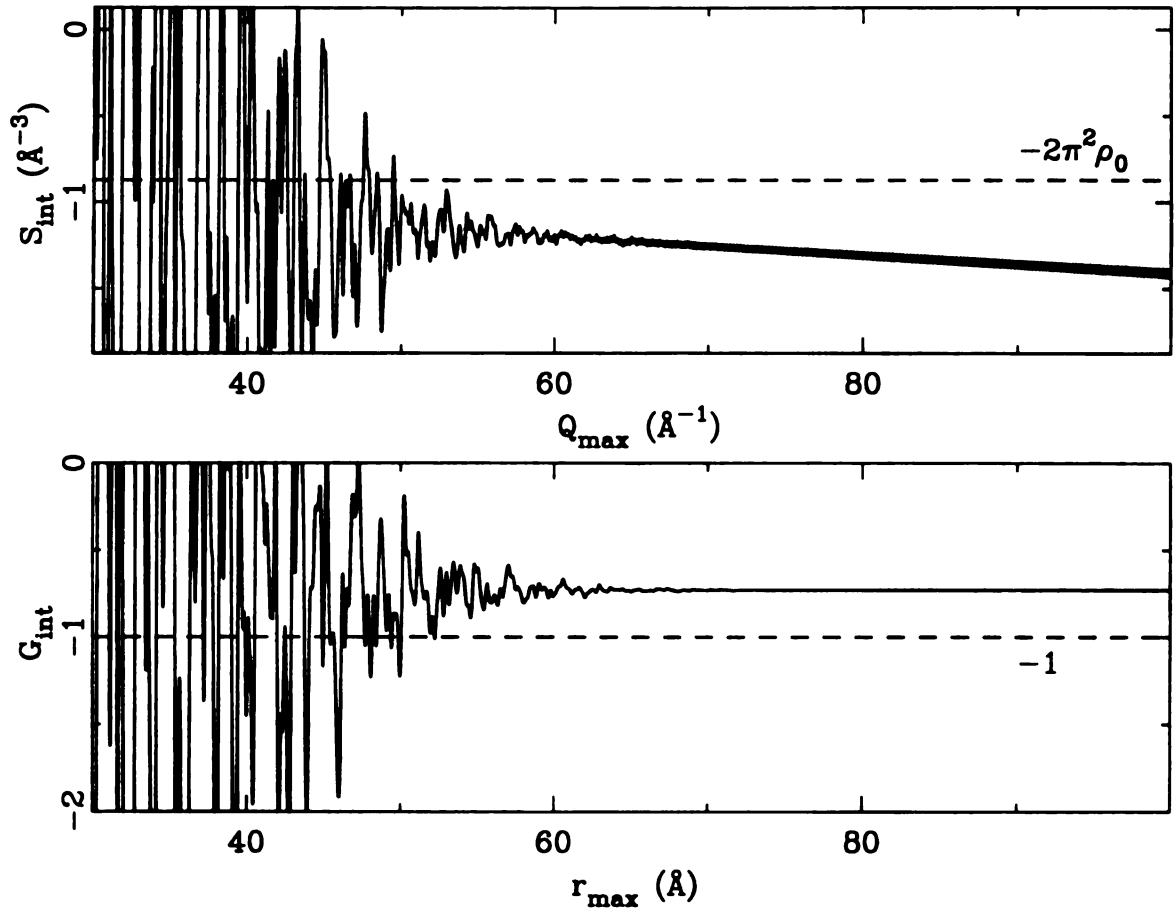


Figure 3.4: Value of S_{int} and G_{int} as a function of Q_{max} and R_{max} respectively. The dotted lines are the theoretical values.

data. Nonetheless, this fact suggests that S_{int} and G_{int} are less valuable quality measures in general, and especially for crystalline materials since they require a very broad measurement range. For this reason they will not be considered further. Besides S_{int} and G_{int} , the values of the other criteria are not more than 3% different from their theoretical values. This also gives the minimum uncertainty in the quality criteria.

Measured spectra tend to have errors which are both random and systematic in nature. Random noise originates from measurement statistics. The other basic type of error is a systematic error. There are many sources of systematic errors, from bad detectors to an unstable source. Systematic errors are normally dealt with by

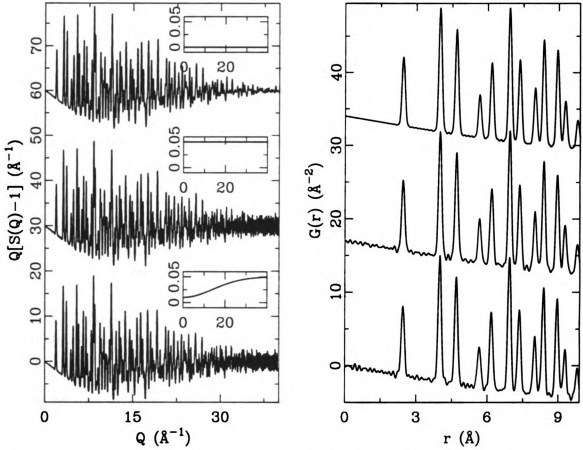


Figure 3.5: Reduced total scattering structure function (left), form of noise dS added to $S(Q)$ (inset), and associated PDFs (right). From top to bottom the synthetic data are pure, constant noise added, Q -dependent noise added.

determining where they come from, fixing the problem and re-measuring.

Frequently it is not possible to re-measure a data-set or the systematic error is subtle enough to not be noticed. In these cases one can either disregard the data or get an idea of its quality and try to understand the underlying physics, knowing that the data does have a systematic error and its effect on the data. The following examples all started from the synthetic data set described above with errors introduced into $S(Q)$ and Fourier transformed using a Q_{max} of 40\AA^{-1} , obtainable at several neutron instruments.

The effect of random noise is handled in two ways, by adding constant noise

| | theory | 100Å ⁻¹ | %diff | 40Å ⁻¹ | %diff |
|--------------|---------|--------------------|-------|-------------------|-------|
| S_{avg} | 1.0000 | 1.0002 | 0.02 | 1.0003 | 0.03 |
| S_{disp} | 1.0000 | 0.9814 | 1.86 | 0.9774 | 2.26 |
| S_{int} | -0.8725 | -0.8614 | 1.27 | -1.5843 | 81.59 |
| G_{int} | -1.0000 | -0.7292 | 27.08 | -0.7286 | 27.14 |
| G_{low} | 0.0000 | 0.0000 | - | 0.0001 | - |
| ρ_{fit} | 0.0442 | 0.0439 | 0.68 | 0.0439 | 0.68 |

Table 3.1: Values of quality criteria unspoiled data with Q_{max} of 100Å⁻¹ and 40Å⁻¹.

| | theory | none | constant | Q -dependent |
|--------------|--------|--------|----------|----------------|
| S_{avg} | 1.0000 | 1.0001 | 0.9999 | 1.0005 |
| S_{disp} | 1.0000 | 0.9772 | 0.9770 | 0.9774 |
| G_{low} | 0.0000 | 0.0001 | 0.0366 | 0.0720 |
| ρ_{fit} | 0.0442 | 0.0439 | 0.0445 | 0.0458 |
| R_{wp} | | 0.0174 | 0.0487 | 0.0492 |

Table 3.2: Values of quality criteria for different amounts of random noise. R_{wp} is calculated between the test data and the ideal PDF.

and noise that increases with Q . Noise is added by adding a random number between $\pm 0.5dS$, where dS is shown in the insets to Figure 3.5 along with the resulting $S(Q)$ s and PDFs. The effect of random noise on the criteria can be seen in Table 3.2. Random noise, of any form, should effect only quality factors which concentrate on the agreement with ideal behavior. As seen in Figure 3.5 the effect of random noise is most easily seen in the regions where there are no PDF peaks. Being average criteria, the values of S_{avg} and S_{disp} do not appreciably change, within the prescribed 3%; the value of G_{low} does.

One might expect the effect of systematic errors on data to be more dramatic than random noise. Since systematic errors carry information, their effect is more complicated than random noise which overall does not greatly affect the PDF peaks. Three types of systematic errors will be presented here. While the source of the errors is not mentioned they are all types of errors that have been seen in real data. The most common systematic error is a scaling error. This comes from the fact that

| α | 0.5 | 1.0 | 2.0 |
|---------------------|--------|--------|--------|
| S_{avg} | 1.0005 | 1.0003 | 0.9999 |
| S_{disp} | 0.4894 | 0.9774 | 1.9557 |
| G_{low} | 0.0000 | 0.0000 | 0.0000 |
| ρ_{fit} | 0.0219 | 0.0439 | 0.0878 |
| S_{disp}/α | 0.9788 | 0.9774 | 0.9778 |
| ρ_{fit}/α | 0.0438 | 0.0439 | 0.0439 |

Table 3.3: Values of quality criteria for various scaling.

diffraction data are inherently arbitrarily scaled. Therefore, this type of systematic error will always be encountered. Many authors have described various techniques for finding either an absolute scale factor [47, 48, 49, 52, 53, 54] or a relative scale factor [38, 39, 55] to compare data sets. When $S(Q)$ is scaled, this changes the asymptotic behavior. To ensure proper asymptotic behavior we set $\beta = 1 - \alpha$, hence

$$S'(Q) = \alpha S(Q) + (1 - \alpha), \quad (3.30)$$

As expected from the analytic result, Equation 3.6, $G'(r) = \alpha G_c(r)$ and $G(r)$ remains undistorted but changes its scale. In principle, therefore, S_{disp} and ρ_{fit} could be used to determine the scale of the data. S_{disp} only requires knowledge of the sample chemical composition and ρ_{fit} only the average sample number density. The effect of scaling can be seen in Figure 3.6 and Table 3.3. By definition, S_{avg} does not change for the three cases within reasonable accuracy, while it is also noticed that G_{low} is scale invariant as well. The other two criteria S_{disp} and ρ_{fit} do vary with scale as seen in the second half of Table 3.3.

We now consider a slowly oscillating additive sine wave that might originate from an imperfectly corrected background. As before we want $S'(Q)$ to have the right asymptotic form, $S_{avg}=1$, so the constant α is changed in such a way that this is satisfied at Q_{max} . This is a common situation in real experimental PDFs: an unknown slowly oscillating additive correction is arbitrarily corrected with a

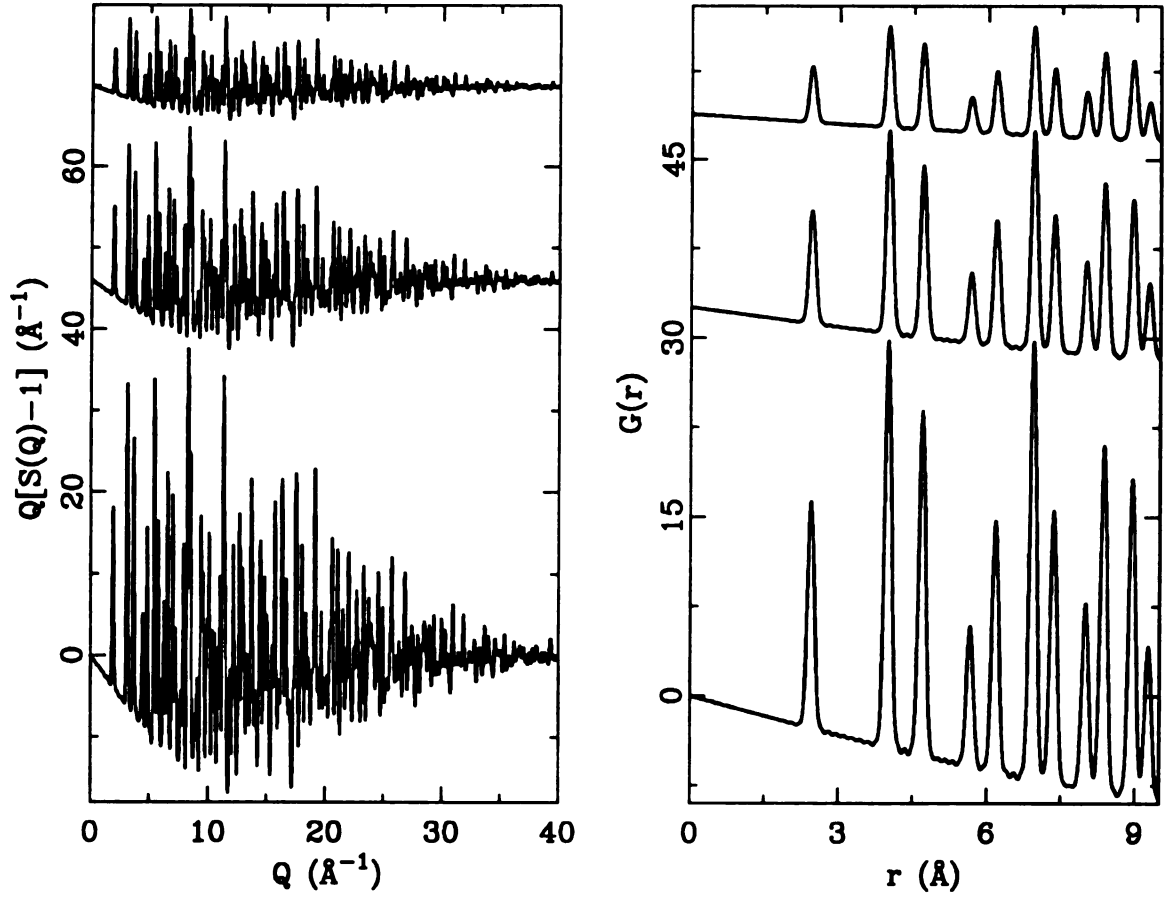


Figure 3.6: $S(Q)$ (left), and associated PDFs (right). From top to bottom the scale, α , is 0.5, 1.0 and 2.0. Both $S(Q)$ and $G(r)$ are offset for clarity.

| error | theory | (a) | (b) | (c) |
|-----------|--------|--------|--------|--------|
| α | - | 0.97 | 1.07 | 0.97 |
| S_{avg} | 1.0000 | 1.0124 | 1.0218 | 1.0129 |
| G_{low} | 0.0000 | 0.0469 | 0.1311 | 0.1507 |
| R_{wp} | - | 0.0175 | 0.0217 | 0.0442 |

Table 3.4: Values of quality criteria for various systematic errors. R_{wp} is calculated between the test data and the appropriately scaled ideal PDF. The three columns are shown in Figures 3.7 and 3.8 as (a), (b), and (c) respectively.

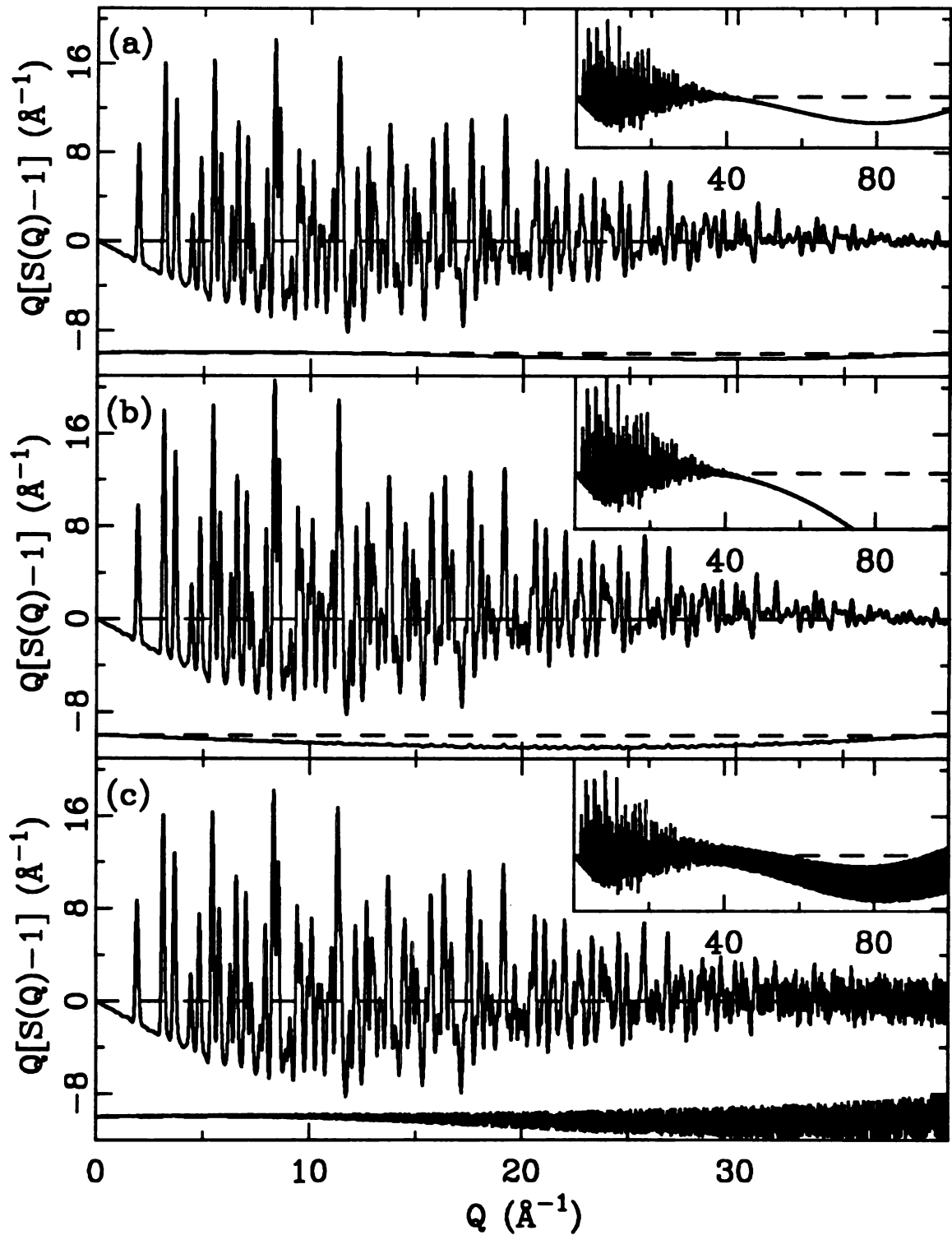


Figure 3.7: $Q[S(Q) - 1]$ for three types of errors, (a) long wavelength sine oscillation, (b) step function, and (c) sine oscillation with Q -dependent random noise. Below each structure function is the difference between the data with and without errors. The insets are the same data plotted from 0\AA^{-1} to 100\AA^{-1} .

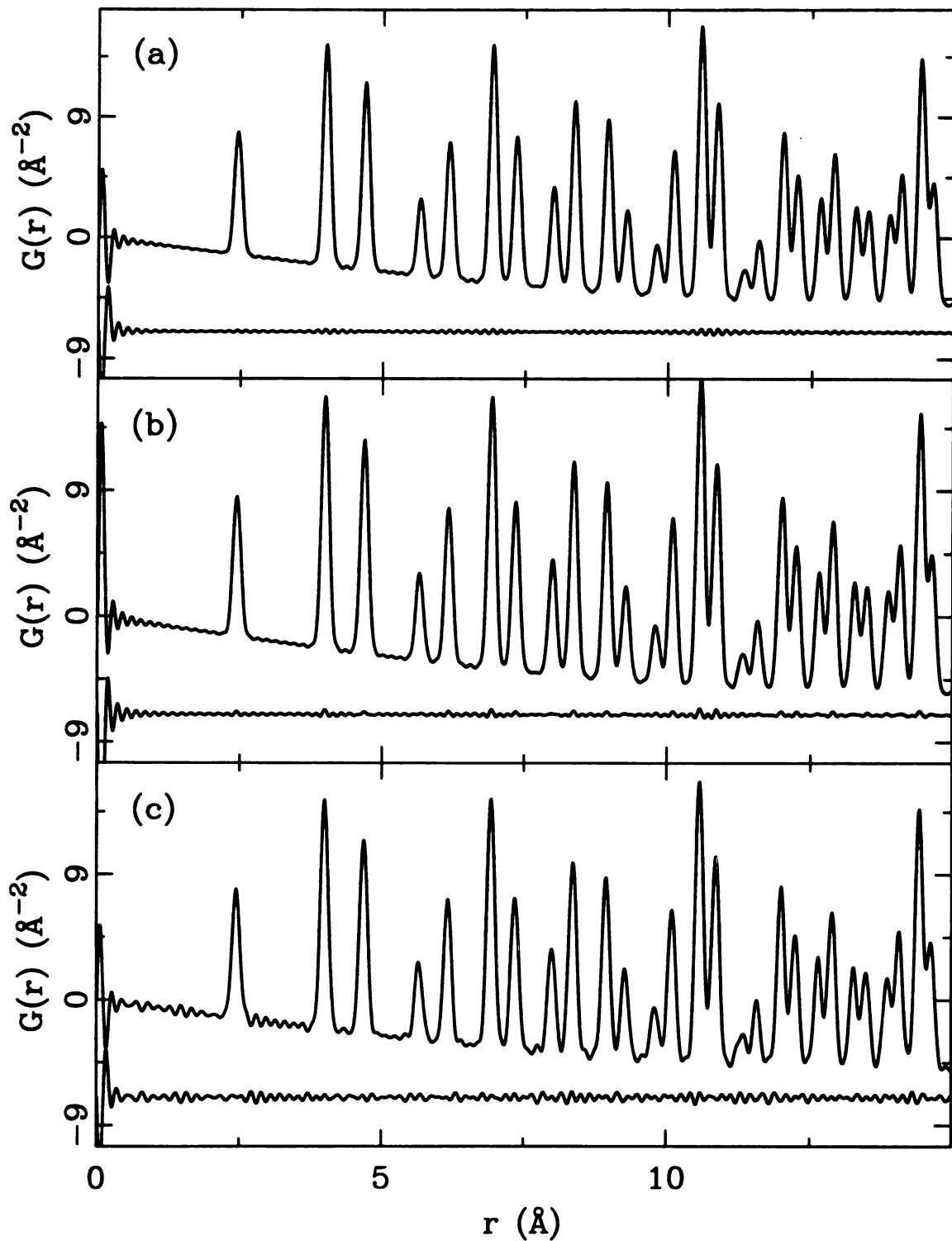


Figure 3.8: $G(r)$ for three types of errors, (a) long wavelength sine oscillation, (b) step function, and (c) sine oscillation with Q -dependent random noise. Below each PDF is the difference between the data with and without errors.

(mostly) multiplicative correction. The exact form of $S'(Q)$ introduced here is

$$S'(Q) = \alpha \left[S(Q) + .1 \sin \left(\frac{2\pi}{100} Q \right) \right] \quad (3.31)$$

The choice of the amplitude (0.1) and wavelength (100\AA^{-1}) were done to produce $S'(Q)$ similar to what is seen with measurements. The reduced total scattering structure function is in Figure 3.7(a) and associated PDF can be seen in Figure 3.8(a) with the quality factors being listed in Table 3.4(a). From Equation 3.6 we expect to see the PDF scaled and low- r ripples due to $\gamma(r)$. While there is little noticeable change in $S(Q)$, the effect on the PDF is quite large. The most interesting feature of this type of systematic error is that it is the first type of error presented here that shows the behavior normally seen in PDF data. That is large peaks near $r = 0\text{\AA}$ and oscillations carrying into the physical portion of the PDF. Both S_{avg} and S_{disp} are within reasonable range of their ideal values while G_{low} varies significantly. This is expected because G_{low} is a quantification of the low- r noise in the PDF.

The third, type of systematic error to be discussed here is a slowly varying multiplicative factor. This type of systematic error would result from an improper multiple scattering correction. The exact form of the function used here is

$$S'(Q) = \alpha S(Q) \left[e^{-\left(\frac{Q}{130}\right)^2} \right] \quad (3.32)$$

The reduced total scattering structure function is in Figure 3.7(b) and associated PDF can be seen in Figure 3.8(b) with the quality factors being listed in Table 3.4(b). In this case the value of S_{disp} is less than one because this systematic error suppresses the high- Q intensity. There is also a clear effect on the low- r portion of the PDF due to this effect, illustrating the next point: the low- r portion of the PDF is related to high- Q .

For completeness, the fourth spoiling of the synthetic data was done by introducing both Q -dependent random noise and a sine wave oscillation. The results of this synthetic data can be seen in Figure 3.7(c) and 3.8(c) with some of the quality factors listed in Table 3.4(c).

From these seven examples we know which quality criteria are most useful. S_{int} and G_{int} are not working on the test data, and even if they were they are still not useful for measurements of crystalline materials due to the large measurement range required. S_{disp} and ρ_{fit} were determined to be scale dependent. While this dependence could be used to achieve a proper relative scale between data sets, which is outside the scope of this paper, the necessity of knowing the scale of the data makes these two less useful. This leaves S_{avg} and G_{low} as the preferred criteria. For perfect data, S_{avg} and G_{low} are equivalent. However, for real data G_{low} is a more robust criterion. In the next section these criteria, S_{avg} and G_{low} , will be tested with *real* data and be used to determine the best pair of parameters to adjust to optimize a PDF.

3.4 Data Analysis Protocols

Time of flight neutron powder diffraction data were measured using GLAD at IPNS at Argonne National Laboratory. Finely powdered Germanium was sealed inside an extruded cylindrical vanadium container with He exchange gas. The sample weighed 4.472g and filled a container (0.9272cm diameter and 5.4cm high) to a height of 4.0cm. We therefore estimate the mass density of the powder sample to be 1.7g/cm³. This was mounted on a closed cycle helium refrigerator. Neutron powder diffraction data were measured at 10K for 4 hours with a collimator 0.4636cm wide. Parasitic scattering from the heat-shields was estimated by taking data with the sample environment in place but no sample at the sample position.

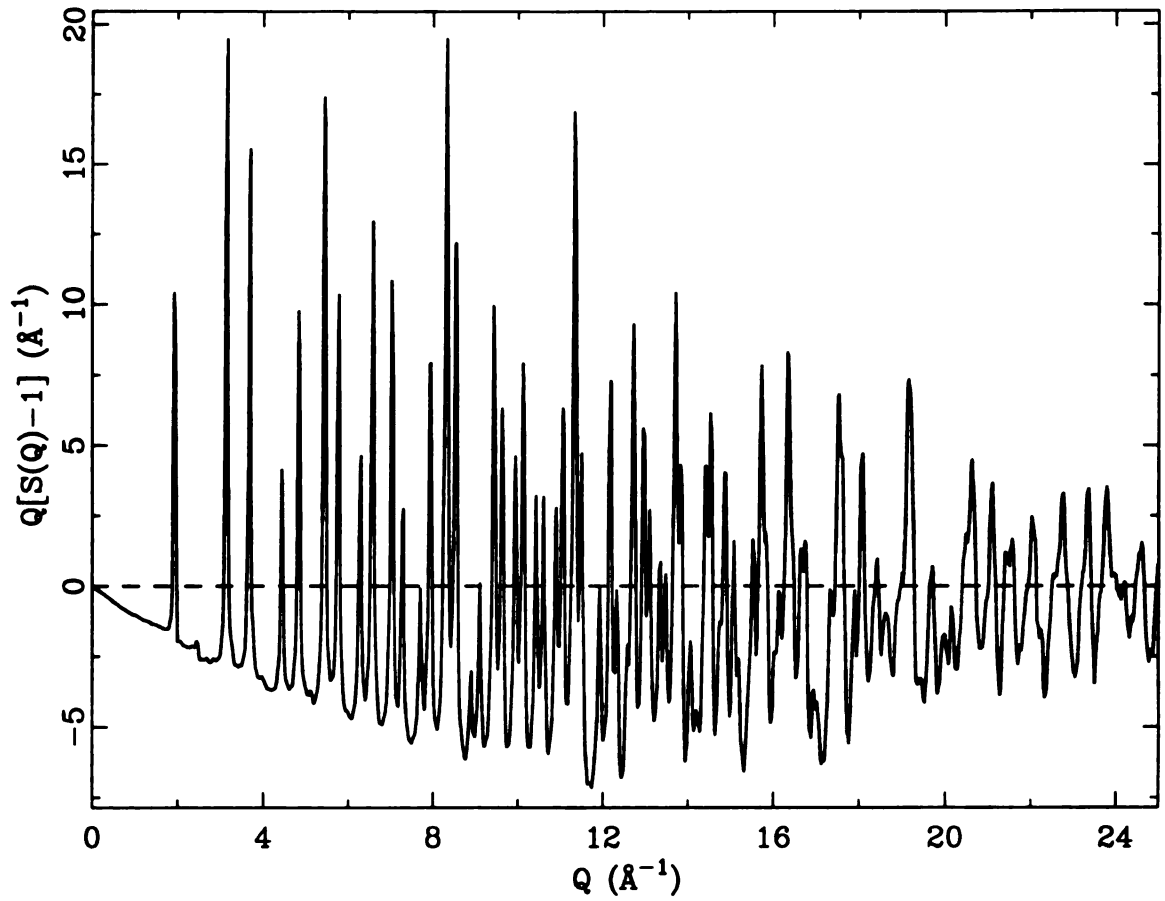


Figure 3.9: Representative reduced total scattering structure factor for Germanium at 10K measured using GLAD at IPNS.

Scattering from the sample container was measured from an empty container. The scattering from a vanadium rod was also measured to allow the data to be normalized for the incident spectrum and detector efficiencies. Standard data corrections were carried out as described elsewhere [24, 40] using the program PDFgetN. [30] A representative reduced total scattering structure factor ($Q[S(Q) - 1]$) is shown in Figure 3.9 and Fourier transformed using $Q_{max}=25\text{\AA}^{-1}$ to produce the PDF shown in Figure 3.10 as the open circles.

The data were modeled using PDFFIT. [34] Pure Germanium is a diamond structure ($F\bar{4}3m$ with atoms at $[0,0,0]$ and $[\frac{1}{4}, \frac{1}{4}, \frac{1}{4}]$). The structure refinement was carried out over the range of $2\text{\AA} < r < 15\text{\AA}$ using the following method. The starting

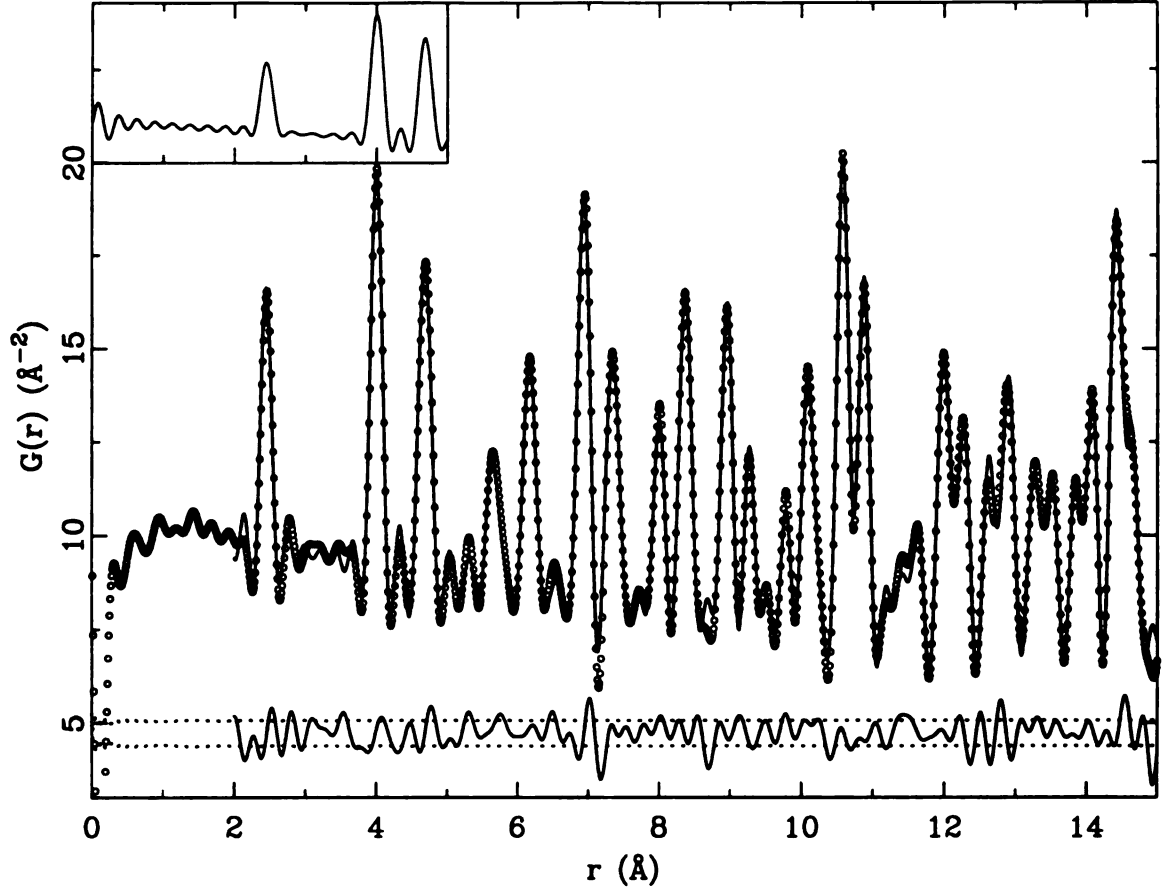


Figure 3.10: Representative PDF (circles), PDFFIT model (line) and difference curve with 2σ error bars as dotted lines (below) for Germanium at 10K measured using GLAD at IPNS. The sine systematic error with Q -dependent noise test data with Q_{max} of 25\AA^{-1} (inset) is also shown for comparison.

structure was a crystal structure with lattice parameter of 5.66\AA and Germanium atoms only at the symmetric sites. The anisotropic thermal factors were set to be equal ($U_{11} = U_{22} = U_{33} = 0.0021\text{\AA}^2$). Then the refinement proceeded by varying parameters in five steps:

1. The scale factor (N_m), Q -resolution ($qsig[1]$), and Q -dependent sharpening ($delt[1]$) are varied.
2. N_m , $delt[1]$ and the lattice parameter ($latt[i]$) are varied.
3. N_m , $qsig[1]$, $delt[1]$, and $latt[i]$ are varied.

4. isotropic thermal factor ($u[i,j]$) is varied

5. N_m , $latt[i]$, and $u[i,j]$ are varied.

This method was repeated for all data, however processed, to obtain values of N and R_{wp} that were reproducible. A representative fit is shown in Figure 3.10 as the solid line. A difference curve is shown beneath the data. Notice the unphysical peak in the experimental PDF at very low- r coming from the imperfect data corrections. Also, note that the structural information is not affected in a significant way by this feature.

3.4.1 Methods of Optimizing PDFs

When processing a given run there are multiple ways which the processing parameters can be varied to minimize G_{low} . This discussion is better understood by looking at Table 3.5 The first refined column is that done by using the physical values for all of the parameters. While this does represent the experimental setup it clearly is not the best PDF. Traditionally one adjusts the effective sample density, ρ_{eff} , the effective beam width, σ_{eff} , or both to obtain the optimal PDF. Two of the more common methods of adjusting ρ_{eff} and σ_{eff} , seen in the first half of Table 3.5 are

- vary ρ_{eff}
- reduce σ_{eff} to reflect beam profile then adjust ρ_{eff} accordingly

These methods allow for obtaining an optimal PDF for a particular measurement, but the relative scale of the data is set by other means. While the topic of scale is outside the scope of this work, it should be taken into account, in general, when processing data. Normally an experiment is performed where multiple data sets are compared rather than individual runs independent of other measurements. The

scale of the runs is determined when using the above methods to minimize G_{low} because ρ_{eff} and σ_{eff} are used in predominantly multiplicative corrections. In order to scale the data and minimize G_{low} both multiplicative and additive processing parameters are needed.

In Equation 3.6 the parameters α and β were introduced. While α has a multiplicative effect like ρ_{eff} and σ_{eff} , β allows for optimizing the PDF without affecting the scale. β can be combined with the different multiplicative factors as follows

- vary α and β
- vary ρ_{eff} and β
- vary σ_{eff} and β

The effect of these parameters is seen in the second half of Table 3.5 The multiplicative factor in these cases was chosen to produce $N_m = 1$ to demonstrate the ability of scale selection.

As seen in the five columns of Table 3.5 that are associated with these methods the values of R_{wp} , a and $\langle U \rangle$ are all near identical. While the values of S_{avg} and G_{low} vary between the two halves of the table, there are some tendencies. The value of S_{avg} is distinctly less than its ideal value of one and G_{low} is between two and three for the optimized PDFs. Because all of the criteria are in fairly good agreement, it is hard to chose one which one is the best. The optimization methods that utilize β have the obvious advantage of being able to decide the scale factor which makes them more desirable methods. As seen in Sec. 3.3.2, varying α and β when $\beta = 1 - \alpha$ allows the scale to be varied without changing the quality of the PDF. For this reason, using α and β is the recommended method.

| | theory | traditional methods | | | multiplicative and β | | |
|---------------------|--------|---------------------|-------------|-------------|----------------------------|-------------|-------------|
| α | 1.0000 | 1.0000 | 1.0000 | 1.0000 | 1.6107 | 1.0000 | 1.0000 |
| β | 0.0000 | 0.0000 | 0.0000 | 0.0000 | -0.6550 | -0.6800 | -0.6780 |
| ρ_{eff} | 1.7 | 1.7 | 1.2427 | 1.5799 | 1.2427 | 0.7484 | 1.2427 |
| σ_{eff} | 0.4636 | 0.4636 | 0.4636 | 0.4173 | 0.4636 | 0.4636 | 0.3623 |
| S_{avg} | 1.0000 | 0.7246 | 0.9894 | 0.9649 | 0.9394 | 0.9419 | 0.9411 |
| G_{low} | 0.0000 | 106.8844 | 3.0028 | 2.1319 | 2.1720 | 2.0487 | 2.0714 |
| N_m | | 0.462(4) | 0.6225(15) | 0.6088(16) | 0.9994(25) | 1.000(3) | 0.999(3) |
| R_{wp} | | 0.2836 | 0.1219 | 0.1261 | 0.1265 | 0.1268 | 0.1267 |
| a | | 5.6578(3) | 5.65789(11) | 5.65790(11) | 5.65790(11) | 5.65789(11) | 5.65789(11) |
| $\langle U \rangle$ | | 0.002151(21) | 0.002137(6) | 0.002134(6) | 0.002134(6) | 0.002134(6) | 0.002164(6) |

Table 3.5: Results of varying different parameters. The traditional method columns, in order, are done by using physical parameters, varying ρ_{eff} to minimize G_{low} , and reducing σ_{eff} then varying ρ_{eff} to minimize G_{low} . The second half of the table is done by varying α , ρ_{eff} , and σ_{eff} with β to obtain $N_m = 1$ and minimize G_{low} .

3.5 Summary

Errors in scattering data, both random and systematic, have an effect on the low- r region of the PDF. To determine the quality of PDF data various criteria were introduced. The quality criteria (S_{avg} , S_{disp} , G_{low} , and ρ_{fit}) were compared to synthetic data with different errors to demonstrate what each criterion is sensitive to. Tests with synthetic data show that S_{disp} and ρ_{fit} vary with scale while S_{avg} and G_{low} do not. This is important for finding the optimal processing parameters for a given data set. Future work should be done to find a more appropriate version of both S_{avg} and S_{disp} since both methods are using averaging over a range rather than a fitting method to determine their values. Finally, real data was optimized using different methods only to find that no one method obtains better results, however, the use of α and β is preferable.

Chapter 4: Local Bond Length

Mismatch in $\text{ZnSe}_{1-x}\text{Te}_x$

4.1 Introduction

The study of alloys is complicated by the fact that considerable local atomic strains are present due to the disordering effect of the alloying. This means that local bond-lengths can differ from those inferred from the average (crystallographic) structure by as much as 0.1 Å. [10, 11] This clearly has a significant effect on calculations of electronic and transport properties. [5] To fully characterize the structure of these alloys it is necessary to augment crystallography with local structural measurements. In the past the extended x-ray absorption fine structure (EXAFS) technique has been extensively used. [3, 10, 13] More recently the atomic pair distribution function (PDF) analysis of powder diffraction data has also been applied to get additional local structural information from $\text{In}_x\text{Ga}_{1-x}\text{As}$ alloys. [11, 14, 15] In that case high energy x-rays combined with good resolution and a wide range of momentum transfer allow the In-As and Ga-As nearest neighbor peaks to be resolved. In this Chapter we describe PDF measurements of the II-VI alloy $\text{ZnSe}_{1-x}\text{Te}_x$ from neutron powder diffraction measurements using the new General Materials Diffractometer (GEM) at ISIS. In these measurements the distinct Zn-Se and Zn-Te bonds, which differ in length by just $\Delta r = 0.14$ Å, could be distinguished demonstrating the quality of the data from GEM.

Both ZnTe and ZnSe have the zinc-blende structure ($F\bar{4}3m$) where the Zn atoms and Te, Se atoms occupy the two interpenetrating face-centered-cubic (fcc) lattices as seen in Figure 4.1. In the alloys the lattice parameter of $\text{ZnSe}_{1-x}\text{Te}_x$ interpolates linearly between the end member values consistent with Vegard's

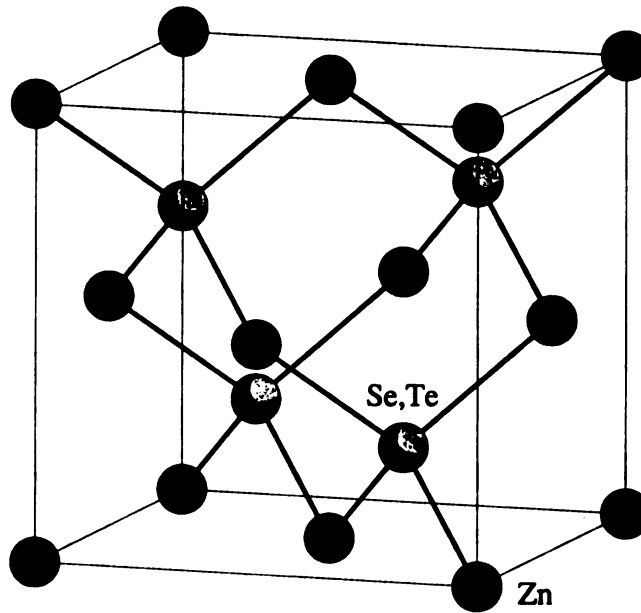


Figure 4.1: The zinc-blende structure shown with conventional unit cell.

law. [9] However, both EXAFS experiments [3, 13] and theory [1, 56, 57, 58] show that the atomic nearest neighbor (nn) distances deviate strongly from Vegard's law. Rather, they stay closer to their natural lengths found in the end-member compounds: $L_{\text{Zn-Te}}^0 = 2.643(2)\text{\AA}$ and $L_{\text{Zn-Se}}^0 = 2.452(2)\text{\AA}$.

A limitation of the EXAFS method for studying the local structure of alloys is that it only gives information about the first and second neighbor bond-lengths and information about the bond-length distributions with less accuracy. Here PDF analysis of neutron powder diffraction data is used. As was discussed in earlier chapters the total scattering structure function includes both the Bragg and diffuse scattering, the PDF contains both *local* and *average* atomic structure yielding accurate information on short and intermediate length-scales. Previous high resolution PDF studies on $\text{In}_x\text{Ga}_{1-x}\text{As}$ were carried out using high energy x-ray diffraction. [11, 15] This yielded data over a wide Q -range (Q is the magnitude of the scattering vector) which resulted in the very high real-space resolution required

to separate the nearest neighbor peaks from In-As and Ga-As. The high Q -range coverage and Q -space resolution of the GEM Diffractometer allowed us, for the first time, to obtain similarly high real space resolution PDFs of $\text{ZnSe}_{1-x}\text{Te}_x$ using neutrons and to resolve the Zn-Se and Zn-Te bonds that differ in length by only 0.14 Å. Furthermore, the data collection time was only sixty minutes compared to the 12 hours for the x-ray data with similar quality. The nn distances and average peak widths are fit using model independent techniques to better understand the local and intermediate structure. The PDFs of the full alloy series have been calculated using a model based on the Kirkwood potential giving excellent agreement over a wide range of r with no adjustable parameters.

4.2 Experimental

4.2.1 Synthesis and Characterization

The powder samples were made in collaboration with Hyung-sook Choi and Professor M. G. Kanatzidis in the Chemistry Department at Michigan State University. Finely powdered samples of ~10g of $\text{ZnSe}_{1-x}\text{Te}_x$ were made with $x = \frac{1}{6}, \frac{2}{6}, \frac{3}{6}, \frac{4}{6}, \frac{5}{6}$. The starting reagents (zinc selenide, metal basis, 99.995%; zinc telluride, metal basis, 99.999%) were finely ground, mixed in the correct stoichiometry, and sealed in quartz tubes under vacuum. The samples were then heated at 900°C for 12-16 hours. [59] This procedure (grinding, vacuum sealing, and heating) was repeated four times to obtain high quality homogeneous products. The colors of the solid solutions vary gradually from dark red (ZnTe) to yellow (ZnSe) as the x -value decreases reflecting the band-gap of the alloy samples smoothly changing in the optical frequency range. The homogeneity of the samples was checked using x-ray diffraction by monitoring the width and line-shape of the $\langle 400 \rangle$, $\langle 331 \rangle$, $\langle 420 \rangle$, and $\langle 422 \rangle$ Bragg peaks measured on a rotating anode Cu K_α source. Finely powdered

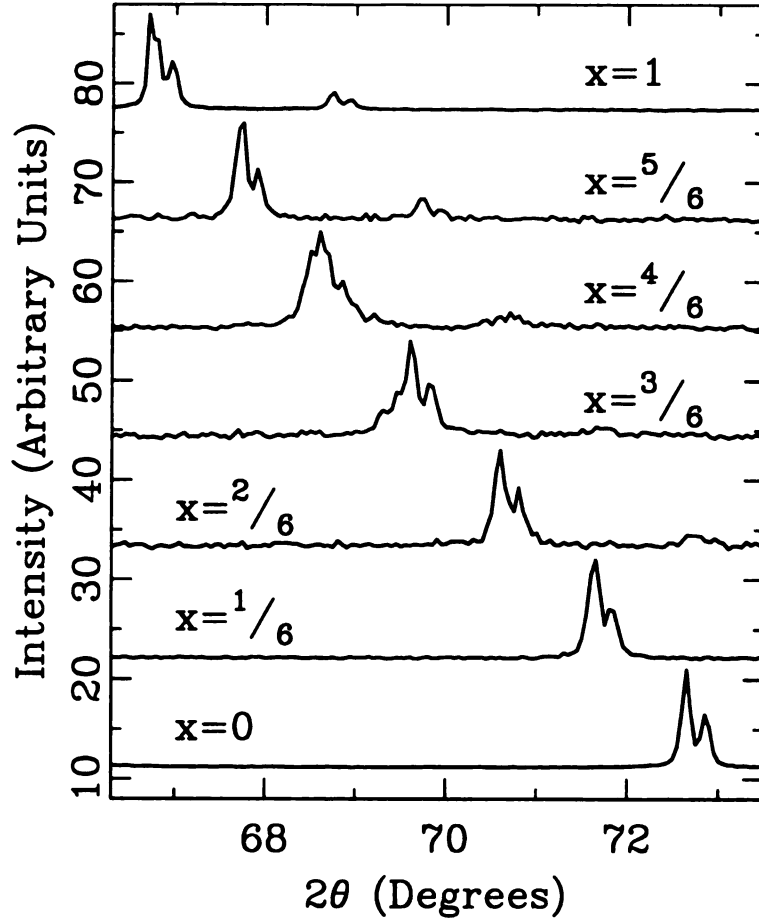


Figure 4.2: $\langle 331 \rangle$ and weak $\langle 420 \rangle$ peaks of $\text{ZnSe}_{1-x}\text{Te}_x$ measured at 300K using Cu rotating anode.

samples were sieved through a 200-mesh sieve then packed into flat plates and measured in symmetric reflection geometry. The $\langle 331 \rangle$ and (weak on high angle side) $\langle 420 \rangle$ peaks are reproduced in Figure 4.2. The double-peaked shape comes from the $K_{\alpha 1}$ and $K_{\alpha 2}$ components in the incident beam. The line-widths are narrow and smoothly interpolate in position between the positions of the end-members verifying the homogeneity of the samples.

T

diffrac

Labor

sealed

cold-

rese

atta

bro

con

all

va

sp

de

A:

th

co

of

wer

exp

rath

end-

 Q_{max}

evid

detec

yildi

4.2.2 Neutron Measurements and Data Processing

Time of flight neutron powder diffraction data were measured on the GEM diffractometer at the ISIS spallation neutron source at Rutherford Appleton Laboratory in Oxfordshire, UK. The finely powdered $\text{ZnSe}_{1-x}\text{Te}_x$ samples were sealed inside extruded cylindrical vanadium containers. These were mounted on the cold-stage of a helium cryostat immersed in cold He gas in contact with a liquid He reservoir. The temperature of the samples was maintained at 10K using a heater attached to the cold-stage adjacent to the sample. 10K was used to minimize broadening of the PDF peaks due to thermal effects. The empty cryostat, an empty container mounted on the cryostat and the empty instrument were all measured, allowing us to assess and subtract instrumental backgrounds. The scattering from a vanadium rod was also measured to allow the data to be normalized for the incident spectrum and detector efficiencies. Standard data corrections were carried out as described in Chapter 2 and elsewhere [24, 40] using the program PDFgetN. [30] After being corrected the data are normalized by the total scattering cross-section of the sample to yield the total scattering structure function, $S(Q)$. This is then converted to the PDF, $G(r)$, by a Sine Fourier transform according to Eq. 2.14.

The GEM instrument yields useful diffraction information up to a maximum Q of greater than 90 \AA^{-1} . Unfortunately, due to a neutron resonance in Tellurium we were forced to terminate the Fourier transform at a maximum Q of 40 \AA^{-1} in this experiment. This resulted in nn peaks in these alloys which are resolution limited rather than sample limited. This was verified by Fourier transforming the ZnSe end-member at higher values of Q_{max} . The nn peak kept getting sharper up to $Q_{max} = 60 \text{ \AA}^{-1}$. Nonetheless, the distinct short and long bond distances are still evident in the alloy PDFs. At the time of this measurement the backscattering detector banks on GEM were not operational. With the backscattering banks yielding better statistics in high Q and adding detector coverage, one might expect

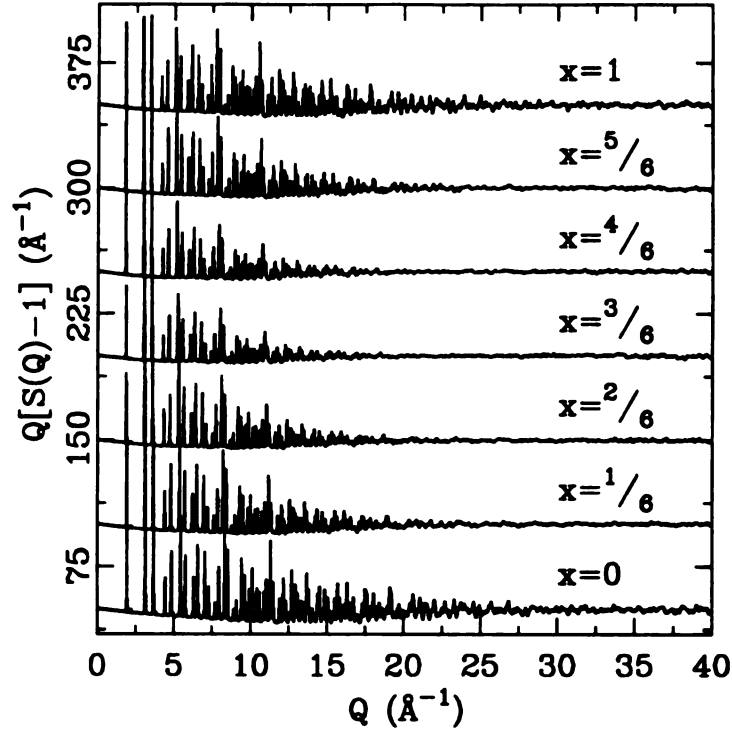


Figure 4.3: $Q[S(Q) - 1]$ for $\text{ZnSe}_{1-x}\text{Te}_x$ measured at 10K.

to get similar quality PDFs in a fraction of the time. The reduced structure functions, $Q[S(Q) - 1]$, obtained from the $\text{ZnSe}_{1-x}\text{Te}_x$ samples are shown in Figure 4.3 and the resulting PDFs are shown in Figure 4.4.

4.2.3 Method of Modeling

We have used three approaches to obtain structural information from the PDF. First, we carry out a model independent analysis by fitting Gaussian functions to peaks in the RDF. Next we calculate the PDF expected from the average crystal structure using the methods described in Chapter 2. Using a least squares approach, atomic displacement (thermal) parameters are then refined to obtain empirically the PDF peak widths in the alloys. This was done using the PDF refinement program PDFFIT. [34] Finally, we calculate the PDF from a Kirkwood potential based model where the atom positions and thermal broadenings are fully

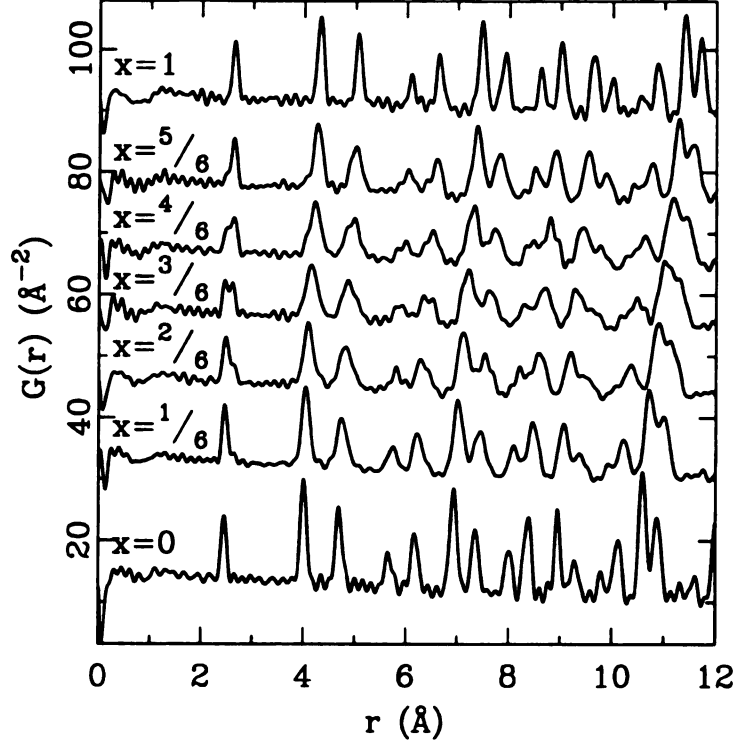


Figure 4.4: $G(r) = 4\pi r(\rho(r) - \rho_0)$ for $\text{ZnSe}_{1-x}\text{Te}_x$ measured at 10K.

determined by the atomic potential parameters.

The Zn-Se and Zn-Te nn distances in the alloys were found by fitting two Gaussians, convoluted with termination functions to account for the termination effects, to the nearest neighbor peak in the RDF. Peak positions and widths were varied. The relative peak intensities were constrained to those expected from the alloy composition. The widths refined to the same values as the end-members within the errors for all the alloys. We thus repeated the fits constraining the peak widths to have the values refined from the end-member RDFs. This more highly constrained fitting procedure resulted in less scatter in the refined peak positions.

To find the far neighbor peak widths PDFFIT [34] was used. The zinc-blende crystal structure was used with all the atoms constrained to lie on their average positions. Lattice parameters, scale factor, isotropic thermal factors, and r -dependent PDF peak broadening parameters [34, 60] were allowed to vary but the

atoms were not allowed to move off the symmetry sites. In this way, all of the atomic disorder, static and dynamic, is included in the refined thermal factors that are giving an empirical measure of the PDF peak widths at higher- r . This approach is better than fitting unconstrained Gaussians because of the problem of PDF peak overlap at higher distances. Clearly this approach does not result in a good model for the alloy structure but will yield a good fit to the intermediate PDF in the alloys. However, it should give reliable empirical estimates of the width of high- r PDF peaks, even when they are strongly overlapped, and allows us to separate the disorder on the cation and anion sublattices. The PDFs were fit over the range of 3 to 15 Å⁻¹. This range was selected so the global properties of the alloys could be fit without influence from the nn behavior.

Potential based modeling to yield realistic alloy structures has been carried out using a model based on the Kirkwood potential. [61] This procedure has been described in detail elsewhere. [1, 56, 62, 63] The model consists of 512 atoms arranged in the zinc-blende structure with periodic boundary conditions where the interatomic force is described by the Kirkwood potential. The system is then relaxed by moving atoms to minimize the energy.

The Kirkwood potential can be written as,

$$V = \frac{\alpha}{2} \sum_{ij} (L_{ij} - L_{ij}^0)^2 + \frac{\beta}{8} L_e^2 \sum_{ijk} \left(\cos \theta_{ijk} + \frac{1}{3} \right)^2, \quad (4.1)$$

where L_e^2 is the nn bond length of an undistorted reference crystal structure, L_{ij} is the length of the bond between the atoms i and j , and L_{ij}^0 is the natural

bond-length. In this definition the bond-stretching, α , and bond-bending, β , force constants have the same units and $\theta_{ijk} = \arccos(-\frac{1}{3})$, for an ideal tetrahedron.

Literature values [1] were used for the bond-stretching and bond-bending parameters obtained from elastic constant measurements. We also tried optimizing α and β by

| | α (N/m) | β (N/m) | β/α | a^{**} |
|------|----------------|---------------|----------------|----------|
| ZnSe | 33.7 | 4.6 | 0.14 | 0.78 |
| ZnTe | 31.1 | 4.7 | 0.15 | 0.76 |
| InAs | 35.1 | 5.8 | 0.16 | 0.74 |
| GaAs | 44.3 | 9.2 | 0.21 | 0.70 |

Table 4.1: α and β reported for $\text{ZnSe}_{1-x}\text{Te}_x$ and $\text{In}_x\text{Ga}_{1-x}\text{As}$. [1]

fitting to the ZnSe and ZnTe end-member PDFs; however, the PDFs calculated using both sets of parameters gave comparable agreement when compared to the alloy data so we simply report the results obtained with the literature values of α and β . The values of α and β for ZnTe and ZnSe used are shown in Table 4.2.3.

The PDFs for the alloys are calculated with no adjustable parameters using the same potential parameters used for the end-members. The additional bond-bending parameters present in the alloy due to Te-Zn-Se type configurations are determined as a geometric mean of the β parameters for the end-members. [62] The thermal broadening of the PDF is calculated by determining the dynamical matrix from the potential and projecting out the atomic displacement amplitudes for each phonon. [62]

4.3 Results and Discussion

4.3.1 Model Independent Results

Upon inspection of the PDFs presented in Figure 4.4 one will immediately notice the splitting of the first peak. This comes from the fact that the nn distances of Zn-Te and Zn-Se stay close to the end-member values of 2.643(2)Å and 2.452(2)Å respectively. The positions of each component of the doublet were determined by fitting Gaussians as described above. The values for the nn bond-lengths are shown as filled circles with 2σ error bars in Figure 4.5. Also plotted in the same Figure as

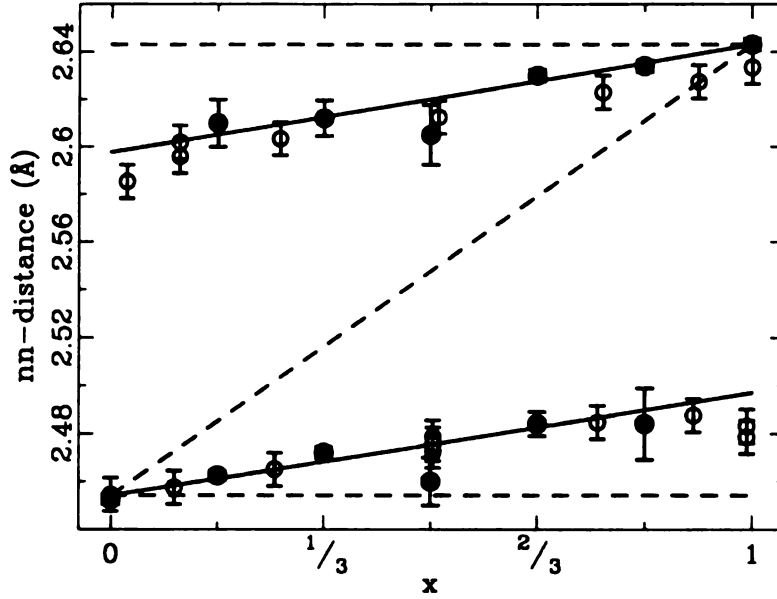


Figure 4.5: nn positions from the PDF (●), EXAFS data [3] (○), and Kirkwood model z-plot (solid line) [1] as a function of composition, x , for $\text{ZnSe}_{1-x}\text{Te}_x$. The angled dashed line is the average nn distance. The horizontal dashed lines are at the end-member distances for comparison. Note that not all EXAFS points had reported error bars so they were all set to the same value.

open circles are the nn bond-lengths determined from an earlier EXAFS study by Boyce and Mikkelsen. [3] There is clearly excellent agreement between the two results. Superimposed on the data are lines which are the predictions of the Kirkwood model for the nearest neighbor bond-lengths using the potential parameters given in Table 4.2.3. [1] Again, there is excellent agreement with the data with no adjustable parameters.

In contrast to the local structure, the long-range structure is well described by the virtual crystal approximation (VCA). [64, 65] The VCA assumes that the structural properties of a crystal alloy all are a linear interpolation of the end-member values. If this were true in semiconductor alloys then not only would one be able to find the lattice parameter of the alloy from Vegard's law but the nn distance would be, for zinc-blende crystals $A_{1-x}B_xC$, $L_{AC} = L_{BC} = \frac{\sqrt{3}}{4}a$. This is shown in Figure 4.5 as the angled dashed line.

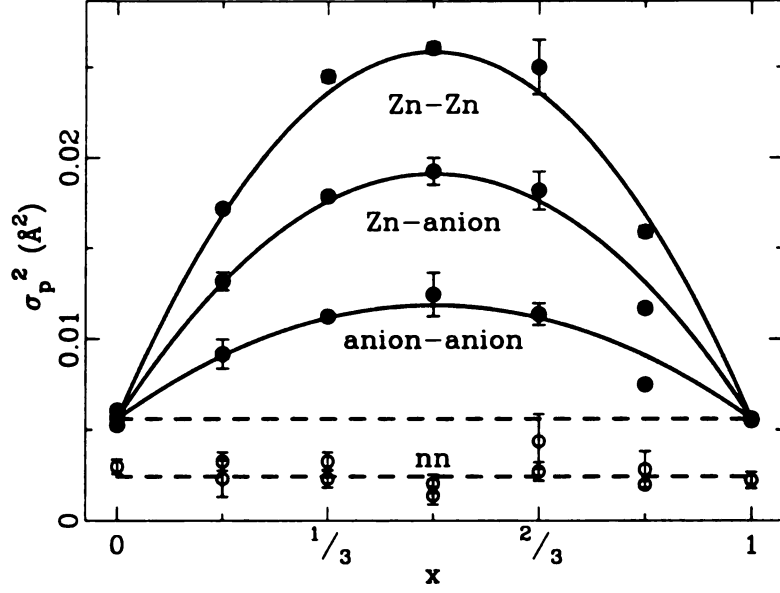


Figure 4.6: Square of the PDF peak widths for near (\circ) and far (\bullet) neighbors as a function of composition, x . The extracted values are plotted with parabolas (lines) to guide the eye. The upper dotted line is at 0.0056\AA^2 and the lower is at 0.0024\AA^2 .

It is clear that the local bond-lengths remain closer to those in the end-members than to the prediction of Vegard's law. In fact the bond-lengths stay close to the Pauling limit [66] in which they would remain completely unchanged in length across the alloy series. The deviation from the Pauling limit is attributed to the disorder in the force constants as we describe below.

The difference in the local structure of the alloys leads to a large amount of atomic strain resulting in much broader PDF peaks in the high- r region of the PDF. In Figure 4.6 the strain is quantified. Little strain is seen in the nn distribution as characterized by the lack of appreciable dispersion in the nn peak widths. The dotted line at $\sigma_p^2 = 0.0056\text{\AA}^2$ represents the mean square width of the PDF peak, σ_p^2 , attributed to the thermal motion of the atoms while the parabolas indicate additional peak broadening due entirely to static strain in the system. The largest peak broadening is seen in the mean-square width of the Zn-Zn peaks (cation-cation) which is as much as $5\times$ as large as the mean-square width due to

thermal broadening and zero-point motion at 10 K. It is also evident that the disorder is larger on the unalloyed (Zn) sublattice than the mixed (Se,Te) sublattice similar to the observation in $\text{In}_x\text{Ga}_{1-x}\text{As}$. [11, 15]

4.3.2 Kirkwood Model

The Kirkwood potential [61] is widely used to describe semiconductor alloys. Petkov *et al.* [11] showed that the Kirkwood model is good at describing $\text{In}_x\text{Ga}_{1-x}\text{As}$, a III-V semiconductor. $\text{ZnSe}_{1-x}\text{Te}_x$ is a II-VI semiconductor so it is of great interest to know whether or not the Kirkwood model is equally successful for this more polar semiconductor alloy. The values of α and β used in this study are shown in Table 4.2.3 with appropriate values for $\text{In}_x\text{Ga}_{1-x}\text{As}$ for comparison.

Other quantities of note are the ratio, β/α , and the topological rigidity parameter, a^{**} , [56] which is a function of β/α :

$$a^{**} = \frac{1 + 1.25(\beta/\alpha)}{1 + 3.6(\beta/\alpha) + 1.17(\beta/\alpha)^2}. \quad (4.2)$$

The topological rigidity parameter, a^{**} , can vary from 0 to 1 and quantifies the effect of the lattice. The Pauling limit results when $a^{**}=1$, the floppy lattice limit. If $a^{**}=0$ the lattice is rigid and Vegard's law will hold true locally as well as globally. As can be seen in Table 4.2.3, the values found for a^{**} are close to 0.75 which appears to be fairly universal for all semiconductors. [56]

In this study, the Z-plot shown in Figure 4.5 and PDFs from each alloy composition were all calculated using the Kirkwood parameters appropriate for the end-members with no adjustable parameters. Figure 4.7 shows PDFs obtained from the Kirkwood model plotted with measured PDFs for characteristic compositions. The model is very successful in matching both the short *and* longer-range behavior of the PDFs for all alloy compositions. The measured and calculated PDF peaks of

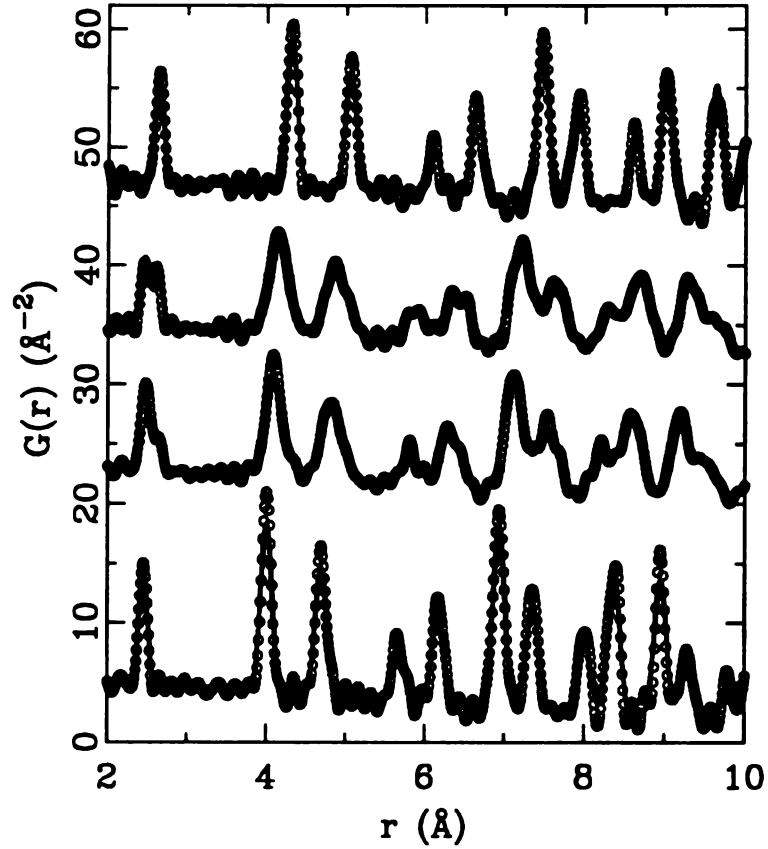


Figure 4.7: Comparison of the Kirkwood model (lines) and data (\circ) PDFs for (from top to bottom) ZnTe, ZnSe_{3/6}Te_{3/6}, ZnSe_{4/6}Te_{2/6}, and ZnSe.

the nearest neighbor bonds are shown on an expanded scale in Figure 4.8. It is clear that the model based on the Kirkwood potential does a very satisfactory job of explaining both the PDF peak positions and widths and appears to produce a very satisfactory model for the structure of these II-VI alloys.

4.3.3 Comparison with In_xGa_{1-x}As

The results found for ZnSe_{1-x}Te_x are not entirely unexpected. In a previous study of In_xGa_{1-x}As similar results were obtained. [11] With high real space resolution measurements now possible, direct observation of the nn distances in addition to the static strain in the system is observed. The basis for the comparison

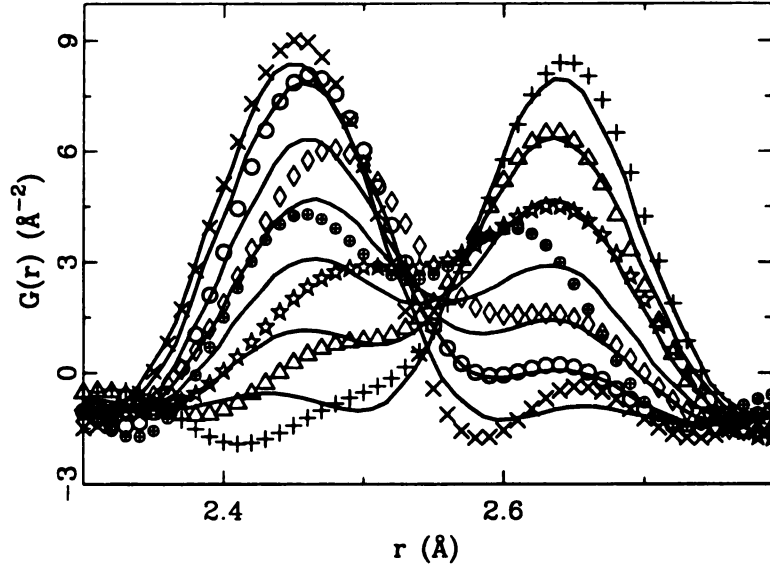


Figure 4.8: Comparison of the Kirkwood model (lines) and data (points) nn distances for $\text{ZnSe}_{1-x}\text{Te}_x$ where x is 0 (\times), $\frac{1}{6}$ (\circ), $\frac{2}{6}$ (\diamond), $\frac{3}{6}$ (\oplus), $\frac{4}{6}$ (\star), $\frac{5}{6}$ (\triangle), and 1 ($+$).

between $\text{ZnSe}_{1-x}\text{Te}_x$ and $\text{In}_x\text{Ga}_{1-x}\text{As}$ is that the two systems are both semiconductor alloys with zinc-blende structures. However, they vary in a couple of important aspects. The salient difference is number of valence electrons.

$\text{ZnSe}_{1-x}\text{Te}_x$ are more polar alloys and so might be expected to have bonding with more ionic character than $\text{In}_x\text{Ga}_{1-x}\text{As}$ which should give rise to smaller β values since ionic bonding is less directional than covalent bonding. Indeed the bond-bending magnitudes are less in $\text{ZnSe}_{1-x}\text{Te}_x$ than $\text{In}_x\text{Ga}_{1-x}\text{As}$ (Table 4.2.3). However, the nearest neighbor bonds are stiffer in $\text{In}_x\text{Ga}_{1-x}\text{As}$. This is presumably also due to the lower polarity of this material resulting in greater orbital overlap and covalency. The result is that the β/α ratio and a^{**} are similar for the two systems. Since it is this ratio, rather than the values of α and β themselves, that has the greatest impact on the structure of the alloy, we find very strong similarities in the local structures of $\text{In}_x\text{Ga}_{1-x}\text{As}$ and $\text{ZnSe}_{1-x}\text{Te}_x$. For example, the Z-plots from both systems are plotted on the same scale in Figure 4.9.

The similarity in the Z-plots is even more striking because of the similar

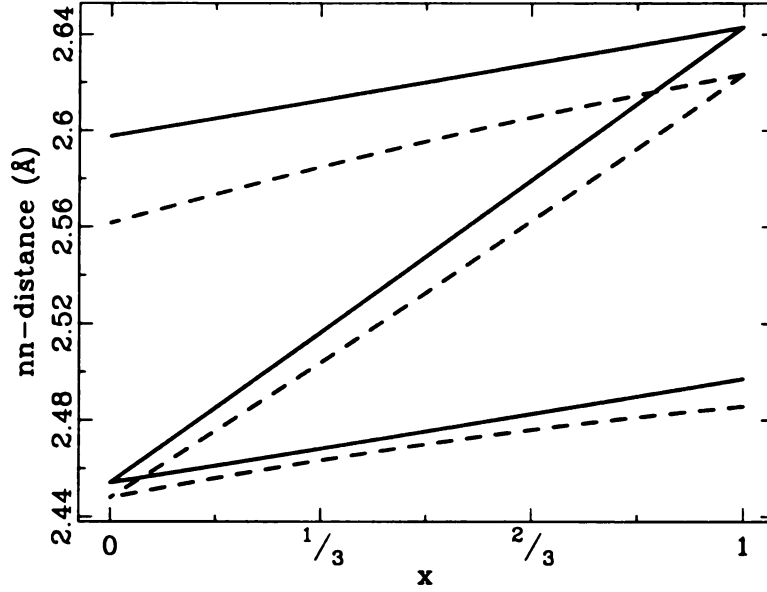


Figure 4.9: Comparison of the theoretically calculated $\text{ZnSe}_{1-x}\text{Te}_x$ (solid line) and $\text{In}_x\text{Ga}_{1-x}\text{As}$ (dashed line) z-plots.

| A - B | r_A (Å) | r_B (Å) | r_{A+B} (Å) |
|-------|-----------|-----------|---------------|
| GaAs | 1.26 | 1.18 | 2.44 |
| InAs | 1.44 | 1.18 | 2.62 |
| ZnSe | 1.31 | 1.14 | 2.45 |
| ZnTe | 1.31 | 1.32 | 2.63 |

Table 4.2: Ionic radii from literature when atoms are in tetrahedral covalent bonds. [2]

bond-lengths of the end-members in these two alloy systems. The ionic radii for the atoms in these two alloy series are reproduced in Table 4.2. Despite the ionic radii themselves being somewhat different, it is clear that the sums of the ionic radii of the end-members yield values that are within 0.01 Å of each other.

As well as the Z-plots of $\text{In}_x\text{Ga}_{1-x}\text{As}$ and $\text{ZnSe}_{1-x}\text{Te}_x$ matching rather well, the observed magnitude of the mean-square width of the high- r PDFs peak are rather similar in the two alloy series. This can be seen by comparing Figure 4.6 with Figure 4 in Ref. [11]. For example, the static strain contribution to the PDF peak widths of the unalloyed site has a maximum at 0.027Å^2 and 0.023Å^2 for $x = 0.5$ in $\text{ZnSe}_{1-x}\text{Te}_x$ and $\text{In}_x\text{Ga}_{1-x}\text{As}$, respectively.

It thus appears that the structure of the alloys is principally determined by the differences in bond-length of the end-members and by the β/α ratio rather than by the absolute values of α and β or the absolute values of the ionic radii themselves. It has been shown [56, 1] that the β/α ratios of tetrahedral semiconductors are somewhat universal resulting in a^{**} values close to 0.75 for a wide range of semiconductors. It also does not appear to matter whether the cation or anion sublattice is alloyed. The unalloyed sublattice accommodates the majority of the atomic scale strain.

4.4 Conclusion

From high real space resolution PDFs of $\text{ZnSe}_{1-x}\text{Te}_x$ we conclude the following. In agreement with earlier EXAFS results and the Kirkwood model the Zn-Se and Zn-Te bond-lengths do not take a compositionally averaged length but remain close to their natural lengths. Direct measurement of this was allowed by the new GEM instrument at ISIS. The bond-length mismatch creates considerable local disorder which manifests itself as broadening in the PDF peak widths and can be separated into thermal motion and static strain. $\text{ZnSe}_{1-x}\text{Te}_x$ was compared with $\text{In}_x\text{Ga}_{1-x}\text{As}$. Despite having different polarity the atomic strains in both systems are very similar and both are well modeled by the Kirkwood potential based model. This suggests that the atomic strains in tetrahedral semiconductor alloys are quite universal depending principally on the bond-length mismatch of the end-members and the ratio of the bond-stretch to bond-bending forces.

Chapter 5: Temperature

Dependence of $\text{ZnSe}_{1-x}\text{Te}_x$

5.1 Introduction

Information about the atomic potential can be obtained from the thermal motion of atoms in the solid measured from the pair distribution function (PDF). If a model potential is known it is possible to calculate the PDF including all the lattice dynamics. The dynamical matrix is determined from the potential and its eigenvalues and eigenvectors are found. The PDF peak broadening due to thermal motions is then obtained by projecting the phonons into real-space and taking into account the Bose factor. This procedure was done in the present case using a Kirkwood potential as described in Chapter 4. While temperature dependent data present a more exacting test of model potentials, semi-quantitative information about the potential can be obtained through empirical fitting of the Einstein and Debye models to the temperature dependence of the PDF peak widths.

For this reason we have studied the temperature dependence of the PDF peak widths in the endmember compounds (as a more stringent test of the potential model) and in the alloys. Certain questions remain regarding the nature of the potential in the alloys. For example, the approximation has been taken that the Se-Zn-Te bond bending interaction is the geometric mean of Se-Zn-Se and Te-Zn-Te which are known from bulk moduli measurements of the endmember compounds. Verifying whether the atomic level strain in the alloy significantly modifies the potential parameters is also of great interest. Here we present preliminary results using empirical methods. While using the full potential is superior, it is beyond the scope of this study and will be carried out in the future.

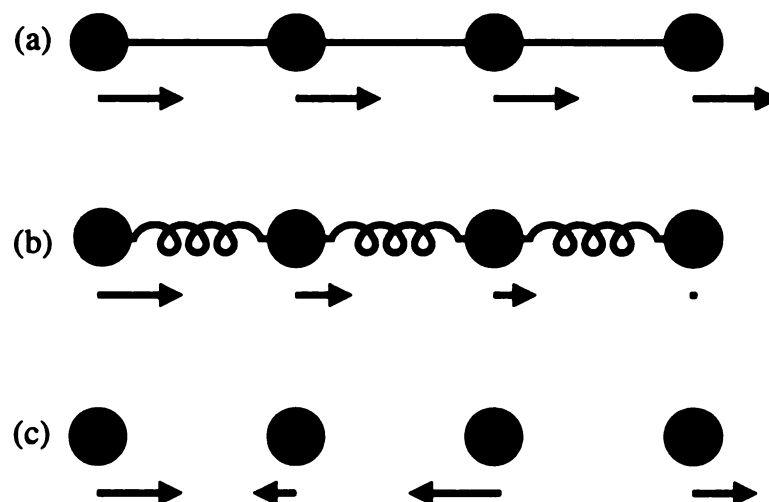


Figure 5.1: Cartoon of motion in solids. Rigid body motion (a), correlated atomic motion (b), and uncorrelated atomic motion (c) are shown.

$\text{ZnSe}_{1-x}\text{Te}_x$ alloys have two distinct nearest neighbor (nn) bond lengths due to the different interatomic potentials of Zn-Se and Zn-Te. The atoms in $\text{ZnSe}_{1-x}\text{Te}_x$ move about their ideal sites because of thermal motion. However, local displacements will also force the atoms from the average crystallographic sites resulting in static disorder, as described in the previous chapter. This static disorder masks the PDF peak broadening due to the dynamics making it difficult to study the nature of the potential directly in the alloy. However, as shown in Figure 4.6, the width of the nn peaks is not significantly increased by static disorder in the alloys.

These measurements present an opportunity to look for softening of the bond-stretch term in the potentials of the alloys. The motion of the atoms in solids is correlated. Figure 5.1 shows a cartoon of three different levels of interaction between the atoms. In the case of rigid body motion (a), all of the atoms in a material would move in unison. In the limit of uncorrelated motion (c), the atoms do not interact at all. The atoms would be at the average structure distances and observe random thermal motion. The real situation lies between these two limits (b); the motion is somewhat, but not completely correlated. The motional

correlations die out with increasing atomic separation. To understand this we can make a simple model for a highly correlated solid. If we start with the completely correlated rigid body case, we see that all the atoms move together regardless of separation. Now cut the rigid rods of Figure 5.1(a) and insert a small, stiff, but compressible, spring where we cut. We see that near neighbors still move in a highly correlated fashion with a small amount of randomness coming from the springs. Between second neighbors lie two springs, between third neighbors three springs, and so on. It is immediately apparent that the correlation of the motion will die out with further neighbors. In the PDF this is evident as an r -dependent peak broadening that is clearly evident, especially in semiconductors. [67, 68] In the previous chapter the local bond length order at 10K was shown to produce strain seen as broadening of the fn peaks with most of the strain on the Zn sites. This chapter will use temperature dependent data to verify the assumption that the contribution of the PDF peak width due to *thermal motion* varies linearly between the end member values for all of the compositions. To test this assumption ZnSe, ZnSe_{0.5}Te_{0.5}, and ZnTe were measured as a function of temperature. By extracting both the nn and fn peak widths the nature of the bonds can be further understood.

5.2 Experimental

5.2.1 Data Reduction

Three samples (ZnSe, ZnSe_{0.5}Te_{0.5}, and ZnTe) were measured using the General Materials Diffractometer (GEM) at ISIS as described in Section 4.2.2. The data were measured for thirty to sixty minutes per data-set as shown schematically in Figure 5.2. The 10K data parameters were used as a template to process the other data of the same material, then G_{low} was minimized by changing β as suggested in Chapter 3. To improve statistics, data that were separated in temperature by 10K

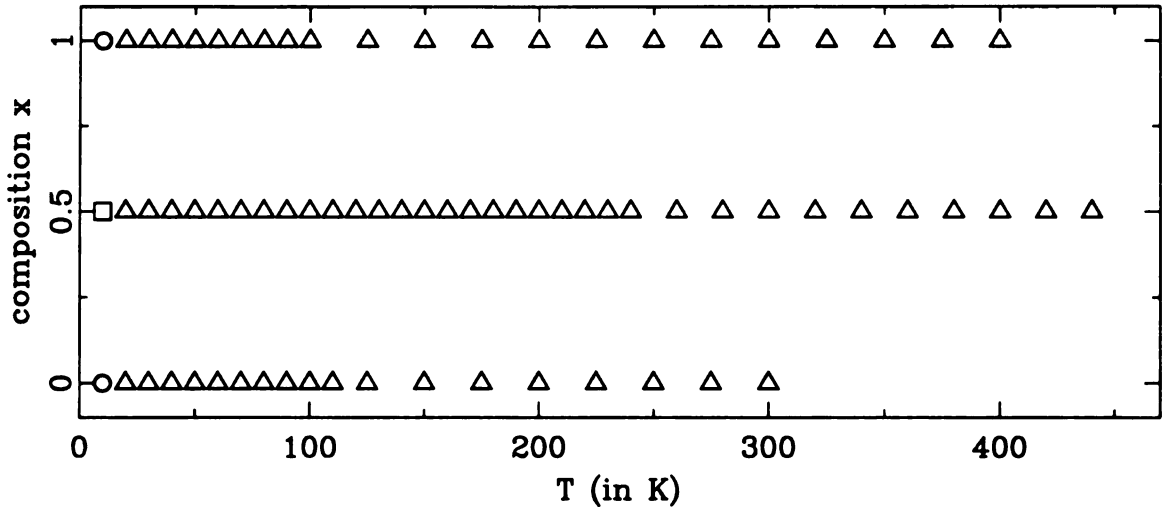


Figure 5.2: Data measured as a function of temperature and composition. The data was measured for 60 minutes (\circ), 45 minutes (\square), and 30 minutes (\triangle).

were combined; the effective temperature is the average of the two temperatures.

5.2.2 Method of Extracting Peak Widths

The nn widths were extracted using `rwid`. `rwid` is a program based on the PDFFIT [34] engine that can fit any number of Gaussians to a radial distribution function (RDF). The RDF can be written in terms of the PDF as

$$T(r) = rG(r) + 4\pi r^2 \rho_0, \quad (5.1)$$

where ρ_0 is the average number density. For zinc-blende structures $\rho_0 = 8/a^3$ where a is the lattice parameter found using PDFFIT and there are eight atoms in the conventional unit cell. While the range that the fit was being done over was different for ZnSe ($2.2\text{\AA} \leq r \leq 2.7\text{\AA}$), $\text{ZnSe}_{0.5}\text{Te}_{0.5}$ ($2.2\text{\AA} \leq r \leq 2.9\text{\AA}$), and ZnTe ($2.2\text{\AA} \leq r \leq 3.0\text{\AA}$) due to the different nn bond lengths, the method was the same. After choosing appropriate initial values for peak width, height and position, the refinement took place in three steps

1. width and height are varied.
2. position is varied.
3. width and height are varied.

In the case of $\text{ZnSe}_{0.5}\text{Te}_{0.5}$ there were two Gaussians being fit to the data while for ZnSe and ZnTe only one was used. The initial peak position is $\frac{\sqrt{3}}{4}a$ for ZnSe and ZnTe and $\frac{\sqrt{3}}{4}a \pm 0.07\text{\AA}$ for $\text{ZnSe}_{0.5}\text{Te}_{0.5}$. The $\pm 0.07\text{\AA}$ for $\text{ZnSe}_{0.5}\text{Te}_{0.5}$ is to account for the nominal peak separation of 0.14\AA in the alloy as determined in Chapter 4.

To extract the fn peak widths the data was modeled using PDFFIT. The modeling was done in three steps:

1. The scale factor (N_m), and the lattice parameter ($\text{latt}[i]$) are varied.
2. The isotropic thermal parameters, U_{Zn} and U_{alloy} , are varied.
3. N_m , $\text{latt}[i]$, U_{Zn} , and U_{alloy} are varied.

The refinement range was $2.3\text{\AA} \leq r \leq 20\text{\AA}$ for ZnSe and ZnTe and $3.1\text{\AA} \leq r \leq 20\text{\AA}$ for $\text{ZnSe}_{0.5}\text{Te}_{0.5}$ with a fixed Q -resolution ($\text{qsig}[i]$) of 0.03536 representative of GEM. The correlation factor ($\text{delt}[i]$) was fixed at 0.15, 0.16, and 0.17 for ZnSe , $\text{ZnSe}_{0.5}\text{Te}_{0.5}$, and ZnTe respectively. Once the isotropic thermal parameters were extracted they were converted to PDF peak widths by

$$\sigma_{ij}^2 = U_i + U_j \quad (5.2)$$

where i and j signify the atomic components of the PDF peak.

5.3 Nearest Neighbor Information

The nn are highly correlated as seen by the sharpening of the nn peak width. [67] However, in the case of low temperature the nn peak does not broaden

| | ZnSe | ZnSe _{0.5} Te _{0.5} | ZnTe |
|-------|----------|---------------------------------------|----------|
| Zn-Se | 420(30)K | 530(30)K | - |
| Zn-Te | - | 350(30)K | 450(30)K |

Table 5.1: Debye temperature found from the nn peak widths with $\sigma_{off}^2=0.0\text{\AA}^2$.

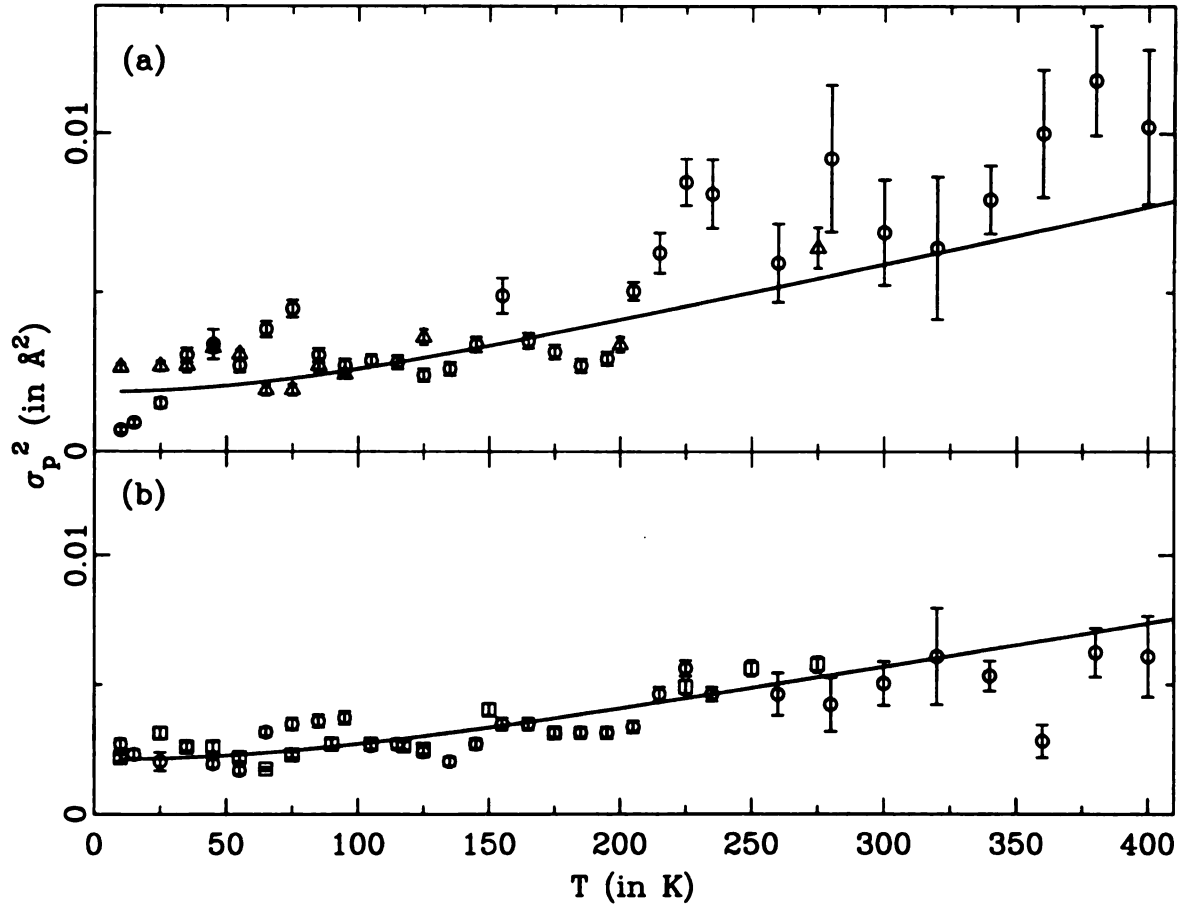


Figure 5.3: nn peak widths for Zn-Se (a) and Zn-Te (b). The widths are extracted from ZnSe (\square), ZnSe_{0.5}Te_{0.5} (\circ), and ZnTe (\triangle). The solid lines are the Debye model fit to the data.

due to static strain. This observation led to the result that the width of the nn peak arises from thermal motion not static strain.

We fit the nn widths as a function of temperature using the Debye model, [69]

$$\sigma_D^2 = \frac{3\hbar^2}{m_a k_b \Theta_D} \left[\frac{1}{4} + \left(\frac{T}{\Theta_D} \right)^2 \Phi_1 \right] + \sigma_{off}^2, \quad (5.3)$$

where m_a is the average mass, Θ_D is the Debye temperature, σ_{off}^2 is the static contribution to the peak width, and Φ_1 is given by

$$\Phi_n = \int_0^{\Theta_D/T} \frac{x^n}{e^x - 1} dx. \quad (5.4)$$

Due to the correlated nature of the nn motions the Debye temperature determined in this way will not correspond to that determined crystallographically or from thermal measurements such as specific heat. Nonetheless, we can compare Debye temperatures obtained from similar samples. Because of the complex nature of Φ_1 , fitting the Debye model to data directly is difficult at best. An alternative method is to fit the Einstein model then use the relation

$$\Theta_D = \frac{5}{3} \Theta_E \quad (5.5)$$

with the same value of σ_{off}^2 . [70] This method of determining Θ_D emphasizes the need for good statistics to distinguish between the Debye and Einstein models.

Unfortunately, the statistical nature of the nn distribution does not allow this here.

The extracted nn peak widths can be seen in Figure 5.3 with fit parameters in Table 5.1. It is immediately apparent that significant fluctuations are evident in the data which do not exhibit smooth, monotonic, Debye behavior. This behavior is unlikely to be real. Furthermore, these fluctuations do not appear to be completely random in nature and are not reflected in the estimated error bars. The higher

temperature measurements have larger uncertainties due to the statistics related to the shorter measurement times. The fluctuations may come from some kind of systematic instability in the experimental setup. One such effect is moderator temperature which, it is now known, fluctuated on the order of hours at the time of the measurements. Steps have since been taken to rectify this problem. With the understanding that this limits the uncertainty of the measurements data have been fit using the Debye model. The reader will notice that the nn peak width does not have any additional offset due to static strain in agreement with the low temperature results in Chapter 4, i.e., the measured asymptotic low-temperature peak width is well explained by quantum zero point motion. The lack of strain is re-iterated in the fact that plotting the Zn-Se peak width for ZnSe and ZnSe_{0.5}Te_{0.5} together yields a single curve, as do the Zn-Te peak widths. This behavior shows that the peak width is independent of material composition and instead depends on the interatomic potential. This is the reason for the Zn-Se widths being on one curve and Zn-Te widths on another.

5.4 Far Neighbor Information

For convenience we fit far neighbor peaks using the Einstein model, [71]

$$\sigma_E^2 = \frac{\hbar^2}{2m_r k_b \Theta_E} \coth\left(\frac{\Theta_E}{2T}\right) + \sigma_{off}^2 \quad (5.6)$$

where m_r is the reduced mass, Θ_E is the Einstein temperature, and σ_{off}^2 is the static contribution to the peak width. As we have discussed, both Einstein and Debye models give qualitatively similar temperature dependence and our data are not good enough to distinguish them. The fit parameters are shown in Table 5.2 and the extracted widths are shown in Figure 5.4.

As before, significant non-random fluctuations are evident in the alloy data

| | Θ_E in K | | | σ_{off}^2 in \AA^2 | | |
|-------|-----------------|---------------------------------------|--------|------------------------------------|---------------------------------------|-----------|
| | ZnSe | ZnSe _{0.5} Te _{0.5} | ZnTe | ZnSe | ZnSe _{0.5} Te _{0.5} | ZnTe |
| Zn-Zn | 145(2) | 141(2) | 151(2) | 0.0013(4) | 0.0232(4) | 0.0006(4) |
| Zn-Se | 146(1) | 144(1) | - | 0.0009(4) | 0.0160(4) | - |
| Zn-Te | - | 132(2) | 125(2) | - | 0.0164(4) | 0.0010(4) |
| Se-Se | 148(1) | 148(1) | - | 0.0005(4) | 0.0088(4) | - |
| Te-Te | - | 119(5) | 99(5) | - | 0.0095(4) | 0.0015(4) |
| Se-Te | - | 134(5) | - | - | 0.0092(4) | - |

Table 5.2: Parameters for Einstein model fit to the fn peak widths.

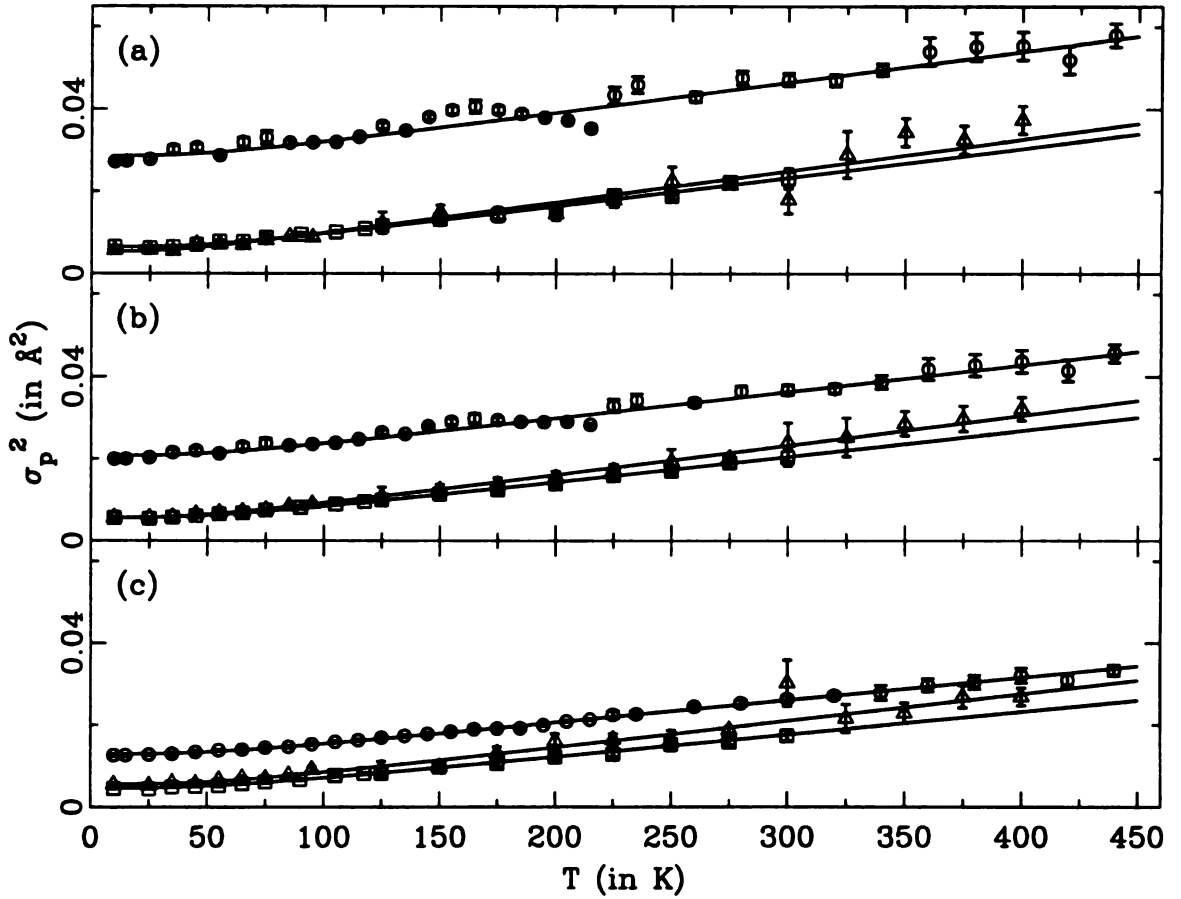


Figure 5.4: fn peak widths for Zn-Zn (a), Zn-Alloy (b), and Alloy-Alloy (c) plotted with fits of the Einstein model. The widths are extracted from ZnSe (\square), ZnSe_{0.5}Te_{0.5} (\circ), and ZnTe (\triangle).

that compromises the fit somewhat. However, the qualitative effects are very clear. First it is apparent from Figure 5.4 that all the curves are nearly parallel but have different offsets. This is also reflected in the fact that the refined Einstein temperatures are very similar to each other. The values for the Einstein temperatures are somewhat lower than those obtained from the nn peak. If we convert the nn Zn-Se and Zn-Te peak Debye temperatures to Einstein temperatures using Equation 5.5 we get 250K and 270K respectively compared to 146K and 125K measured from the fn peaks. This simply reflects the fact that the nn motion is correlated and that this has not been properly accounted for in the Debye model fit to the nn peaks. This is being investigated in more detail elsewhere [72]. For the Zn-Se/Te pairs the Einstein temperature is lower in the Te compound. As is evident in Table 5.1, α for this material is about 8% smaller than in the Se compound so this smaller Einstein temperature might be real. It is less easy to explain why this trend is reversed in the case of Zn-Zn pairs (ZnTe compound has a higher Θ_E in this case), although we note the β parameters for each compound are comparable (Table 5.1) and Zn-Zn pairs are second neighbor pairs. Although this may be a real effect, it is somewhat dangerous to overinterpret these numbers given the quantitative nature of the fits.

We now consider the Einstein temperatures in the alloy compound in contrast to the end-members. First note that, as expected from Figure 5.4, the values are very similar to those of the endmember compounds, supporting the use of potential parameters from the endmembers with the alloys. We also note that the value for Se-Te, which has no analog in the endmember compounds, is the mean of the values for Se-Se and Te-Te in the alloys. Again, caution should be exercised against overinterpretation. Nonetheless, the main approximations that we have made in our potential based modeling appear to be confirmed here.

Finally, we consider the offsets yielded by the Einstein modeling. The offsets

should be a direct measure of the static (non zero-point) disorder present in the compounds. They can, therefore, be compared with the values presented in Chapter 4 which were extracted assuming that the thermal disorder in the alloys was the same as in the end-members. The offsets refined for the endmember compounds are, indeed, very small and are unlikely to be significant. Since we expect no static disorder and no offset in these compounds this is an independent measure of the quality of our procedures for extracting PDF peak widths on an absolute scale and fitting them. It is reasonable to use the offsets for the endmembers as a measure of the uncertainty in this parameter of around 0.001\AA^2 . The absolute values of the peak widths can therefore be expected to be accurate at around the 2% level or better.

Turning to the alloys it is clear that significant disorder exists and that it is least on the alloy (SeTe) sublattice and greatest on the Zn sublattice. The mean of the two values is seen for Zn-alloy pairs as expected. Referring to Figure 4.6, it is clear that this is also in rather good agreement with the values determined for the static strain using the approximations of Chapter 4.

5.5 Conclusions

From the temperature dependent PDF measurements we conclude the following. The evolution with temperature of the PDF peak widths is material independent as seen by all curves for a given type of peak being either parallel or overlapping and from the fitting values. Thus, the approximation that potentials from the endmembers can be reasonably transferred to the alloys is reasonable. Our procedures for extracting peak widths from the PDF of neutron data gave, in this case, peak widths that are accurate on an absolute scale at the level of a few percent. The Einstein and Debye models work reasonably well to explain the data,

though clearly a more complete analysis using a measured phonon density of states would be preferable. However, in the spirit that the PDF is a relatively quick and easy experiment that can yield useful (though low precision) information about the atomic potential, these empirical models appear to be a valuable approach for studying trends. The results for static strains obtained on low-temperature data are quantitatively reproduced by this temperature dependent experiment. In the future, temperature dependent PDFs will be calculated from the Kirkwood potential to compare to the data as well.

Chapter 6: Summary and Discussion

6.1 Summary

The purpose of this work is to understand the atomic structure of bulk $\text{ZnSe}_{1-x}\text{Te}_x$ alloys. In particular we wanted to determine the relation between the local, intermediate, and average structure. Learning about the interplay between these different length scales is motivated by the need to understand (and engineer) alloy properties even in the presence of atomic scale disorder present in alloys. A prerequisite for most theoretical studies of electronic structure is an accurate atomic structure of the material in question. Despite their importance, a full description of the accurate local structure of semiconductors was lacking before this study and a related one. [15] This study was done using the pair distribution function (PDF) which allows for accurate local and intermediate structure determination.

The average zinc-blende atomic structure interpolates linearly between the end-member (ZnSe and ZnTe) values of the lattice parameter, a . In order to minimize peak broadening, measurements of the structure were done at 10K for a variety of compositions. In Chapter 4 these measurements were used to confirm the nearest neighbor (nn) peak splitting seen by earlier XAFS measurements [3] and provide further insight into the nature of the bonds. The nn bonds were close to the Pauling limit (staying near their end-member values) in contrast to the average structure which behaves very closely to the Vegard limit (linear interpolation between end-member values). The effect of the nn bond on the far neighbor (fn) distribution was then explored by looking at the nn and fn PDF peak widths. We determined that, while the nn peak widths do not vary from the end member

values, the fn peak widths are affected by the local bond length order. The broadening of the fn peaks is interpreted as static strain and is bond-specific, with the Zn-Zn accounting for the majority of broadening due to strain. Looking at the five different local neighborhoods of the Zn site in contrast to the one neighborhood of the alloy site explains this phenomenon.

The measured PDFs were then compared to the Kirkwood potential model without adjustable parameters. Since the Kirkwood model agreed with the measured PDFs so well, other predictions of the Kirkwood were explored. Among the predictions is the structure of other semiconductor alloys, specifically $\text{In}_x\text{Ga}_{1-x}\text{As}$. We saw that the difference in chemical composition had little bearing on the atomic structure of the material. Qualitatively all of the results of $\text{ZnSe}_{1-x}\text{Te}_x$ and $\text{In}_x\text{Ga}_{1-x}\text{As}$ are the same.

Since semiconductors are normally used at or above room temperature rather than at 10K, it is of great interest to see how the low and room temperature structures compare to each other. In Chapter 5 ZnSe, $\text{ZnSe}_{0.5}\text{Te}_{0.5}$, and ZnTe were measured over a large range of temperatures. It was confirmed that the peak widths can indeed be split into static and thermal contributions. Also observed was the fact that the temperature dependence of the peak widths depends only on the type of bond, not the material.

In the course of this work we used, for the first time, the new GEM neutron powder diffractometer at ISIS neutron facility at the Rutherford Laboratory in Oxfordshire, England. This is the first of a new generation of neutron diffractometers with very high solid angle coverage on bright sources giving unprecedented gains in measurement throughput. To put this in perspective, we found that the data rate from GEM is of the order of 100x faster than the SEPD diffractometer at the Intense Pulsed Neutron Source at Argonne National Laboratory that has been the instrument of choice for many previous studies in the

Billinge group. Thus, four days of GEM beam-time would correspond to more than 1 year of continuous SEPD beamtime. This revolution in data acquisition presented special challenges for the computer based data reduction and analysis. In order to successfully carry out this project the data acquisition software, and data analysis protocols, had to be completely overhauled. The necessity to somewhat automate data reduction, when faced with ≥ 100 data-sets from a single measurement, became apparent and methods for assuring that PDFs of optimal quality were obtained in this process had to be developed. This is described in Chapter 3 of this thesis. Though not described in detail in the thesis, a straightforward GUI interface was also developed for the computer analysis programs, as well as a number of other program improvements. The interested reader is referred to the program documentation for the program PDFgetN and the accompanying publication. [30]

6.2 Future Work

This work has produced a greater understanding of $\text{ZnSe}_{1-x}\text{Te}_x$, but more questions need to be answered. While the temperature dependence of the peak widths was appropriately described using the Debye and Einstein models, they are only rough approximations. Since the Kirkwood model was successfully used to describe the atomic structure of $\text{ZnSe}_{1-x}\text{Te}_x$ at 10K, it should be tested against the temperature dependence of the peak widths. The potential model will give further insight into the nature of the bonds.

Use of the Kirkwood model suggests other work that could be done. Similar measurements of other pseudobinary semiconductors will further the understanding of the atomic structure. By measuring more II-VI semiconductors the structure can be studied by varying the lattice parameters as the general chemistry is unchanged. Then by measuring alloys with the same lattice parameter, semiconductors of

different families (IV-IV, III-V, and I-VII) should be measured to study the effect of the chemistry on the structure. Comparison with $\text{In}_x\text{Ga}_{1-x}\text{As}$ in Chapter 4 hints that chemistry is not as important in the atomic structure first believed. This would mean that the electronic and atomic structure are actually quite independent of each other.

This work has shown in general that local structure can be quite different from the average structure determined crystallographically. This is also true in a wide range of materials beyond semiconductor alloys where multiple elements or anharmonicities exist. In fact, this describes a majority of materials of interest to physicists, chemists and materials scientists these days. With the advent of powerful spectrometers like GEM and easier, faster, and more accurate PDF data analysis and modeling codes similar to those developed as part of this work, we expect the use of the PDF technique to increase as an adjunct to crystallography for verifying and solving local structures.

APPENDIX

A large component of this dissertation was developing various software for a large number of tasks. Here is an incomplete list of what was written with brief descriptions. Everything listed was written using the Perl language (<http://www.perl.com>).

All programs are fully documented and available to academic researchers upon request. Many are also documented on the web under "downloads" on the Billinge-group web-page, <http://www.pa.msu.edu/cmp/billinge-group/>.

- **PDFgetN** [30] - A program to extract the pair distribution function from spallation source neutron scattering measurements.
- **PDFsaveN**, **PDFsearchN**, and **PDFrestoreN** - A suite for archiving neutron data.
- **pow** - Calculate the x-ray diffraction Bragg positions of a crystal.
- **Activate** - CGI script that calculates the time until a sample is no longer radioactive after exposed to a neutron source.
<http://skywalker.pa.msu.edu/cgi-bin/activate.cgi>
- **mu-t** - CGI script that calculates the x-ray absorption of samples.
<http://skywalker.pa.msu.edu/cgi-bin/mut.cgi>
- **Beam Time Scheduler** - CGI script used for planning and tracking experimental measurements.
- **einsteinfit** and **einstein** - Fit and calculate the PDF peak width (σ_p^2) as a function of temperature using the Einstein model for a given Θ_E and σ_{off}^2 .
- **debye** - Calculate the PDF peak width (σ_p^2) as a function of temperature using the Debye model for a given Θ_D and σ_{off}^2 .

Bibliography

- [1] Y. Cai and M. F. Thorpe, *Length mismatch in random semiconductor alloys. II. Structural characterization of psuedobinaries*, Phys. Rev. B **46**, 15879 (1992).
- [2] C. Kittel, *Introduction to Solid State Physics*, Wiley, New York, 7th edition, 1996.
- [3] J. B. Boyce and J. C. Mikkelsen, Jr., *Local Structure of Pseudobinary Semiconductor Alloys*, J. Cryst. Growth **98**, 37 (1989).
- [4] A. M. Glass, Science **235**, 1003 (1985).
- [5] Z. Q. Li and W. Potz, *Electronic density of states of semiconductor alloys from lattice-mismatched isovalent binary constituents*, Phys. Rev. B **46**, 2109 (1992).
- [6] A. Silverman, A. Zunger, R. Kalish, and J. Adler, *Atomic-scale structure of disordered $Ga_{1-x}In_xP$ alloys*, Phys. Rev. B **51**, 10795 (1995).
- [7] A. Balzarotti et al., *Model of the local structure of random ternary alloys: Experiment versus theory*, Phys. Rev. B **31**, 7526 (1985).
- [8] T. Hahn, editor, *International Tables for Crystallography*, volume A, pages 648–650, Kluwer Academic Publishers, Boston, 4th edition, 1996.
- [9] L. Vegard, Z. Phys. **5**, 17 (1921).
- [10] J. C. Mikkelsen and J. B. Boyce, *atomic scale structure of random solid solutions: extended x-ray-absorption fine-structure study of $Ga_{1-x}In_xAs$* , Phys. Rev. Lett. **49**, 1412 (1982).
- [11] V. Petkov et al., *High real-space resolution measurement of the local structure of $Ga_{1-x}In_xAs$ using x-ray diffraction*, Phys. Rev. Lett. **83**, 4089 (1999).
- [12] R. A. Young, editor, *The Rietveld Method*, Oxford University Press, 1995.

- [13] J. B. Boyce and J. C. Mikkelsen, Jr., *Local Structure of Ionic Solid Solutions: Extended X-Ray Absorption Fine-Structure Study*, Phys. Rev. B **31**, 6903 (1985).
- [14] V. Petkov et al., *Local structure of $\text{In}_{0.5}\text{Ga}_{0.5}\text{As}$ from joint high-resolution and differential pair distribution function analysis*, J. Appl. Phys. **88**, 665 (2000).
- [15] I. Jeong et al., *Local structure study of $\text{In}_x\text{Ga}_{1-x}\text{As}$ semiconductor alloys using high energy synchrotron x-ray diffraction*, Phys. Rev. B **63**, 205202 (2001).
- [16] R. F. Pierret, *Semiconductor Fundamentals*, volume I of *Modular Series on Solid State Devices*, Addison-Wesley Publishing Company, Reading, MA, 1983.
- [17] R. F. Pierret, *Advanced Semiconductor Fundamentals*, volume VI of *Modular Series on Solid State Devices*, Addison-Wesley Publishing Company, Reading, MA, 1989.
- [18] K. J. Close and J. Yarwood, *An Introduction to Semiconductors*, Heinemann Educational Books, London and Edinburgh, 1971.
- [19] D. A. Fraser, *The Physics of semiconductor devices*, Clarendon Press, Oxford, 1977.
- [20] A. Chen and A. Sher, *Semiconductor Alloys Physics and Materials Engineering*, Plenum Press, New York, 1995.
- [21] H. Ohtani, K. Kojima, K. Ishida, and T. Nishizawa, J. Alloy Compd. **182**, 103 (1992).
- [22] N. W. Ashcroft and N. D. Mermin, *Solid State Physics*, Saunders College Publishing, 1976.

- [23] V. Petkov and S. J. L. Billinge, *Local structure of random $\text{In}_x\text{Ga}_{1-x}\text{As}$ alloys by full-profile fitting of atomic pair distribution functions*, Physica B **305**, 83 (2001).
- [24] C. N. J. Wagner, *Direct methods for the determination of atomic-scale structure of amorphous solids (x-ray, electron and neutron scattering)*, J. Non-Cryst Solids **31**, 1 (1978).
- [25] B. E. Warren, *X-ray Diffraction*, Dover, New York, 1990.
- [26] J. I. Langford and D. Louër, *Powder Diffraction*, Rep. Prog. Phys. **59**, 131 (1996).
- [27] Y. Waseda, *The structure of non-crystalline materials*, McGraw-Hill, New York, 1980.
- [28] P. Debye, *Basic X-ray Scattering Equations*, Ann. Phys. **46**, 809 (1915).
- [29] K. Laaziri et al., *Quantitative treatment for extracting coherent elastic scattering from X-ray scattering experiments*, J. Appl. Crystallogr. **32**, 322 (1999).
- [30] P. F. Peterson, M. Gutmann, Th. Proffen, and S. J. L. Billinge, *PDFgetN: A user-friendly program to extract the total scattering structure function and the pair distribution function from neutron powder diffraction data*, J. Appl. Crystallogr. **33**, 1192 (2000).
- [31] I. Jeong, J. Thompson, A. M. P. Turner, and S. J. L. Billinge, *PDFgetX: a program for determining the atomic pair distribution function from x-ray powder diffraction data*, J. Appl. Crystallogr. **34**, 536 (2001).
- [32] S. J. L. Billinge et al., *Direct Observation of Lattice Polaron Formation in the Local Structure of $\text{La}_{1-x}\text{Ca}_x\text{MnO}_3$* , Phys. Rev. Lett. **77**, 715 (1996).

- [33] S. J. L. Billinge, E. S. Božin, M. Gutmann, and H. Takagi, *Microscopic charge inhomogeneities in underdoped $\text{La}_{2-x}\text{Sr}_x\text{CuO}_4$: local structural evidence*, J. Supercond. **13**, 713 (2000).
- [34] T. Proffen and S. J. L. Billinge, *PDFFIT, a program for full profile structural refinement of the atomic pair distribution function*, J. Appl. Crystallogr. **32**, 572 (1999).
- [35] T. Egami, Pdf analysis applied to crystalline materials, in *Local Structure from Diffraction*, edited by S. J. L. Billinge and M. F. Thorpe, page 1, New York, 1998, Plenum.
- [36] T. Egami, *Atomic Correlations in Non-periodic Matter*, Mater. Trans. **31**, 163 (1990).
- [37] H. P. Klug and L. E. Alexander, *X-ray Diffraction Procedures for Polycrystalline Materials*, Wiley, New York, 2nd edition, 1974.
- [38] A. K. Soper, W. S. Howells, and A. C. Hannon, Rutherford Appleton Laboratory Report , RAL (1989).
- [39] A. C. Hannon, W. S. Howells, and A. K. Soper, Atlas - a suite of programs for the analysis of time-of-flight neutron-diffraction data from liquid and amorphous samples, in *Institute of Physics Conference Series*, volume 107, pages 193–211, IOP Publishing LTD, 1990.
- [40] S. J. L. Billinge and T. Egami, *Short-range atomic structure of $\text{Nd}_{2-x}\text{Ce}_x\text{CuO}_{4-y}$ determined by real-space refinement of neutron-powder-diffraction data*, Phys. Rev. B **47**, 14386 (1993).
- [41] A. C. Wright et al., in *Neutron Scattering for Materials Science II*, edited by D. A. Neumann, T. P. Russell, and B. J. Wuensch, volume 376, page 635, 1995.

- [42] P. Zetterstrom and R. L. McGreevy, *Improved Monte Carlo program MCGR, for determining $G(r)$* , Physica B **276**, 187 (2000).
- [43] T. C. Terwilliger, *MAD phasing - Bayesian estimates of F-A*, Acta Crystallogr. D **50**, 11 (1994).
- [44] R. Lovell, G. R. Mitchell, and A. H. Windle, *An Improved Transformation Procedure for Radial Distribution Function Analysis*, Acta Cryst. **A35**, 598 (1979).
- [45] A. C. Larson and R. B. VonDreele, *General Structure Analysis System (GSAS)*, Los Alamos National Laboratory, Report , 86 (1994).
- [46] B. H. Toby, *EXPGUI, a graphical user interface for GSAS*, J. Appl. Crystallogr. **34**, 210 (2001).
- [47] G. Kartha, *A New Method of Calculating the Sclae Factor in Structure Analysis*, Acta Cryst. **6**, 817 (1953).
- [48] N. Norman, *The Fourier Transform Method for Normalizing Intensities*, Acta Cryst. **10**, 370 (1957).
- [49] J. Krogh-Moe, *A Method for Converting Experimental X-ray Intensities to an Absolute Scale*, Acta Cryst. **9**, 951 (1956).
- [50] V. Petkov and R. Danev, *IFO - a program for image reconstruction-type calculation of atomic distribution functions for disordered materials*, J. Appl. Crystallogr. **31**, 609 (1998).
- [51] W. I. F. David and D. S. Sivia, *Background estimation using a robust Bayesian analysis*, J. Appl. Crystallogr. **34**, 318 (2001).
- [52] Z. Kaszukur, *Convolutional Approach to the Normalization of Intensity Scattered by Polycrystalline Substances*, J. Appl. Crystallogr. **23**, 180 (1990).

- [53] F. L. Cumbreira, F. Sanchez-Bajo, and A. Munoz, *An Improved Method for the Normalization of the Scattered Intensity and Accurate Determination of the Macroscopic Density of Noncrystalline Materials*, J. Appl. Crystallogr. **28**, 408 (1995).
- [54] A. J. Leadbetter and A. C. Wright, *Diffraction Studies of Glass Structure II. The Structure of Vitreous Germania*, J. Non-Cryst Solids **7**, 37 (1972).
- [55] D. Louca and T. Egami, *Local lattice distortions in $\text{La}_{1-x}\text{Sr}_x\text{MnO}_3$ studied by pulsed neutron scattering*, Phys. Rev. B **59**, 6193 (1999).
- [56] Y. Cai and M. F. Thorpe, *Length mismatch in random semiconductor alloys I. General theory for quaternaries*, Phys. Rev. B **46**, 15872 (1992).
- [57] N. Mousseau and M. F. Thorpe, *Length mismatch in random semiconductor alloys. III. Crystalline and amorphous SiGe*, Phys. Rev. B **46**, 15887 (1992).
- [58] M. C. Schabel and J. L. Martins, *Structural model for pseudobinary semiconductor alloys*, Phys. Rev. B **43**, 11873 (1991).
- [59] S. Larach, R. E. Shrader, and C. F. Stocker, *Anomalous Variation of Band Gap with Composition in Zinc Sulfo- and Seleno-Tellurides*, Phys. Rev. **108**, 587 (1957).
- [60] S. J. L. Billinge, *Real-space rietveld: Full profile structure refinement of the atomic pair distribution function*, in *Local Structure from Diffraction*, edited by S. J. L. Billinge and M. F. Thorpe, page 137, New York, 1998, Plenum.
- [61] J. G. Kirkwood, J. Phys. Chem. **7**, 506 (1939).
- [62] J. S. Chung and M. F. Thorpe, *Local atomic structure of semiconductor alloys using pair distribution functions*, Phys. Rev. B **55**, 1545 (1997).

- [63] J. S. Chung and M. F. Thorpe, *Local atomic structure of semiconductor alloys using pair distribution functions II*, Phys. Rev. B **59**, 4807 (1999).
- [64] L. Nordheim, Ann. Phys. (Leipz.) **9**, 607 (1931).
- [65] L. Nordheim, Ann. Phys. (Leipz.) **9**, 641 (1931).
- [66] L. Pauling, *The Nature of the Chemical Bond*, Cornell Univ. Press, Ithaca, 1967.
- [67] I. Jeong, T. Proffen, F. Mohiuddin-Jacobs, and S. J. L. Billinge, *Measuring Correlated Atomic Motion Using X-ray Diffraction*, J. Phys. Chem. A **103**, 921 (1999).
- [68] M. F. Thorpe, J. S. Chung, S. J. L. Billinge, and F. Mohiuddin-Jacobs, Advances in pair distribution profile fitting in alloys, in *Local Structure from Diffraction*, edited by S. J. L. Billinge and M. F. Thorpe, page 157, New York, 1998, Plenum.
- [69] G. Beni and P. M. Platzman, *Temperature and polarization dependence of extended x-ray absorption fine-structure spectra*, Phys. Rev. B **14**, 1514 (1976).
- [70] E. Sevillano, H. Meuth, and J. J. Rehr, *Extended x-ray absorption fine structure Debye-Waller factors. I. Monatomic crystals*, Phys. Rev. B **20**, 4908 (1979).
- [71] D. Haskel, E. A. Stern, F. Dogan, and A. R. Moodenbaugh, *XAFS study of the low-temperature tetragonal phase of $\text{La}_{2-x}\text{Ba}_x\text{CuO}_4$: Disorder, stripes, and T_c suppression at $x = 0.125$* , Phys. Rev. B **61**, 7055 (2000).
- [72] I. Jeong and S. J. L. Billinge, unpublished, 2001.